Water in star-forming regions: Physics and chemistry from clouds to disks as probed by Herschel spectroscopy

A&A 648, A24 (2021)
https://doi.org/10.1051/0004-6361/202039084

Astronomy & Astrophysics

Water in star-forming regions: physics and chemistry from clouds to disks as probed by *Herschel* spectroscopy

E. F. van Dishoeck[1,2], L. E. Kristensen[3], J. C. Mottram[4], A. O. Benz[5], E. A. Bergin[6], P. Caselli[2], F. Herpin[7], M. R. Hogerheijde[1,21], D. Johnstone[8,9], R. Liseau[10], B. Nisini[11], M. Tafalla[12], F. F. S. van der Tak[13,14], F. Wyrowski[15], A. Baudry[7], M. Benedettini[16], P. Bjerkeli[10], G. A. Blake[17], J. Braine[7], S. Bruderer[2,5], S. Cabrit[18], J. Cernicharo[19], Y. Choi[13,20], A. Coutens[7], Th. de Graauw[1,13], C. Dominik[21], D. Fedele[22], M. Fich[23], A. Fuente[12], K. Furuya[24], J. R. Goicoechea[19], D. Harsono[1], F. P. Helmich[13,14], G. J. Herczeg[25], T. Jacq[7], A. Karska[26], M. Kaufman[27], E. Keto[28], T. Lamberts[29], B. Larsson[30], S. Leurini[15,31], D. C. Lis[32], G. Melnick[28], D. Neufeld[33], L. Pagani[18], M. Persson[10], R. Shipman[13], V. Taquet[22], T. A. van Kempen[34], C. Walsh[35], S. F. Wampfler[36], U. Yıldız[32], and the WISH team

(Affiliations can be found after the references)

Received 1 August 2020 / Accepted 14 December 2020

ABSTRACT

Context. Water is a key molecule in the physics and chemistry of star and planet formation, but it is difficult to observe from Earth. The *Herschel* Space Observatory provided unprecedented sensitivity as well as spatial and spectral resolution to study water. The Water In Star-forming regions with *Herschel* (WISH) key program was designed to observe water in a wide range of environments and provide a legacy data set to address its physics and chemistry.

Aims. The aim of WISH is to determine which physical components are traced by the gas-phase water lines observed with *Herschel* and to quantify the excitation conditions and water abundances in each of these components. This then provides insight into how and where the bulk of the water is formed in space and how it is transported from clouds to disks, and ultimately comets and planets.

Methods. Data and results from WISH are summarized together with those from related open time programs. WISH targeted ~80 sources along the two axes of luminosity and evolutionary stage: from low- to high-mass protostars (luminosities from <1 to $>10^5$ $L_\odot$) and from pre-stellar cores to protoplanetary disks. Lines of H_2O and its isotopologs, HDO, OH, CO, and [O I], were observed with the HIFI and PACS instruments, complemented by other chemically-related molecules that are probes of ultraviolet, X-ray, or grain chemistry. The analysis consists of coupling the physical structure of the sources with simple chemical networks and using non-LTE radiative transfer calculations to directly compare models and observations.

Results. Most of the far-infrared water emission observed with *Herschel* in star-forming regions originates from warm outflowing and shocked gas at a high density and temperature ($>10^5$ cm^{-3}, 300–1000 K, $v \sim 25$ km s^{-1}), heated by kinetic energy dissipation. This gas is not probed by single-dish low-J CO lines, but only by CO lines with $J_{\rm up} > 14$. The emission is compact, with at least two different types of velocity components seen. Water is a significant, but not dominant, coolant of warm gas in the earliest protostellar stages. The warm gas water abundance is universally low: orders of magnitude below the H_2O/H_2 abundance of 4×10^{-4} expected if all volatile oxygen is locked in water. In cold pre-stellar cores and outer protostellar envelopes, the water abundance structure is uniquely probed on scales much smaller than the beam through velocity-resolved line profiles. The inferred gaseous water abundance decreases with depth into the cloud with an enhanced layer at the edge due to photodesorption of water ice. All of these conclusions hold irrespective of protostellar luminosity. For low-mass protostars, a constant gaseous HDO/H_2O ratio of ~0.025 with position into the cold envelope is found. This value is representative of the outermost photodesorbed ice layers and cold gas-phase chemistry, and much higher than that of bulk ice. In contrast, the gas-phase NH_3 abundance stays constant as a function of position in low-mass pre- and protostellar cores. Water abundances in the inner hot cores are high, but with variations from 5×10^{-6} to a few $\times 10^{-4}$ for low- and high-mass sources. Water vapor emission from both young and mature disks is weak.

Conclusions. The main chemical pathways of water at each of the star-formation stages have been identified and quantified. Low warm water abundances can be explained with shock models that include UV radiation to dissociate water and modify the shock structure. UV fields up to 10^2–10^3 times the general interstellar radiation field are inferred in the outflow cavity walls on scales of the *Herschel* beam from various hydrides. Both high temperature chemistry and ice sputtering contribute to the gaseous water abundance at low velocities, with only gas-phase (re-)formation producing water at high velocities. Combined analyses of water gas and ice show that up to 50% of the oxygen budget may be missing. In cold clouds, an elegant solution is that this apparently missing oxygen is locked up in larger μm-sized grains that do not contribute to infrared ice absorption. The fact that even warm outflows and hot cores do not show H_2O at full oxygen abundance points to an unidentified refractory component, which is also found in diffuse clouds. The weak water vapor emission from disks indicates that water ice is locked up in larger pebbles early on in the embedded Class I stage and that these pebbles have settled and drifted inward by the Class II stage. Water is transported from clouds to disks mostly as ice, with no evidence for strong accretion shocks. Even at abundances that are somewhat lower than expected, many oceans of water are likely present in planet-forming regions. Based on the lessons for galactic protostars, the low-J H_2O line emission ($E_{\rm up} < 300$ K) observed in extragalactic sources is inferred to be predominantly collisionally excited and to originate mostly from compact regions of current star formation activity. Recommendations for future mid- to far-infrared missions are made.

Key words. astrochemistry – infrared: ISM – stars: formation – ISM: jets and outflows – ISM: molecules – protoplanetary disks

1. Introduction

Of the more than 200 detected interstellar molecules (McGuire 2018), water is special because it combines two of the most abundant elements in the Universe and plays a key role in the physics and chemistry of star- and planet-forming regions. On planets, water is widely acknowledged as essential for potential habitability and the emergence of life (Chyba & Hand 2005; Kaltenegger 2017). This makes the question of how much water is present in forming planetary systems, and whether this amount depends on the location and birth environment, highly relevant. Water ice also plays a role in promoting the coagulation of small dust grains to pebbles, rocks and ultimately planetesimals, the building blocks of planets, by enhancing the mass of solids due to freeze out. Such icy planetesimals (asteroids, comets), in turn, may have delivered much of the water and organic molecules trapped in ices to oceans on planets such as Earth that have formed inside the water iceline (see Morbidelli et al. 2012, 2018; van Dishoeck et al. 2014; Hartmann et al. 2017; Altwegg et al. 2019, for reviews).

In the early phases of star formation, water vapor is an exceptional tool for studying warm interstellar gas and the physical processes taking place during star formation. This diagnostic capability stems from water's large abundance variations between warm gas, where it is copiously produced (e.g., Draine et al. 1983; Kaufman & Neufeld 1996), and cold gas, where it is mostly frozen out (e.g., Bergin et al. 2002). Thus, water vapor emission can be used as a "beacon" that signals where energy is deposited into molecular clouds. This happens especially in the deeply embedded stages when jets and winds from the protostars interact with the surroundings, and when the (proto)stellar luminosity heats envelopes and disks. Water vapor lines are also particularly sensitive to small motions inside clouds, such as those that are due to gravitational collapse or expansion. Water[1] is therefore highly complementary to other molecules such as CO in probing the protostellar environment. Finally, water actively contributes to the energy balance of warm gas as a gas coolant, with its importance likely varying with protostellar evolution (Nisini et al. 2002).

The quest for understanding the water "trail" from clouds to planet-forming disks is complicated by the fact that water in the Earth's atmosphere prevents the direct observation of rotational lines of water gas with ground-based telescopes, except for some high excitation (masing) transitions and a few isotopolog lines. Indeed, the first detection of interstellar water was made from the ground through the 22 GHz water maser line in Orion (Cheung et al. 1969). Space-based observatories are needed to probe the full spectrum of water vapor. As a light hydride, water vapor has its principal rotational transitions at far-infrared rather than millimeter wavelengths, for which development of appropriate detector technology was required.

A related complication is the fact that star formation takes place over many size scales (Shu et al. 1993; Beuther et al. 2007): pc-sized clouds can fragment and contract to ~0.1 pc pre-stellar cores, which can subsequently collapse to form a protostar. Its envelope has a typical size of a few thousand au and feeds a growing disk of a few hundred au radius from which material can accrete onto the young star. Early in the evolution, the protostar will develop a bipolar jet and wind, which interact with their surroundings to create outflows on scales ranging from <0.01 up to 0.5 pc. Even in the nearest star-forming clouds at ~150 pc distance, these sizes range from many arcmin to <1 arcsec on the sky. A single-dish telescope in space with a spatial resolution of typically 0.5′ cannot resolve protoplanetary disks at far-infrared wavelengths, in contrast with what the Atacama Large Millimeter/submillimeter Array (ALMA) now does routinely at longer wavelengths. However, a single-dish telescope can image protostellar envelopes and their outflows. Motions range from <0.1 km s^{-1} to >100 km s^{-1} so that very high spectral resolution is needed to resolve line profiles which can typically only be provided by heterodyne instruments. This high spectral resolution allows to infer some spatial information for unresolved sources with systematic motions, such as for gas in rotating disks.

Pioneering infrared and submillimeter space missions have provided considerable insight into the water cycle in space. The Infrared Space Observatory (ISO; Kessler et al. 1996) covered the full mid- and far-infrared wavelength range observing both water gas and ice, but at modest spectral and spatial resolution and sensitivity. The Submillimeter Wave Astronomy Satellite (SWAS; Melnick et al. 2000) observed water with heterodyne spectral resolution in a 3.3′ × 4.5′ beam, but only through the ground-state line of ortho-H_2O and $H_2^{18}O$ near 557 and 547 GHz, as did the Swedish-led *Odin* satellite (Nordh et al. 2003). *Odin* had a factor of two higher angular (2′ circular beam) and spectral (0.5 MHz) resolution than SWAS, with spectra from these two missions agreeing very well when degraded to the same resolution (Larsson & Liseau 2017). Finally, the *Spitzer* Space Telescope (Werner et al. 2004) covered the mid-infrared wavelength range at low spatial and spectral resolution but with much higher sensitivity than ISO, thus probing both water ice and highly excited water gas. These missions, combined with the *Kuiper* Airborne Observatory and ground-based observations of water ice, have demonstrated that water is mostly frozen out as ice in cold clouds and that water vapor becomes abundant at high temperatures such as associated with outflows. Detailed results from these missions are summarized elsewhere and will not be repeated here (see e.g., Melnick 2009; Hjalmarson et al. 2003; van Dishoeck 2004; van Dishoeck et al. 2013; Pontoppidan et al. 2010b).

The *Herschel* Space Observatory (Pilbratt et al. 2010) covered the 55–672 μm range and improved on previous space missions in all relevant observational parameters. With a 3.5 m telescope, its diffraction-limited beam ranged from 44″ at the longest to 9″ at the shortest wavelengths, increasing the spatial resolution with respect to *SWAS* at the longest wavelengths by a factor of 5 and making it a much better match to the sizes of protostellar sources. Its Heterodyne Instrument for the Far-Infrared (HIFI; de Graauw et al. 2010) provided spectra at very high spectral resolution ($R = \lambda/\Delta\lambda$ up to 10^7) at a single position over the 480–1250 GHz (600–240 μm) and 1410–1910 GHz (210–157 μm) ranges, thus covering many water lines and fully resolving their profiles. The Photodetector Array Camera and Spectrometer (PACS, Poglitsch et al. 2010) obtained spectra with moderate resolving power ($R = (1-5) \times 10^3$) in the 55–190 μm range at each pixel of a 5 × 5 array allowing efficient instantaneous imaging of water lines and full far-infrared spectral scans. The sensitivity of both HIFI and PACS was a factor of >10–100 better than previous missions due to improved detector technology and increase in collecting area. The combination of these two instruments made *Herschel* eminently suited to study both hot and cold water in space. The Spectral and Photometric Imaging Receiver (SPIRE; Griffin et al. 2010) also covered some of the lower-frequency water and CO lines at 194–318 and

[1] Unless specified, the term "water" in this article can imply both water vapor and water ice. The term "ice" is used to indicate all volatiles in solid form, which includes – but is not limited to – water ice.

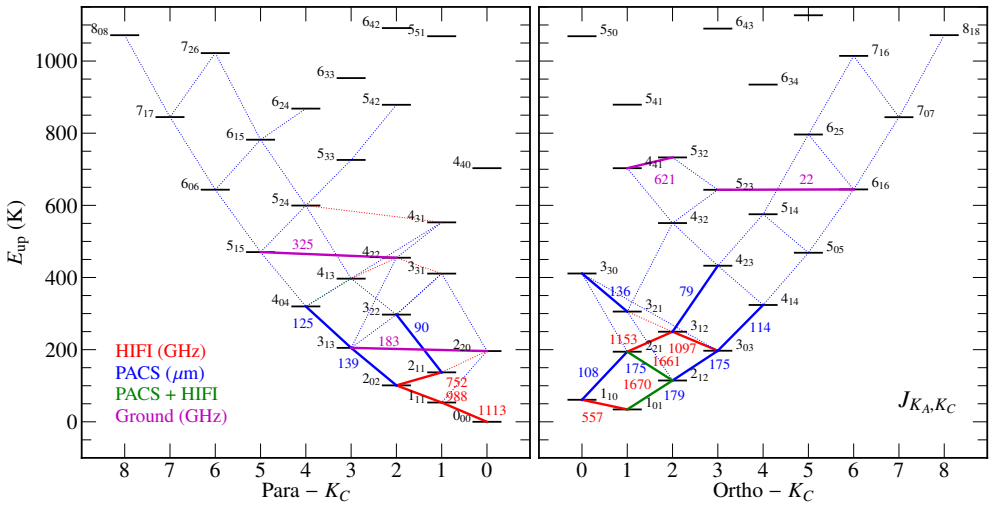

Fig. 1. Water rotational energy levels within the ground vibrational level. Transitions targeted with HIFI are indicated in red with frequencies in GHz, those with PACS in blue with wavelengths in μm. Dashed lines indicate water transitions detected in PACS and HIFI spectral scans. The 179 μm line observed with both PACS and HIFI is indicated in green. Purple lines indicate water (isotopolog) lines that can be observed from the ground with frequencies in GHz; some of them (e.g., 621 GHz) have also been observed with HIFI. The 22 GHz 6_{16}–5_{23} maser line observed at cm wavelengths is indicated.

294-672 μm but at much lower spectral resolution than HIFI and was generally not used as part of WISH.

The goal of the Water In Star-forming regions with *Herschel* (WISH) guaranteed time Key Program (KP) was to use water vapor as a physical and chemical diagnostic and follow the water abundance throughout the different phases of star- and planet formation. A sample of about 80 young stellar objects (YSOs) was targeted covering two axes: mass and time (or equivalently, evolutionary stage). The WISH sources have luminosities from <1 to >10^5 $L_\odot$, thus including low (LM), intermediate (IM) and high mass (HM) protostars. They also cover a large range of evolutionary stages, from pre-stellar cores prior to collapse, through the embedded protostellar stages, to the revealed phase when the envelope has dissipated and – for the case of low-mass sources – the pre-main sequence stars become optically visible but are still surrounded by gas-rich disks. The full list of sources is included as Table 1 in van Dishoeck et al. (2011), which also describes the WISH program and highlights initial results. The gas-poor debris disk stage was not covered in WISH but was targeted spectroscopically by other programs such as GASPS (Dent et al. 2013).

The WISH program was organized along the mass and time axes (see Table A.1 in the Appendix) with slightly different observing strategies for each of the subprograms. For all embedded protostars, a comprehensive set of water observations has been carried out with HIFI and PACS (Fig. 1) with a mix of low- and high-excitation lines of H_2O, $H_2^{18}O$, $H_2^{17}O$, and the chemically related species O and OH, targeted. In addition, a number of high-J CO and its isotopologs lines are included in the spectral settings, as are some hydrides and C^+ that are diagnostic of the presence of X-rays or UV that are emitted either by the source itself or at the star-disk interface (see Table 2 in van Dishoeck et al. 2011). Thus, the WISH data also cover the major coolants of the gas. For the cold pre-stellar cores and protoplanetary disks, at most a few water lines were observed but with very long integrations. Later in the *Herschel* mission, when additional guaranteed time became available, some HDO lines were added, since the HDO/H_2O ratio is a particularly powerful tracer of the water chemistry and its history. The 1_{11}–0_{00} line of HDO at 893 GHz is a particularly powerful probe of cold HDO gas.

Since the WISH sample was limited in the number of sources in each luminosity or evolutionary bin, several follow-up open time programs have been pursued to validate the conclusions. For example, the *William Herschel* Line Legacy survey (WILL) doubled the number of low-mass protostars in a much more unbiased way (Mottram et al. 2017). A program targeting all protostars in the Cygnus star-forming cloud added greatly to the intermediate- and high-mass samples (San José-García 2015). Very deep integrations on a number of protoplanetary disks allowed more general conclusions for those sources to be drawn (Du et al. 2017). Similar extensions hold for many of the WISH subprograms, the most important of which are summarized in Table A.1. The collection of WISH and these programs is indicated here as WISH+.

Complementary guaranteed and open time *Herschel* programs have provided information on water in star-forming regions as well, most notably the HIFI spectral surveys as part of the CHEmical Survey of Star-forming regions (CHESS; Ceccarelli et al. 2010) and Herschel observations of EXtraOrdinary Sources (HEXOS; Bergin et al. 2010b) KPs. The Dust, Ice and Gas in Time (DIGIT; Green et al. 2013) and Herschel Orion Protostar Survey (HOPS; Manoj et al. 2013) KPs complemented WISH by carrying out full PACS spectral scans for a larger sample of low-mass embedded YSOs. The PRobing InterStellar Molecules with Absorption line Studies (PRISMAS) targeted the chemistry of water and other hydrides in the diffuse interstellar gas (Gerin et al. 2016). At the other end of the water trail, the Water and related chemistry in the Solar System (HSSO; Hartogh et al. 2009) probed water and its deuteration in a variety of solar system objects, including comets. Some of their results will be put in the context of the WISH+ program.

The main aims of the WISH program are to determine:

(i) How and where water is formed in space.

(ii) Which physical components of a star-forming cloud water traces, and what the water abundances are in each of these components. Also, what fraction of the total oxygen reservoir is accounted for by water, and what the importance is of water vapor as a coolant of warm gas.

(iii) What the water trail is from clouds to disks, and ultimately to comets and planets.

Overall, WISH+ has published nearly 90 papers to date which are summarized on the WISH website[2]. This paper synthesizes these WISH+ results, together with related results from the above mentioned *Herschel* programs. It focuses on questions (i) and (iii) and the latter part of question (ii), including previously unpublished data, new models and new analyses. The physical components traced by water vapor have been addressed in a number of synthesis papers, most notably San José-García et al. (2016), Herpin et al. (2016), van der Tak et al. (2019), Kristensen et al. (2017b) and Mottram et al. (2017) for WISH+, Karska et al. (2018) for WISH+WILL+DIGIT, and Manoj et al. (2016) for HOPS+DIGIT, with the latter paper limited to CO.

In terms of question (iii), this paper describes the evolution of water from cores to disks. The bigger picture of the delivery of water to planets and Earth itself is summarized in other reviews (e.g., van Dishoeck et al. 2014; Morbidelli et al. 2018). Also, this paper is centered around *Herschel*'s contributions to these questions. Other facilities provide important complementary information, most notably ground-based infrared telescopes on ices (e.g., Boogert et al. 2015), and millimeter interferometers such as ALMA and the Northern Extended Millimeter Array (NOEMA) through high resolution images of quiescent warm water in protostellar sources (e.g., van der Tak et al. 2006; Persson et al. 2014; Harsono et al. 2020), but they will be mentioned only sparsely.

This paper is organized as follows. Section 2 summarizes the main observing strategy, sample selection and data reduction. Section 3 and Appendix D provide an overview of the main water formation and destruction processes, especially those that are relevant for star-forming regions. Also, the WISH modeling approach is outlined. Section 4 summarizes the main results of *Herschel* WISH+ and related programs on water, especially its distribution, line profiles and excitation, and links them to observations of the CO rotational ladder. The inferred characteristics hold universally from low- to high-mass protostars. Section 5 describes the surprisingly low water abundance inferred for the different types of warm outflowing gas and shocks associated with star-forming regions and the implications for shock models. Comparison is made with chemically related molecules such as OH observed with *Herschel* and shock tracers such as SiO and grain surface products such as CH_3OH.

Sections 6–9 follow water from pre-stellar cores through protostars to disks for low- and high-mass sources. Section 6 focuses on the cold pre-stellar cores, whereas Sect. 7 describes similar results for the outer cold protostellar envelopes using the high-resolution HIFI line profiles to infer the water abundance profile as a function of position in the envelope. New analyses of HDO and NH_3 (another grain surface chemistry product) are presented. Section 8 highlights the puzzling low water abundances in the inner hot core of several protostellar envelopes where all ices should have sublimated. Section 9 focuses on recent new results on water in young and mature disks around pre-main sequence stars, setting the stage for planet formation. Section 10 and Appendix G bring all the information on oxygen reservoirs in star-forming regions together and compare them with diffuse clouds and comets to address the puzzling question of the missing oxygen. Section 11 concludes with a discussion and overview of what we have learned from *Herschel* on the above water questions, from low to high-mass protostars, and from clouds to disks. Section 12 summarizes the main points in bullet form and looks forward to future observations of warm water using ALMA, the *James Webb* Space Telescope (JWST) and Extremely Large Telescopes (ELTs) on the ground and in space, as well as surveys of water ice using the SPHEREx mission. It also makes recommendations for future far-infrared space mission concepts such as the Space IR telescope for Cosmology and Astrophysics (SPICA; Roelfsema et al. 2018) and the Origins Space Telescope (Meixner et al. 2019). For deep observations of cold water vapor, the WISH+ *Herschel* data will remain unique for a long time.

2. Observations

2.1. Observed lines

Water is an asymmetric rotor with energy levels characterized by the quantum numbers J_{K_A,K_C}, grouped into ortho ($K_A + K_C$ = odd) and para ($K_A + K_C$ = even) ladders because of the nuclear spin statistics of the two hydrogen atoms. In contrast with CO, its energy level structure is highly irregular, resulting in transitions scattered across the far-infrared and submillimeter wavelength range. Figure 1 summarizes the $H_2^{16}O$ lines in the vibrational ground state that were targeted by WISH using HIFI and PACS. Also, water lines serendipitously detected in full spectral scans are indicated. The full list of lines, including isotopologs and related species, is summarized in Table 2 of van Dishoeck et al. (2011). To this list, the HDO $1_{11}-0_{00}$ 893.639 GHz line has been added for a number of embedded protostars and the H_2O $5_{24}-4_{31}$ line at 970.3150 GHz (E_{up} = 599 K)[3] for high-mass sources.

The targeted water vapor lines were chosen to cover both low- and high-energy levels as well as a range of opacities in three groups. First, lines connected with the ground state levels of o- and p-H_2O at 557, 1113, and 1670 GHz[4] are prime diagnostics of the cold gas. They usually show strong self-absorption or can even be purely in absorption against the strong continuum provided by the source itself (Fig. 2).

The second group, the 'medium-J' lines originating from levels with E_{up} around 100–250 K, probe the warm gas and are not (or less) affected by absorption. The $2_{02}-1_{11}$ line at 988 GHz, $3_{12}-3_{03}$ at 1097 GHz, and $3_{12}-2_{21}$ at 1153 GHz (for LM and IM sources), are particularly useful; the latter two lines originate from the same upper level but have Einstein A coefficients that differ by a factor of 6.3. Because of high optical depths of $H_2^{16}O$, optically thin(ner) isotopic lines are crucial for the interpretation. Thus, deep integrations on a number of ground-state and medium-J $H_2^{18}O$ and $H_2^{17}O$ lines are included in WISH for embedded sources. They proved to be particularly useful for the high-mass protostars. For the low-mass subsample, $H_2^{18}O$ specific settings were only observed toward Class 0 sources which have brighter lines than the Class I sources. No water lines had been seen prior to *Herschel* for Class I sources, so longer integrations were put on the $1_{10}-1_{01}$ 557 GHz transition to ensure detections.

The third group are highly excited lines originating from levels >300 K, which are only populated in high temperature gas and strong shocks (e.g., higher-lying backbone lines). Most of these lines are covered by PACS in its individual line scan mode and are thus not velocity resolved. They have E_{up} up to 1324 K at the shortest PACS wavelengths (Herczeg et al. 2012), which is high in energy, but not yet high enough to probe the hottest shocked gas seen at mid-infrared wavelengths

[2] www.strw.leidenuniv.nl/WISH

[3] Energies of levels are indicated in short as E_{up} in K units rather than E_{up}/k_B with k_B the Boltzmann constant.

[4] Frequencies are abbreviated to values commonly used to designate these lines in the WISH papers. They may differ by 1 GHz from the properly rounded values.

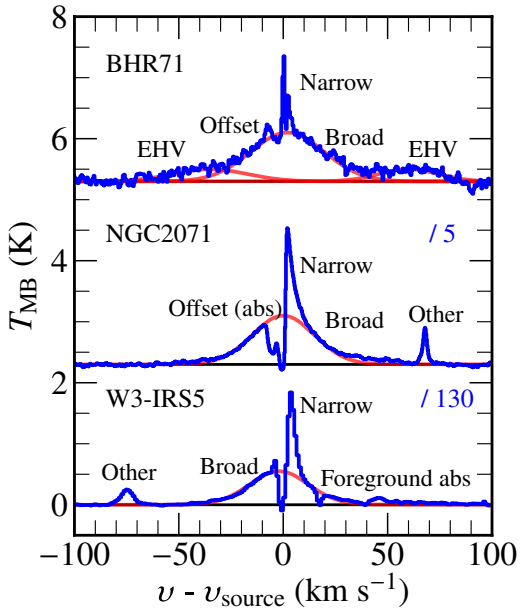

Fig. 2. Water spectra of the 1_{10}–1_{01} 557 GHz line taken with *Herschel*-HIFI (38″ beam) toward a low-, intermediate- and high-mass YSOs (*top to bottom*). The spectra highlight the complexity of water profiles with multiple kinematic absorption and emission components (see text and Table 1 for the interpretation of these components). Other refers to lines from molecules other than H_2O.

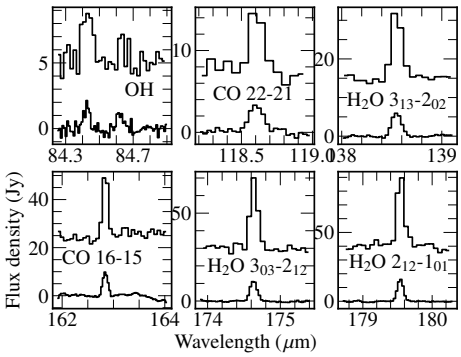

Fig. 3. Examples of PACS spectra of NGC 1333 IRAS 4B with the same spectrum shown twice in each panel: (*top*) taken in the full spectral scan mode at Nyquist sampling; (*bottom*) taken in individual line scan mode, which has a factor 3 higher spectral sampling.

(e.g., Melnick et al. 2008). The PACS spectra also cover many OH lines and the two [O I] fine-structure lines. Full PACS spectral scans were obtained for four low-mass WISH sources to provide an unbiased view of all the far-infrared lines. Both modes have the same spectral resolving power, but the spectral sampling for full scans is much lower than that for individual line scans. Combined with the shorter integration time per line, this affects the quality of individual line spectra in full spectral scans as illustrated in Fig. 3.

CO lines are included in the HIFI settings up to the $J = 10$–9 transition ($E_{up} = 304$ K), both of the main and minor CO isotopologs (Yıldız et al. 2013b; San José-García et al. 2013). As described in Sect. 4, these lines are not yet high enough in energy to probe the same physical components as the mid-J water lines. The important CO $J = 16$–15 ($E_{up} = 752$ K) does so and was targeted in a separate program, COPS-HIFI (Kristensen et al. 2017b). PACS covers CO lines starting at $J = 14$–13 up to $J = 49$–48 with $E_{up} = 6725$ K (Herczeg et al. 2012; Goicoechea et al. 2012), so there is a small overlap to connect PACS and HIFI for CO ladder observations.

PACS provides small 5×5 maps over a $\sim 1' \times 1'$ region for all sources. Additional, sometimes larger, maps were made with HIFI and PACS of selected water and CO lines together with the continuum for a few selected low-mass (e.g., Nisini et al. 2010; Bjerkeli et al. 2012) and high-mass protostars (e.g., Jacq et al. 2016; Leurini et al. 2017; Kwon et al. 2017).

Simple hydrides such as CH^+, OH^+, and H_2O^+, also have their lowest transitions at far-infrared wavelengths that can be observed with *Herschel*. Since these molecules are either part of the water network, have formation pathways that involve energy barriers or are dissociation products, they provide complementary information on the chemistry, gas temperatures and the irradiation by far-UV or X-rays and were therefore included in WISH. Moreover, HCO^+, an ion whose main destroyer is water, is serendipitously covered through its $J = 6$–5 line in the WISH $H_2^{18}O$ 1_{10}–1_{01} setting.

Even though WISH had a generous guaranteed time allocation of 425 h, a trade-off between number of sources, lines and integration times per line had to be made. Integration times range from as little as 10–15 min per line for embedded protostars with bright water emission, to 10–20 h per setting to detect the very weak water lines from cold pre-stellar cores and protoplanetary disks.

2.2. Sample

The WISH KP source sample of ~80 sources is summarized in Table 1 of van Dishoeck et al. (2011), with updates on source distances and luminosities listed in Table 1 of Kristensen et al. (2012) for low-mass and Table 1 of van der Tak et al. (2019) for high-mass protostars. Spectral energy distributions (SEDs) of most sources, including updated far-infrared fluxes from *Herschel*, are presented in Kristensen et al. (2012); Karska et al. (2013); van der Tak et al. (2013); Green et al. (2013); Mottram et al. (2017).

WISH selected its source samples among well known archetypal sources, based on a wide array of complementary data. The program distinguishes low (LM, $<10^2$ $L_\odot$), intermediate (IM, 10^2–10^4 $L_\odot$) and high-mass (HM, $>10^4$ $L_\odot$) protostars. Also, for a subset of low-mass protostars, positions in the outflow, well separated from the source, were targeted in a separate subprogram. In terms of evolutionary stages, pre-stellar cores, embedded protostars (both Class 0 and Class I, separated by T_{bol} < and >70 K, Evans et al. 2009), and pre-main sequence stars with disks (Class II), are included. For high mass protostars, the evolutionary stages range from Infrared Dark Clouds (IRDC) to High-Mass Protostellar Objects (HMPO, both IR "quiet" and IR bright) to UltraCompact H II regions (UC HII), although the latter two stages have some overlap (Beuther et al. 2007; Motte et al. 2018).

The WISH sample favors luminous sources with particularly prominent and extended outflows in the case of low-mass sources. The latter was a requirement to be able to target separate on-source and off-source positions in the outflow subprogram. As demonstrated by other *Herschel* programs such as WILL and DIGIT, such large extended outflows are not representative of the general population of low-mass protostars (Mottram et al. 2017; Karska et al. 2018). All WISH conclusions have, however, been verified by these additional samples.

The number of sources per WISH (sub)category ranges from a few for the cold line-poor sources (pre-stellar cores, disks) to 10–20 for warm line-rich objects. The latter samples are large enough to allow individual source peculiarities to be distinguished from general trends. The radiation diagnostics subprogram observed hydrides other than H_2O in a subsample of low- and high-mass protostars. As noted above, the number of sources per subcategory has in many cases been more than doubled thanks to the additional programs listed in Table A.1. Details of the observations and data reduction are summarized in Appendix B.

3. Water chemistry

3.1. Overall oxygen budget

For the interpretation of the *Herschel* data, it is important to compare observed water abundances with the maximum water abundance that can be expected based on the available elements in interstellar gas. The average abundance of elemental oxygen with respect to total hydrogen nuclei in the interstellar medium is measured to be $[O] = 5.8 \times 10^{-4}$ (Przybilla et al. 2008), with an uncertainty of about 20%. This value is close to the current best estimate of the solar oxygen abundance of 4.9×10^{-4} (Asplund et al. 2009; Grevesse et al. 2010) and nearly identical to the solar system value (Lodders 2010). The notation [X] indicates the abundance of element X in all its forms. Some fraction of this oxygen, $(0.9-1.4) \times 10^{-4}$ (16–24%), is locked up in refractory silicate material in the diffuse interstellar medium (Whittet 2010). The abundance of volatile oxygen (that is, the oxygen not tied up in some refractory form) is measured to be 3.2×10^{-4} in diffuse clouds (Meyer et al. 1998), so this is the maximum amount of oxygen that can cycle between water vapor and ice in dense clouds.

Counting up all the forms of detected oxygen in diffuse clouds, the sum is less than the overall elemental oxygen abundance. This missing fraction increases with density (Jenkins 2009). Thus, a fraction of oxygen is postulated to be in some yet unknown refractory form, called Unidentified Depleted Oxygen (UDO), which may increase from ~20% in diffuse clouds up to 50% in dense star-forming regions (Whittet 2010; Draine & Hensley 2020). For comparison, the abundance of elemental carbon is 3×10^{-4}, with about 50–70% of the carbon thought to be locked up in solid carbonaceous material (Henning & Salama 1998). If CO (gas + ice) contains the bulk of the volatile carbon, its fractional abundance should thus be about 1×10^{-4} with respect to total hydrogen, thus accounting for up to 30% of the volatile oxygen. Indeed, direct observations of warm CO and H_2 gas provide a maximum value of $CO/[H] = 1.4 \times 10^{-4}$ (Lacy et al. 1994), that is, a little less than half the volatile oxygen. Subtracting the amount of oxygen in CO from 3.2×10^{-4} leaves $\sim 2 \times 10^{-4}$ for other forms of volatile oxygen in dense clouds.

Often water abundances are cited with respect to H_2 rather than total hydrogen. Thus, the maximum expected abundance if most volatile oxygen is driven into water is $H_2O/H_2 = 4 \times 10^{-4}$, with $H_2O/CO \approx (1.4-2)$. This maximum H_2O abundance takes into account the fraction of oxygen locked up in CO and silicates (at 24%), as well as a minimal 20% fraction of UDO such as found in diffuse clouds. A more detailed discussion of the oxygen budget can be found in Sect. 10 and Appendix G.

3.2. Simplified water chemistry networks

Detailed networks of the water chemistry in the gas and on the grains are presented in van Dishoeck et al. (2013) and Lamberts et al. (2013), and the three main routes to water are described in Appendix D: (i) cold ion-molecule chemistry; (ii) high-temperature gas-phase chemistry; and (iii) ice chemistry. In addition, the link between the water network and that forming CO_2, another potentially significant oxygen carrier, is described there. The main reactions are illustrated in Fig. 4.

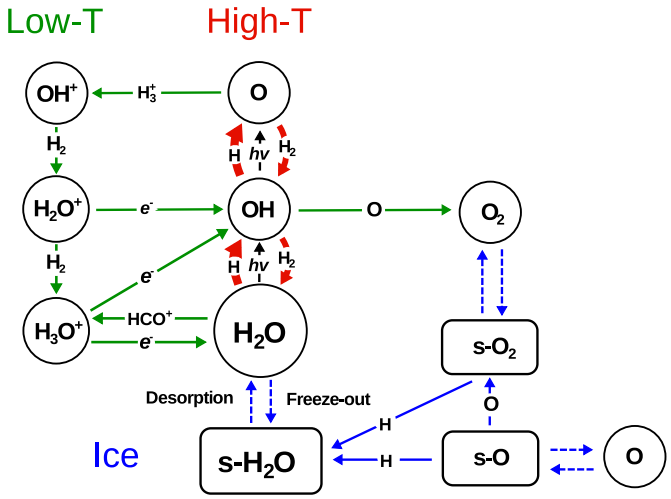

Fig. 4. Simplified gas-phase and solid-state reaction network leading to the formation and destruction of H_2O. s-X denotes species X on the ice surface. Three routes to water can be distinguished: (i) ion-molecule gas-phase chemistry which dominates H_2O formation at low temperatures and low densities (green); (ii) high-temperature neutral-neutral chemistry which is effective above ~250 K when energy barriers can be overcome (red); and (iii) solid-state chemistry (blue). The full solid-state network is presented in Lamberts et al. (2013). Chemically related molecules discussed in this paper such as OH, O_2 and HCO^+ are shown as well.

For coupling chemistry with detailed physical or hydrodynamical models, often smaller chemical networks are preferred to make such calculations practical and computationally feasible for large grids of models. Moreover, these simple models often allow the key physical and chemical processes to be identified. Two independent simple water chemistry models have been developed within WISH, that by Keto et al. (2014) for cold pre-stellar cores and the SWaN (Simple Water Network) model for protostellar envelopes by Schmalzl et al. (2014). They include only a few of the reactions shown in Fig. 4: (a) cycling of water from gas to ice through freeze-out and UV photodesorption; (b) photodissociation of gaseous water to OH and atomic O, and (c) grain-surface formation of water ice from atomic O.

The Keto et al. (2014) model explicitly includes gaseous OH as an intermediate channel, as well as the high temperature O + H_2 and OH + H_2 reactions, although the latter reactions never become significant in cold cores. The SWaN model ignores all OH reactions, but explicitly includes thermal desorption of water in the hot core region above 100 K.

Both simplified models have been extensively tested against the full water chemistry models of Hollenbach et al. (2009) (see Figs. 3 and 4 of Keto et al. 2014) and those of Visser et al. (2011), Walsh et al. (2012) and Albertsson et al. (2014) (see Fig. B.2 of Schmalzl et al. 2014). While differences of factors of a few in absolute abundances can readily occur, the overall profiles are similar and robustly seen in all models as long as the same physical and chemical parameters are adopted.

Multilayer ice models such as developed by Taquet et al. (2014) and Furuya et al. (2016) predict similar abundance profiles

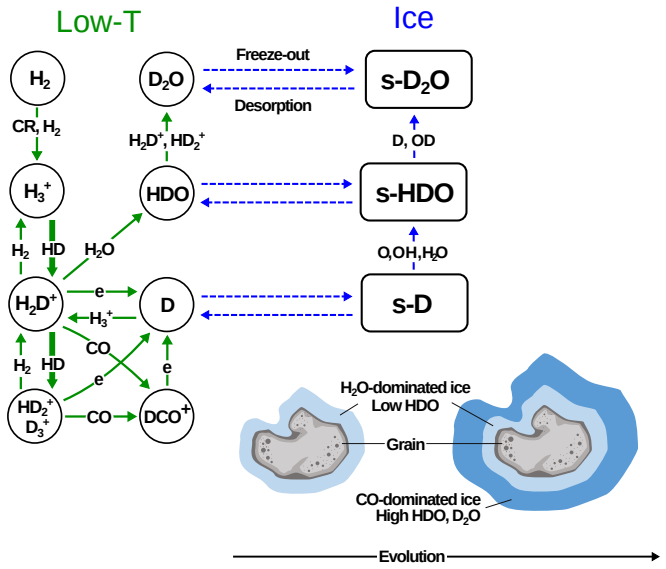

Fig. 5. Simplified reaction network illustrating the important reactions in the deuteration of water and other molecules. The left-hand side illustrates the cold gas-phase chemistry, leading to high fractionation of gaseous H_2D^+ and atomic D, and ultimately gaseous HDO and D_2O. The right-hand side illustrates how this enhanced D ends up on the ice and leads to enhanced solid HDO and D_2O. The bottom cartoon shows the different ice layers on a grain: the H_2O-dominated layer formed early in the cloud evolution with low HDO/H_2O < 10^{-3}, and the CO-dominated layer formed at higher densities which is rich in deuterated water, with D_2O/HDO>>HDO/H_2O (Furuya et al. 2015).

of water as the two-phase simple SWaN models do, but differences in absolute water abundances can be introduced because multilayer interstellar ices are inhomogenous.

To compare models with observations, not just the water chemistry but also the water excitation and radiative transfer need to be treated correctly. The various methods and modeling approaches adopted by WISH are described in Sect. 4.4 and Appendix F.

3.3. Water deuteration

Deuterated water, HDO and D_2O, is formed through the same processes as shown in Fig. 4 but there are a number of chemical reactions that can enhance the HDO/H_2O and D_2O/H_2O ratios by orders of magnitude compared with the overall [D]/[H] ratio of 2.0×10^{-5} found in the local interstellar medium (Prodanović et al. 2010). Details can be found in Taquet et al. (2014) and Furuya et al. (2016), and in Ceccarelli et al. (2014) for deuterium fractionation in general (see also Sect. 7.3). The processes are illustrated in Fig. 5. The most effective water fractionation occurs on grains, due to the fact that the relative number of D atoms landing from the gas on the grain is enhanced compared with that of H atoms. In other words, atomic D/H in cold gas is much higher than the overall [D]/[H] ratio (Tielens 1983; Roberts et al. 2003). This high D/H ratio landing on grains naturally leads to enhanced formation of OD, HDO and D_2O ice according to the grain-surface formation routes.

The high atomic D/H ratio in the gas, in turn, arises from the well-known fractionation reactions initiated by the H_3^+ + HD → H_2D^+ + H_2 reaction, which is exoergic by ~230 K and is thus very effective at low temperatures ≤25 K (e.g., Watson 1976; Aikawa & Herbst 1999; Stark et al. 1999; Sipilä et al. 2015). The H_2D^+ abundance is further enhanced when the ortho-H_2 abundance drops (preventing the back reaction) and when the main H_3^+ and H_2D^+ destroyer, CO, freezes out on the grains (Pagani et al. 1992, 2009; Roberts et al. 2003; Sipilä et al. 2010). The latter processes become more important as the cloud evolves from a lower density to a higher density phase (Dartois et al. 2003; Pagani et al. 2013; Brünken et al. 2014; Furuya et al. 2015). Dissociative recombination of H_2D^+ and other ions such as HD_2^+, D_3^+ and DCO^+ with electrons then produces enhanced atomic D which gets incorporated in the ices (Fig. 5). As a result, the outer ice layers, which are produced when the cloud is denser and colder, have higher HDO/H_2O ratios – by orders of magnitude – than the inner layers and the bulk of the ice. The enhanced H_2D^+ also leads to enhanced H_2DO^+ and thus HDO in cold gas, which may play a role at the lower density edge of the cloud.

Another characteristic of this layered ice chemistry is that the D_2O/HDO ratio is much higher than the HDO/H_2O ratio (Furuya et al. 2016). Moreover, the deuteration of organic molecules formed through hydrogenation of CO ice in the later cloud stages is generally much higher than that of water (Cazaux et al. 2011; Taquet et al. 2014; Furuya et al. 2016).

The desorption processes – photodesorption at low ice temperatures (Öberg et al. 2009; Arasa et al. 2015; Cruz-Diaz et al. 2018) and thermal desorption at high ice temperatures – have a small to negligible effect on the deuterium fractionation. In other words, the gaseous HDO/H_2O and D_2O/H_2O ratios should reflect the ice ratios following desorption if no subsequent gas-phase reactions are involved. It is important to note that photodesorption is only effective in the outer few layers of the ice, whereas thermal desorption removes the bulk ice mantle. This selective formation and removal of ice layers turns out to be important in the interpretation of HIFI observations of HDO/H_2O ratios in cold versus warm gas.

In warm gas, the exchange reaction D + OH → H + OD is likely barrierless and can be effective in enhancing OD, especially since the reverse reaction seems to have a barrier of around 800 K (Thi et al. 2010). Photodissociation of HDO can also enhance OD compared with OH by a factor of 2–3, which could be a route to further fractionation. Finally, in high temperature gas in disks the exchange reaction H_2O + HD ↔ HDO + H_2 is often included. Similarly, there are reactions inside the ices that can both enhance and reduce the water fractionation (Lamberts et al. 2015, 2016) but are not considered here (see discussion in Furuya et al. 2016).

4. Herschel water spectra and maps

In this section, we briefly summarize the main features characterizing water emission observed with *Herschel*, largely based on WISH+ programs. Figure 2 illustrates the complexity of individual water profiles for protostars observed with HIFI over more than ±50 km s^{-1} whereas Fig. 6 shows the spatial distribution imaged with PACS. Figure 7 presents examples of full spectral scans with PACS with many lines detected. The main conclusion from the combined analysis of the water maps, the broad water line profiles, and its excitation, is that most of the observed gaseous water is universally associated with warm outflowing and shocked gas of several hundred K. All water lines observed by *Herschel* within WISH show thermal emission, so nonmasing, in contrast with the 22 GHz maser often associated with star-forming regions. At least two different types of kinematic components are involved, with water being a significant (but not necessarily dominant) coolant. In contrast, water emission is not

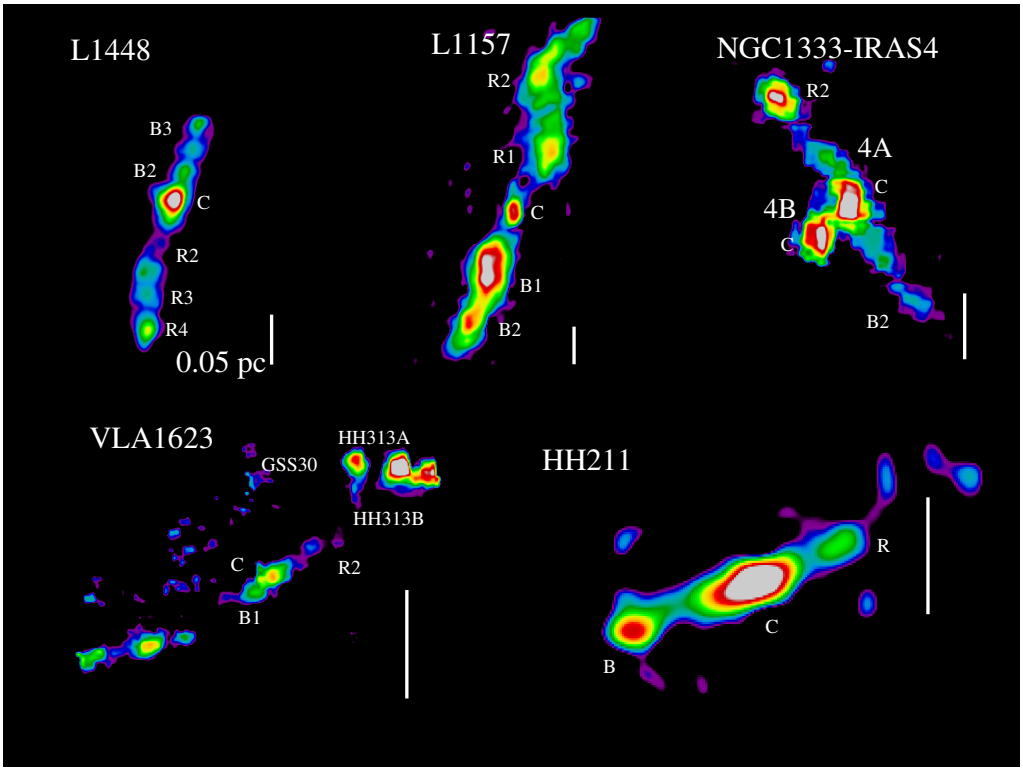

Fig. 6. Gallery of water maps in the $2_{12}-1_{01}$ 179 μm line made with *Herschel*-PACS of the low-mass outflow sources L1448-MM ($d = 235$ pc), L1157 (325 pc), NGC 1333 IRAS 4 (235 pc), VLA1623 (140 pc) and HH211 (250 pc). The white bars indicate a 0.05 pc scale. The central sources are indicated by C, with coordinates and details of data given by Nisini et al. (2010, 2013); Bjerkeli et al. (2012); Santangelo et al. (2014a,b); Dionatos et al. (2018).

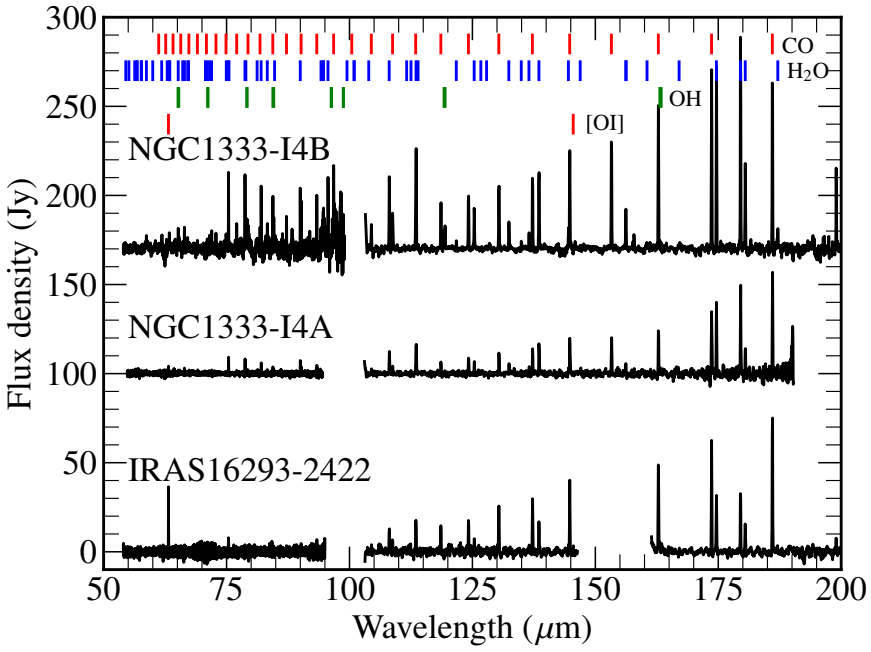

Fig. 7. Full PACS spectral scans of the low-mass protostars NGC 1333 IRAS 4B (Herczeg et al. 2012) and IRAS 1333 IRAS 4A, both taken as part of WISH, compared with that of IRAS 16293-2422, taken as part of CHESS. The IRAS 4B spectrum, which is extracted at the offset and localized shock position just south of the protostar, is much richer in lines than the other two sources, likely because of less extinction at far-infrared wavelengths in the blue outflow lobe.

associated with the slower, colder entrained outflow gas traced by low-J CO line wings.

Cold quiescent water vapor is also detected but is primarily seen in absorption at the protostellar position; only very few cloud positions show weak narrow (FWHM $\lesssim$ few km s^{-1}) water emission lines. These are further discussed in Sect. 7. Recall that *Herschel* does not observe the bulk of water in cold clouds directly, since this is locked up in ice.

4.1. Water maps of outflows

Figure 6 presents maps in the H_2O 179 μm line imaged over several arcmin scales at ~13″ resolution with *Herschel*-PACS for a number of low-mass sources (Nisini et al. 2010, 2013; Santangelo et al. 2014b; Dionatos et al. 2018). Water vapor emission is clearly associated with the powerful large scale outflows from these sources. Close inspection shows, however, that the

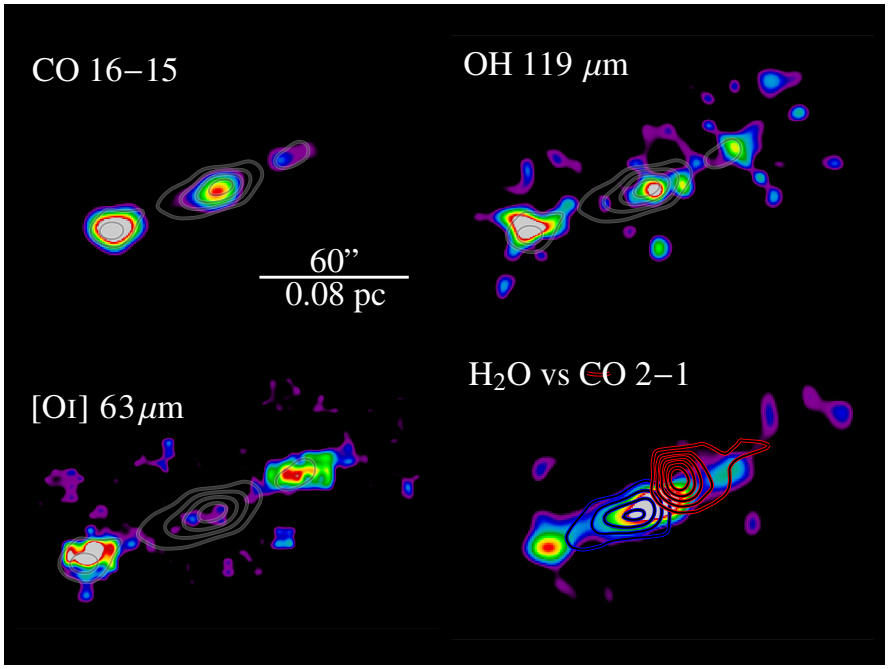

Fig. 8. Map of the water 179 μm emission in the blue outflow lobe of the HH 211 low-mass Class 0 source ($L_{\rm bol} \approx 3.6\,L_\odot$, $d = 250$ pc) compared with that of other lines observed with *Herschel*-PACS. The color maps present, from left to right: a high-J CO line, the OH 119 μm doublet, the [O I] 63 μm line and the H_2O 179 μm line overlaid with a low-J CO ($J = 2$–1) line. The H_2O map is overlaid in light gray contours on the other panels. Note the similarity between the H_2O and CO high-J maps, but not with CO low-J. Data from Tafalla et al. (2013); Dionatos et al. (2018).

water emission is systematically shifted from that of low-J CO emission commonly used to trace outflows (e.g., Tafalla et al. 2013): water only spatially coincides with maps of the higher-J CO lines with $J_{\rm up} > 14$ and with the H_2 mid-IR lines S(1)–S(4) (e.g., Nisini et al. 2013; Bjerkeli et al. 2012; Santangelo et al. 2014a,b; Neufeld et al. 2014) (Fig. 8). Thus, water and high-J CO probe a fundamentally different gas component than that commonly studied with low-J CO lines. This also limits the use of low-J CO lines to determine, for example, abundances in shocked gas (Sect. 5).

Bright compact water emission is seen at the central protostar position, in contrast with the thermal emission from other molecules that are associated with outflows such as SiO and CH_3OH. This suggests an additional production route of water in the warm inner protostellar envelope beyond thermal desorption of ices. Along the outflow, the water emission is clumpy, with unresolved individual peaks (at the 13″ resolution of the 179 μm line) corresponding to shock spots. In addition, weaker more extended water emission is observed.

The [O I] 63 μm line is commonly associated with jets powering the outflows. Indeed, *Herschel*-PACS maps show strong [O I] emission along the outflow direction (Fig. 8). In some cases (∼10% of sources) even velocity resolved PACS spectra have been seen, indicating speeds of more than 90 km s^{-1} with respect to that of the source, characteristic of jets (e.g., van Kempen et al. 2010; Nisini et al. 2015; Dionatos & Güdel 2017; Karska et al. 2018). Comparison of mass flux rates from [O I] and CO suggests that this atomic gas is not the dominant driver in the earliest stages: the jets in the Class 0 phase are mostly molecular. However, toward the Class I stage, the jets become primarily atomic, and ultimately ionized in the Class II stage.

The HH 211 outflow shown in Fig. 8 is an example of a source where the atomic jet has just enough momentum to power the molecular jets and the large scale outflow (Dionatos et al. 2018). Maps in the chemically related OH molecule exist for only a few sources and usually show more compact emission than that of water. In the case of HH 211, OH peaks primarily on source and at the bow-shock position. It is important to note that HH 211 is the only protostellar source which was mapped completely with *Herschel*-PACS full spectral scans. All other outflows were only mapped in selected lines.

The sources included in Fig. 6 represent those with well-known extended outflows; the WISH low-mass protostar sample contains a relatively large fraction of them. However, this is not representative of the low-mass population. As noted in Sect. 2.2, the bulk of the low-mass Class 0 and I sources in the full WISH+WILL+DIGIT sample show little or no extended emission beyond the central PACS 13″ spaxel: out of 90 sources only 18 show extended water emission in the 47″ PACS footprint (Karska et al. 2013, 2018). This means that the currently active mechanism exciting water in the bulk of the sources is limited to a ∼1000 au radius from the central source. The same conclusion holds for higher mass sources (e.g., Leurini et al. 2017). Even in Orion-KL, the bulk of the water emission is relatively compact and associated with the high-mass protostars and their outflows on scales of <25 000 au (<0.1 pc) (e.g., Goicoechea et al. 2015). For more distant high-mass sources at a few kpc, this emitting region would correspond to a single PACS spaxel. Indeed, HIFI maps of high-mass sources in the 988 GHz 2_{02}–1_{11} line show emission confined to $\lesssim$20″ (Jacq et al. 2016; van der Tak et al. 2019).

4.2. Cooling budget

Herschel-PACS full spectral scans from the WISH, WILL and DIGIT programs (see Fig. 7 for examples) have directly measured the total far-infrared line cooling, $L_{\rm FIRL}$ of the warm gas (Karska et al. 2014a, 2018; Green et al. 2016). For those sources for which only selected individual line scans have been observed, corrections for the missing lines have been made. For

the low-mass source sample consisting of 90 targets, $L_{\rm FIRL}$ does not change significantly with evolution from the Class 0 to the Class I stage: median values are 4.5×10^{-3} $L_\odot$ for Class 0 and 3.7×10^{-3} $L_\odot$ for Class I sources, respectively (Karska et al. 2018).

The relative contribution of individual coolants does change with evolution and between low- and high-mass sources. Figure 9 (left) summarizes the far-infrared line emission of CO, H_2O, OH and [O I] as a fraction of $L_{\rm FIRL}$. The LM Class 0 and I numbers are taken from Karska et al. (2018), and this sample is large enough that statistical uncertainties are small. The Class II values are from Karska et al. (2013) based on the sample from Podio et al. (2012). This sample is biased toward Class II sources with strong optical jets which may be more appropriate for comparison with the Class 0 and I outflows than disk-only sources. The Class II sample is too small to conclude whether differences between Class I and II are significant. The HM data are taken from Karska et al. (2014a) and for Orion Peak 1 from Goicoechea et al. (2015).

In the earliest stages of LM sources, CO and H_2O are the dominant coolants, with [O I] becoming relatively more important in the Class I and II stages. Interestingly, the fractional cooling of CO decreases by a factor of 2 whereas that of H_2O stays roughly constant from Class 0 to I. This conclusion differs from that of Nisini et al. (2002), who found a significant decrease in water cooling based on earlier ISO data. The absolute [O I] line cooling is similar from Class 0 to Class II, but its fraction increases as the jet changes from being mostly molecular to being primarily atomic (Nisini et al. 2015).

High-mass sources are found to have a smaller fraction of H_2O cooling compared with low-mass sources: their far-infrared line emission is dominated by CO. The main reason for this difference is that several H_2O and some OH lines are found in absorption rather than emission at the high-mass protostellar source positions, suppressing their contributions to the cooling. However, while globally the energy released in the water lines is low, the central emission is higher with the absorption transferring energy to the cooler layers. To assess the effect of this on-source absorption on the cooling budget, the Peak 1 outflow position in Orion has been added to the figure. This comparison demonstrates that the conclusion that CO dominates the cooling also holds off source where there is no absorption in the water lines.

Consistent with Nisini et al. (2002), the total far-infrared line cooling is found to strongly correlate with $L_{\rm bol}$, see Fig. 14 in Karska et al. (2014a) and Fig. 17 in Karska et al. (2018). The ratio of line cooling over dust emission, $L_{\rm FIRL}/L_{\rm bol}$, decreases from $\sim10^{-3}$ for low- and intermediate-mass sources to $\sim10^{-4}$ for high-mass sources. Nevertheless, this implies that total far-infrared line luminosity can be used as a direct measure of the mechanical luminosity deposited by the jet and wind into the protostellar surroundings. These data also provide estimates of the mass loss rates (Maret et al. 2009; Mottram et al. 2017; Karska et al. 2018).

4.3. Water emission: Two universal components

The water lines imaged by PACS reveal the location of warm water vapor emission, but are spectrally unresolved. In contrast, HIFI spectra reveal the full kinematic structure of the gas but are available mostly at a single position. Figure 2 illustrates that the observed water line profiles are universally broad toward all types of protostars, from low to high mass, and show dynamical

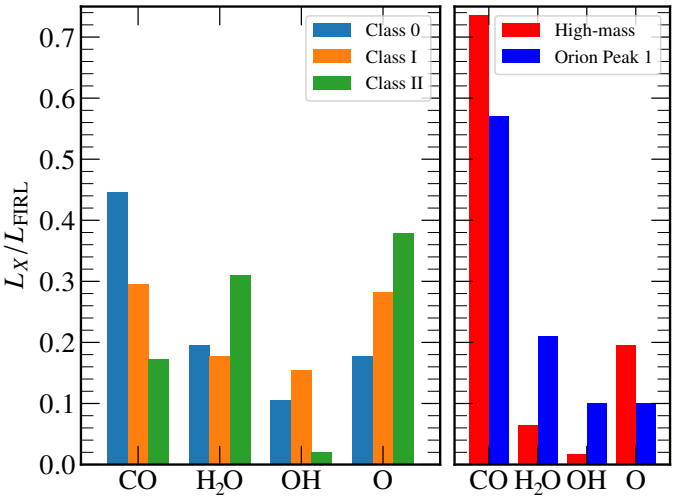

Fig. 9. Fractions of gas cooling contributed by far-infrared lines of CO, H_2O, OH and [O I] to the total far-infrared line cooling, as function of evolutionary stage for low-mass sources (*left*) and for high mass sources (*right*). The Class II sample is small and differences with Class I are not statistically significant. [O I] is seen to become relatively more important with evolution, whereas H_2O and OH contribute little for high-mass sources.

components not previously seen from the ground in low-J CO or other molecules (e.g., Kristensen et al. 2010, 2011, 2012, 2013; Johnstone et al. 2010; Herpin et al. 2012; van der Tak et al. 2013; Mottram et al. 2014; San José-García et al. 2016; Conrad & Fich 2020). They are complex, with emission out to ±100 km s^{-1}, and often have narrow absorption superposed on the ground-state lines at the source position. Nevertheless, comparing different water transitions, a maximum of only four different Gaussian components can be distinguished, each of them associated with a different physical component (Fig. 2, Table 1, see also Fig. C.2):

1. A broad component (typical $FWHM > 15$ km s^{-1}) centered at the source velocity and heated by kinetic energy dissipation. One scenario is that this water emission is produced in non-dissociative $C-$type shocks along the outflow cavity, called "cavity shocks" (Mottram et al. 2014). Alternative explanations for the observed line profiles and gas heating include MHD "disk winds" heated by ion-neutral drift (Yvart et al. 2016), and "turbulent mixing layers" forming between the protostellar wide-angle wind and infalling envelope (Liang et al. 2020).
2. A medium-broad offset component (typical $FWHM = 5$–15 km s^{-1}) slightly blue-shifted from the source velocity. Based on its velocity offset and distinct chemistry, this component is likely tracing dissociative $J-$type shocks, called "spot shocks", at the base of the outflow cavity.
3. A medium-broad component with similar FWHM as 2 but significantly offset from the source velocity, previously called Extremely High Velocity (EHV) gas or "bullets" (Bachiller et al. 1991). Although separately listed here, types 2 and 3 form a continuous sequence of velocity offset features in the profiles and are therefore all considered J-type spot shocks (Mottram et al. 2014).
4. A narrow component ($FWHM < 5$ km s^{-1}) at the source velocity, seen primarily in ground-state water lines in absorption and arising in quiescent cloud or envelope material. The absorption can also be part of a P Cygni type profile, consisting of strong emission lines with blue-shifted absorption pointing to an expanding shell of gas. Also,

Table 1. Physical components seen in water and high-J CO emission lines profiles.

Source type	Velocity Characteristics	$FWHM$ [(a)] (km s^{-1})	CO excitation (K)	Possible origin[(b)]
Pre-stellar	Narrow	<5	<10	Quiescent, infall
Low mass Class 0	Broad,	24	300	Warm outflow (cavity shocks, disk wind, turbulent mixing layers)
	Medium/offset	18	700	Hot spot shock
	Medium/EHV		700	Hot EHV bullets
	Narrow	3.5	<100	Quiescent, infall, expansion
Low mass Class I	Broad	15	300	Warm outflow (cavity shocks, disk wind, turbulent mixing layers)
	Narrow	2.6	<100	Quiescent, infall, expansion
Intermediate mass	Broad	32	300	Warm outflow (cavity shocks, disk wind, turbulent mixing layers)
	Narrow	4.6	<100	Quiescent, infall, expansion
High mass	Broad	24	300	Warm outflow (cavity shocks, disk wind, turbulent mixing layers)
	Narrow	5.6	<100	Quiescent, infall, expansion
Disks	Narrow	<4	20–300	Rotating disk

Notes. [(a)]Median width (FWHM) of water lines at the source position, taken from San José-García et al. (2016) and Table 5.4 of San José-García (2015). Values refer to the median of the WISH sample; those including other samples, such as the WILL sample, are similar within the uncertainties of a few km s^{-1}. [(b)]Based on Table 1 of Kristensen et al. (2017b).

inverse P Cygni profiles are seen with red-shifted absorption indicating infall.

Components 1–3 involve heating by dissipation of kinetic energy through one or more of the proposed mechanisms. In contrast, component 4 involves radiative heating, either by the bulk luminosity of the protostar heating the dust in the surrounding envelope which then transfers its heat to the gas through collisions (a 'passively' heated envelope), or by UV irradiation of the young star-disk system impinging on the gas and dust in outflow cavity walls or disk surfaces and heating it through the photoelectric effect.

Roughly 70–80% of the integrated H_2O emission comes from the broad part of the profile (component 1), whereas the medium-broad offset parts contribute 20–30% (components 2+3) for low-mass sources. For intermediate and high-mass sources, the quiescent component 4 contributes an increasingly higher fraction, up to 40% for the highest luminosity cases (San José-García et al. 2016).

The first two components are also seen in CO $J = 16$–15 ($E_{\rm up} = 752$ K, $n_{\rm crit} \approx 4 \times 10^6$ cm^{-3}) profiles observed with HIFI for low-mass protostars (Kristensen et al. 2017b). Extremely high velocity features are occasionally present as well in the 16–15 lines. The fact that they are not yet seen in the CO 10–9 profiles emphasizes the need for high spectral resolution observations at 1.5 THz and above. The broad and medium-broad velocity components can be associated physically with the two components universally seen in CO rotational diagrams of the same sources, as the $T_{\rm rot} \sim 300$ K (broad) and ~700 K (medium-broad) component, respectively (Table 1; see also below).

At the outflow positions, well offset from the LM and IM source positions by >1000 au, the water lines are also broad, with line widths of 10–40 km s^{-1} on either the blue or red side of the flow (Vasta et al. 2012; Tafalla et al. 2013). The wings at the outflow positions generally follow those seen at the source position in shape and extent although the level of agreement depends on whether a low or high excitation line is chosen for comparison (see below and examples in Bjerkeli et al. 2012; Santangelo et al. 2014b). Similar to the source position, the outflow positions show evidence for two physical components, at intermediate and high velocity offsets, which have different distributions and source sizes (Santangelo et al. 2014b). In addition, EHV gas is seen in a few cases, most notably at various positions in the L1448-MM outflow (Nisini et al. 2013) (see Fig. 2 for BHR71). The EHV component is actually more prominent in water lines than in the low-J CO lines in which it was originally detected (Bachiller et al. 1990, 1991).

4.3.1. Profiles across evolutionary stages

Figure 10 (left) compares the complexity and number of components seen in velocity-resolved water line profiles with evolutionary stage across low-mass sources, whereas Fig. 10 (right) does so for high-mass objects.

Water emission from quiescent starless or pre-stellar cores prior to star formation is very weak or not detected, both for low-mass (Caselli et al. 2010, 2012) and higher mass cores (Shipman et al. 2014). If any feature is seen, it is usually in absorption against the weak central continuum (Fig. 10).

As soon as the protostar is formed, complex water line profiles appear, especially in the earliest most deeply embedded stages. The complexity decreases with time: very few medium/offset components attributed to $J-$type spot shocks are seen in low-mass Class I sources. The FWHM and Full Width at Zero Intensity (FWZI) of the profiles also decrease from Class 0 to Class I, suggesting that the outflows become less powerful as the source evolves (Table 1). These results hold irrespective of source sample used to determine the mean or median width within each Class. Figure 10 (right) shows that within the high-mass stages from HMPO to UC HII, no significant differences in line widths are seen (San José-García et al. 2016; San José-García 2015).

For low-mass Class II sources without an envelope or molecular outflow, water emission is extremely weak and remains undetected for the bulk of the protoplanetary disks observed either with HIFI (Bergin et al. 2010a; Du et al. 2017) or PACS (Fedele et al. 2013; Dent et al. 2013; Rivière-Marichalar et al. 2015; Alonso-Martínez et al. 2017).

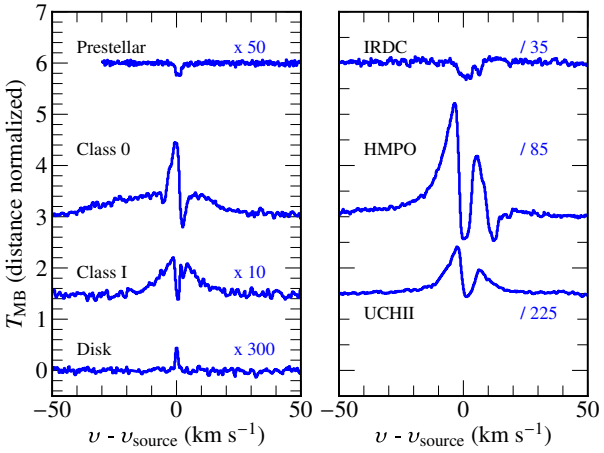

Fig. 10. Water $1_{10}-1_{01}$ 557 GHz spectra at various evolutionary stages, from pre-stellar cores to protostars and disks. *Left*: low-mass YSOs, showing from top to bottom the starless core Oph H-MM1, the Class 0 source Ser SMM4, the Class I source Elias 29 and the disk TW Hya. *Right*: high-mass YSOs, showing from top to bottom the starless core G11-NH_3, the HMPO DR21(OH), and the UC HII region NGC 7538 IRS1.

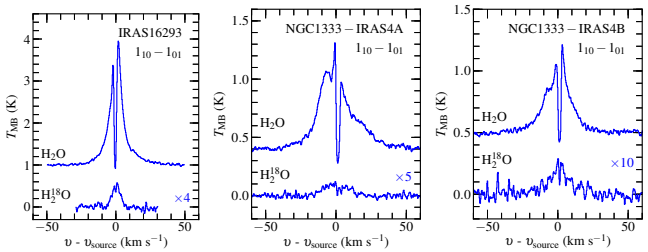

Fig. 11. Water $1_{10}-1_{01}$ 557 GHz and $H_2^{18}O$ 548 GHz lines for three low-mass sources. The $H_2^{18}O$ line for IRAS 16293-2422 is seen to be narrower compared with that of the NGC 1333 sources. Data from Coutens et al. (2012) and Mottram et al. (2014).

Overall, comparing the different evolutionary stages in Fig. 10, it is clear that water emission 'turns' on only when there is star formation activity in the cloud and it diminishes quickly once sources exit the embedded phase.

Water vapor emission is generally not detected from molecular clouds away from protostars. The only exception are Photon Dominated Regions (PDRs), that is, clouds exposed to enhanced UV radiation where water has been observed to have a single narrow emission line component. Examples are the Orion Bar PDR (Choi et al. 2014; Putaud et al. 2019), the Orion Molecular Ridge (Melnick et al. 2020) and the extended ρ Oph cloud (see Fig. 1 in Bjerkeli et al. 2012).

4.3.2. Profiles across mass range

Nearby intermediate mass sources show very similar features to those of low-mass Class 0 sources, with all four components present (Johnstone et al. 2010; van Kempen et al. 2016) (see NGC 2071 in Fig. 2). More distant intermediate mass sources and high-mass sources generally show only two components: the broad profile (component 1) and the quiescent envelope absorption and/or emission (component 4) (San José-García et al. 2016) (Fig. 10). Either these sources are more evolved, such as the low-mass Class I sources, or the $J-$type spot shocks are too beam diluted due to their larger distance to be detected.

The FWHM and FWZI of the water profiles change little from low- to high-mass protostars, suggesting a similar underlying launching mechanism of the jet. This point is illustrated by the average profiles for three water transitions for each of the types of sources presented in San José-García et al. (2016) (see Fig. C.2). Also, the maximum velocity υ_{max} reached by gas seen in CO is similar to that of water and independent of the CO line used, even though the line profiles change greatly from low- to high-J and their FWHM are generally smaller than that of water (Kristensen et al. 2017b; San José-García et al. 2016). At the outflow positions, υ_{max} is also similar among tracers such as H_2O, CO and SiO (Santangelo et al. 2012; Bjerkeli et al. 2012).

The narrow emission component originating in the quiescent envelope becomes more prominent for intermediate and high-mass sources due to their higher envelope mass, up to 40% of the emission seen in the low-lying $H_2^{16}O$ lines. This component is better probed through the excited lines of the less abundant isotopologs $H_2^{18}O$ and even $H_2^{17}O$: indeed, their line profiles show a narrow(er) emission component with $FWHM < 6\,km\,s^{-1}$ that lacks the broad outflow wings (Johnstone et al. 2010; Chavarría et al. 2010; Marseille et al. 2010; Choi et al. 2015; Herpin et al. 2016).

Interestingly, for high-mass sources, the $H_2^{18}O$ $1_{11}-0_{00}$ line profiles at 1101 GHz seen in absorption are remarkably similar to the difference between the H_2O $2_{02}-1_{11}$ 988 GHz and $2_{11}-2_{02}$ 752 GHz profiles, whose upper energy levels lie at 101 and 137 K respectively. This suggests that the narrow $H_2^{18}O$ absorption originates in the envelope just inside the 100 K radius where water sublimates from the grains; it does not arise in the cold envelope gas (see also Sects. 7 and 8) (Jacq et al. 2016; van der Tak et al. 2019).

These $H_2^{18}O$ features are not seen for low-mass sources: in spite of low noise levels, very few low mass sources show detections in the WISH and WILL samples, even in the ground-state lines (Mottram et al. 2014, 2017). Also, when detected (Fig. 11), the $H_2^{18}O$ lines are in emission and broad, in contrast with narrow excited ^{13}CO and $C^{18}O$ lines (Kristensen et al. 2010; Yıldız et al. 2013b). The spatially extended broad $H_2^{18}O$ outflow component may actually block any narrower emission line arising closer to the protostar if it is optically thick. One exception may be the molecule-rich low-mass protostar IRAS 16293-2422, part of the CHESS survey (Coutens et al. 2012), where both $H_2^{18}O$ and $H_2^{17}O$ lines have been detected with widths that are clearly narrower than those of H_2O (Fig. 11).

Is quiescent warm $H_2^{18}O$ emission completely absent in low-mass sources? A dedicated deep (up to 5 hr integration per line) open time program has revealed narrow features superposed on the broad outflow profile in the excited water $3_{12}-3_{03}$ lines near 1097 GHz for all three water isotopologs, but only in a few sources (Visser et al. 2013) (see Sect. 8 and Fig. C.3).

Taken together, the broad and medium/offset components of the water line profiles can be used to study its chemistry in warm outflowing and shocked gas, from low- to high-mass sources. For intermediate and high-mass sources, the narrow $H_2^{18}O$ emission profiles probe the water abundance in the quiescent envelope. For low-mass sources, only the narrow part of the $H_2^{16}O$ (inverse) P Cygni profiles can be used to determine the quiescent water abundance, since their $H_2^{18}O$ profiles are still broad and optically thick, hiding any narrow emission component. As will be shown in Sect. 7, these complex (inverse) P Cygni profiles are actually a remarkably powerful tool to determine the water abundance profile throughout the cold envelope and cloud.

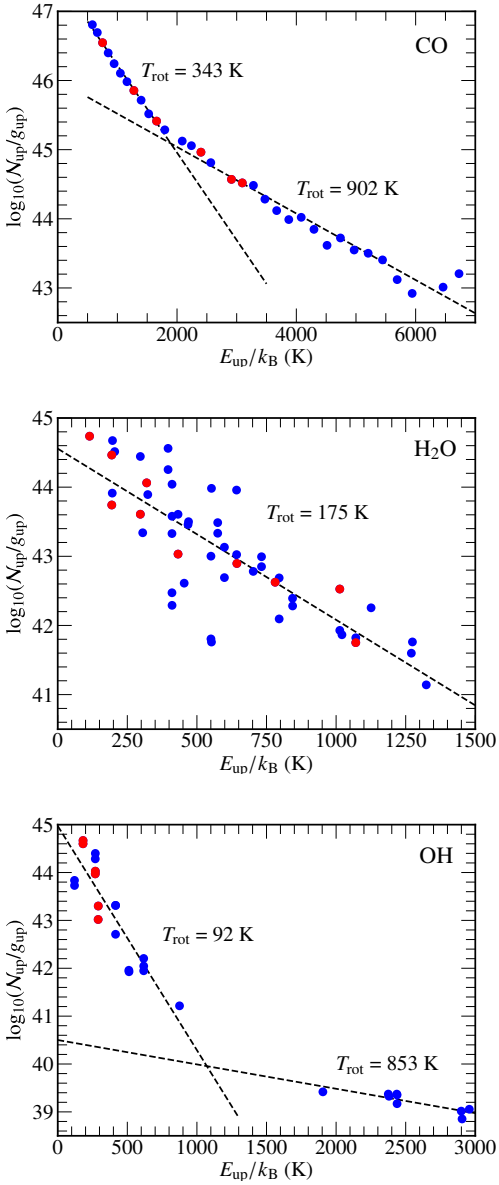

Fig. 12. Comparison of the rotational diagram of CO (*top*), H_2O (*middle*) and OH (*bottom*) for the low-mass YSO NGC 1333 IRAS 4B obtained from the full PACS spectral scan. The red points indicate those lines targeted in WISH and WILL for sources for which no full spectral scans have been obtained. The scatter in the water diagram is dominated by the difference in optical depth of the lines. Different energy ranges are covered for each of the species.

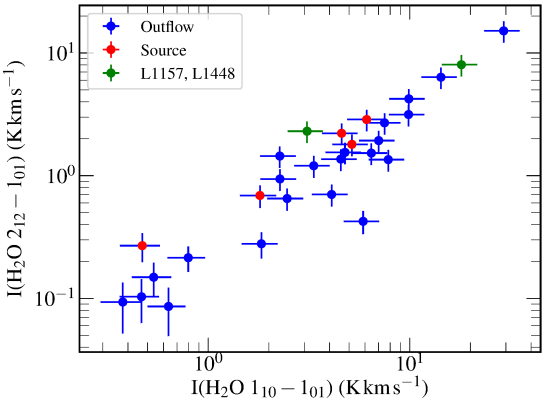

Fig. 13. Correlation of the water 1_{10}–1_{01} 557 GHz (HIFI) and 2_{12}–1_{01} 1670 GHz/179 μm (PACS) line intensities convolved to a common angular resolution toward various outflow and source positions. The outflow data points (blue) are from Tafalla et al. (2013), whereas the source positions (red) use data from Kristensen et al. (2012). This figure demonstrates similar line ratios and thus similar conditions at the on and off source positions. Also, the two sources with strong EHV components, L1157 and L1448-MM (green), do not stand out in this figure.

4.4. Water excitation

4.4.1. Comparing observed fluxes and line profiles

The integrated intensities and luminosities of the various water vapor lines obtained with HIFI and PACS are well correlated with each other at the central protostellar positions, both for low- and high-mass sources (e.g., Karska et al. 2014a; Mottram et al. 2014; San José-García et al. 2016). Rotational diagrams using mostly PACS lines (Fig. 12, middle) indicate median water excitation temperatures of ~140 K for low-mass sources (Herczeg et al. 2012; Goicoechea et al. 2012; Karska et al. 2018) increasing up to ~250 K for high-mass sources (Karska et al. 2014a), with some spread around the mean. The DIGIT survey finds an average value of ~190 K (Green et al. 2013). Because water is subthermally excited, these temperatures are lower limits to the kinetic temperature(s) of the emitting gas. Also, because of high but varying optical depths of the lines, these water excitation temperatures have a limited meaning.

Do these conclusions also hold at positions off source? For low-mass sources, water vapor maps have been made only in two of the ground state transitions (557 and 1670 GHz/179 μm). The flux ratio of these two lines is again very constant across the entire outflow (Tafalla et al. 2013). Moreover, as Fig. 13 shows, the protostellar positions do not stand out in this correlation, suggesting similar conditions on and off source.

This good correlation between water lines holds not only for integrated fluxes but even as a function of velocity. HIFI velocity-resolved observations of the different water transitions with E_{up} ranging from 50 to 250 K reveal surprisingly similar line profiles at the low-mass protostellar positions, irrespective of excitation and beam size (Mottram et al. 2014). The same is often true for the intermediate and high-mass protostars for those lines whose profiles are not affected by absorption (Herpin et al. 2016; San José-García et al. 2016) (Fig. C.2).

4.4.2. Comparison with CO excitation

Surveys of the CO rotational ladder for many protostars with PACS have shown that its excitation for $J_{up} > 14$ can be universally fitted by two rotational temperatures: $T_{rot} \sim 300$ K (warm) and ~700 K (hot) (Fig. 12 top, Fig. 14), respectively, with about 80% of the CO flux originating in the warm component and 20% in the hot component (e.g., Goicoechea et al. 2012; Karska et al. 2013, 2018; Green et al. 2013, 2016; Manoj et al. 2013; Lee et al. 2013; Dionatos & Güdel 2017; Yang et al. 2018). This constancy holds both across evolutionary stages as well as across mass or luminosity (Karska et al. 2014a, 2018; Matuszak et al. 2015). The temperature of the hot CO component shows a larger scatter between sources than the warm component but always has $T > 500$ K.

A key step forward in the interpretation of these two CO rotational temperature components was made by Kristensen et al. (2017b) through velocity resolved CO $J = 16$–15 profiles,

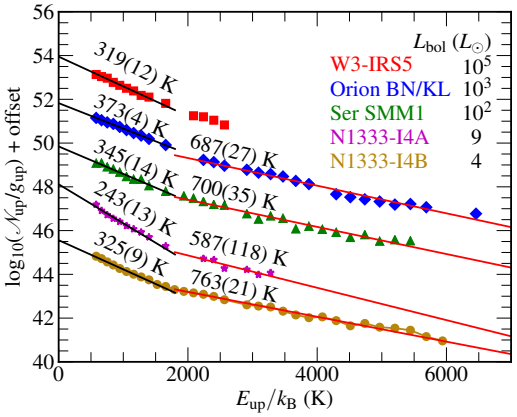

Fig. 14. CO excitation diagrams from low to high-mass protostars based on (velocity-unresolved) PACS data. Two excitation temperature components of T_{rot} ~300 and ~700 K are seen across the mass range. The Orion rotation diagram refers to Peak 1. Data from Herczeg et al. (2012); Karska et al. (2014a); Goicoechea et al. (2012, 2015).

a transition also covered by PACS. This CO line has very similar line profiles to those of water. The broad component was shown to correspond to the $T_{rot} \sim 300$ K component, and the medium-offset spot shocks to the ~700 K component.

Taken together, *Herschel* has shown that three ranges of CO lines can be identified (Goicoechea et al. 2012; Yıldız et al. 2013b; Karska et al. 2018): (i) low-J ($J_{up} < 14$) probing warm quiescent and entrained outflow gas; (ii) mid-J ($J_{up} = 14$–24) probing the 300 K broad component; and (iii) high-J ($J_{up} > 24$) probing the hot 700 K shock component.

4.4.3. CO and water excitation analysis: inferred physical conditions

On-source position. To infer the physical conditions of the gas from these observed rotational temperatures, non-LTE excitation calculations need to be performed using programs such as RADEX (van der Tak et al. 2007). Such analyses have been primarily carried out for LM and IM sources. For CO, it has been demonstrated that both components require high densities ($>10^6$ cm^{-3}), with kinetic temperatures T_k of ~300–400 and 700–1000 K, respectively (Goicoechea et al. 2012; Karska et al. 2018). In some sources with particularly bright CO lines extending to mid-infrared wavelengths, an even hotter component with $T_k \approx 2500$ K may be needed. A single hot (up to 4000 K) component at very subthermal excitation conditions, $T_{rot} \ll T_k$, can provide good solutions to the entire CO excitation ladder as well (Neufeld 2012), but this solution is not consistent with the multiple velocity components seen for high-J CO and H_2O line profiles (Kristensen et al. 2017b) and will therefore not be considered further here.

Do these same conditions also reproduce the water excitation? Analyses of the HIFI lines using RADEX for a single slab model demonstrate that water is indeed collisionally and sub-thermally excited. Best fits are obtained for densities in the range of 10^5–10^8 cm^{-3}, both for the broad component and the medium-broad or offset spot shocks. Kinetic temperature is not well constrained due to the limited range of energy levels covered with HIFI but is typically a few hundred K. Moreover, to fit the absolute fluxes, the size of the emitting area has to be small compared with the beam size, only of order ten to a few hundred au (Mottram et al. 2014).

PACS observed much higher excitation lines of water. An early analysis for the line-rich low-mass protostar NGC 1333 IRAS 4B (Figs. 7, 14) resulted in a single component fit with $T_k \approx 1500$ K, $n \approx 3\times10^6$ cm^{-3} and an emitting radius of ~100 au (<1″) centered in the blue outflow lobe located slightly off source (Herczeg et al. 2012). Thermal excitation at a much lower temperature of 170 K and very high densities $n > 10^{11}$ cm^{-3} on source, as suggested based on mid-infrared *Spitzer* observations (Watson et al. 2007), was excluded in this case. Similarly, modeling of the PACS spectral scan of the Serpens SMM1 intermediate mass source gave $T_k \approx 800$ K, $n \approx 5\times10^6$ cm^{-3} with an emitting region of radius ~500 au (Goicoechea et al. 2012). Comparable conditions are found for L1448-MM (Lee et al. 2013).

In summary, all detailed analyses for low- and intermediate-mass sources agree that the on-source CO and H_2O emission originates from high density $n > 10^6$ cm^{-3}, warm ($T_k \gtrsim 300$ K up to 1000 K) gas with a small emitting area. There is little evidence for a very hot component of several thousand K based on far-infrared data. For the more distant high-mass sources, the analysis is complicated by the fact that shock and envelope emission are more intermixed. However, if the RADEX analysis is limited to the water wing emission, the conditions are inferred to be similar, albeit with somewhat larger emitting areas up to 5000 au (see Sect. 3.6 in San José-García et al. 2016).

Outflow positions. In contrast with the protostellar positions, the velocity-resolved profiles of water lines at outflow spots in low-mass sources can be markedly different from each other. Low excitation lines often show excess emission at high velocity compared to the higher excitation lines. This can be interpreted in terms of density variations, with the gas at low velocity being denser than that at high velocity (Santangelo et al. 2012; Vasta et al. 2012). Indeed, when the water line intensities are consistently fitted together with spectrally resolved high-J CO and mid-IR H_2 observations, the physical conditions of the two water components are as follows (Santangelo et al. 2014b): a warm component at $T_k \sim 300$–1000 K, $n \approx 10^6$–10^8 cm^{-3}, and size 10 – 15″; and a hot component at $T_k > 1000$ K, $n \approx 10^4$–10^5 cm^{-3}, and size 1–5″, for sources at ~200 pc (see also Busquet et al. 2014).

These numbers are consistent with the analysis of the water excitation based on the 557/1670 GHz line ratio at the outflow positions (Fig. 13), which gives pressures $nT \approx 4\times10^9$ cm^{-3} K (Tafalla et al. 2013). Such pressures are about 4 orders of magnitude higher than the surrounding quiescent gas. For $T_k <$ 4000 K, which is the temperature above which molecules are collisionally dissociated, this implies $n > 10^6$ cm^{-3}, consistent with the warm component. The association with H_2 mid-infrared emission gives $T_k > 300$ K as a lower limit.

Thus, while the physical parameters at the outflow positions are similar to those inferred at the protostellar positions (warm and dense), the emitting areas are much larger off source, with sizes up to a few thousand au for the warm component. Also, temperatures can be higher in the offset hot component. This compact hot component is suggested to be associated with the jet impacting the surrounding material in a bow shock, whereas the extended warm and dense component originates from the weaker shocks further downstream. Since shocks at off-source positions can expand in more directions than close to the protostellar base, the larger emitting area and somewhat lower densities found at the outflow positions are not in contradiction.

4.5. Water as tracer of envelope infall and expansion

The absorption and narrow emission features probe the quiescent envelope material. Their line profiles are asymmetric in a fraction of sources (see, for example, Figs. 2 and 10), and indicate either infall motions (inverse P Cygni) or expansion (regular P Cygni) on envelope scales (few thousand au). The incidence of infall profiles is higher in low-mass Class 0 than Class I sources (Kristensen et al. 2012; Mottram et al. 2017). Still, the majority of the Class 0 sources surprisingly do not show infall motions in any molecular feature (Mottram et al. 2017). The incidence of expansion is similar for Class 0 and I. Taken together, the WISH + WILL samples show infall in 7 + 6 = 13 sources and expansion in 6 + 2 = 8 sources, out of a total of 29 + 49 = 78 sources. The small sample of intermediate mass sources shows primarily P Cygni profiles indicative of expansion.

The majority of the high-mass sources, about 2/3, show infall whereas the remainder show expansion (Herpin et al. 2016; van der Tak et al. 2019). Infall is seen not just in the outer cold envelope gas but also in warm dense gas close to the protostar through $H_2^{18}O$ absorption (Jacq et al. 2016; van der Tak et al. 2019). High mass sources often have many more narrow absorption lines offset from the source velocity due to low density diffuse clouds along the line of sight, some of which may be close by and infalling onto the high-mass core (Marseille et al. 2010; van der Wiel et al. 2010; Gerin et al. 2016).

Quantitative modeling of the (outflow subtracted) water line profiles provides mass infall rates from cloud to envelope of order 10^{-5}–10^{-4} $M_\odot$ yr^{-1} for low-mass protostars (Mottram et al. 2013), to 10^{-4}–10^{-2} $M_\odot$ yr^{-1} for high-mass protostars (van der Tak et al. 2019). The latter values are comparable to those derived from inverse P Cygni profiles observed in NH_3, either with HIFI or with the Stratospheric Observatory for Infrared Astronomy (SOFIA) (Wyrowski et al. 2016; Hajigholi et al. 2016).

4.6. Summary of physical components

Table 1 summarizes the profile characteristics and their proposed origin. The key point is that the bulk of the broad water and high-J CO (J_{up} > 14) emission go together and arise in two physical components associated with outflows and shocks, seen as T_{rot} = 300 and 700 K in the CO data and as the broad and medium-broad offset components. The implied physical conditions for both components are high densities ($n > 10^5$–10^8 cm^{-3}) and with warm ($T_k \approx 400$ K) and hot ($T_k \approx 1000$ K) temperatures, respectively. Emitting sizes are small, only ~100 au for low-mass sources up to 5000 au for distant high-mass sources.

The narrow emission and absorption lines probe the more quiescent envelope gas. Overall, the infall and expansion signatures highlight water's ability to pick up small motions along the line of sight on envelope scales. This will prove to be extremely useful to constrain the physical structure and abundance profiles of water and related molecules in the cold outer parts of envelopes (Sect. 7). Water is in this aspect more effective than well-known envelope tracers such as low-J $C^{18}O$ or HCO^+.

4.7. Ortho/para ratio

The ortho/para ratio of water, or equivalently its "spin" temperature, is in principle also a diagnostic of its physical and chemical history. At low temperatures (<10 K) the ortho/para ratio tends to 0 whereas at T > 50 K, the equilibrium ortho/para ratio would be 3. Thus, low ortho/para ratios have been invoked to trace a low formation temperature of H_2O on cold grain surfaces (Mumma & Charnley 2011). However, the ortho/para ratio is controlled by a complex combination of processes (e.g., Tielens 2013; van Dishoeck et al. 2013), including possible changes in the ortho/para ratio upon ice desorption (Hama et al. 2018), and will not be summarized here. Overall, water spin temperatures may tell astronomers less about the water formation location than previously thought.

Within the WISH project, the data are consistent with an ortho/para of 3 for warm water (e.g., Herczeg et al. 2012; Mottram et al. 2014; Herpin et al. 2016). There have been some claims of ortho/para ratios lower than 3 in other sources (e.g., Hogerheijde et al. 2011; Choi et al. 2014; Dionatos et al. 2018) but differences in optical depth of the ortho and para lines can also mimic such low ratios if not properly accounted for (Salinas et al. 2016). In fact, a more detailed analysis of many water lines observed with HIFI in the Orion Bar shows values close to 3 (Putaud et al. 2019).

In summary, there is no convincing evidence for water ortho-to-para ratios significantly below the LTE value of 3 to be present in the ISM.

5. Shocks

Assuming that the bulk of the water emission observed by *Herschel* originates from high temperature shocked gas, WISH+ allows tests of chemical models of different shock types. Key questions to address are (i) whether the basic prediction that all volatile oxygen not locked up in CO is driven into water at high temperatures holds, in which case values of $H_2O/H_2 \approx 4 \times 10^{-4}$ and $H_2O/CO \approx (1.4–2)$ are expected (Sect. 3.1), (ii) what the relative contributions of ice sputtering and gas-phase (re)formation are to the total gaseous water abundance.

5.1. Inferred water abundances in shocks

5.1.1. On-source positions

Table 2 summarizes measurements of the water abundance in warm outflowing and shocked gas made by *Herschel*. A list of pre-*Herschel* results, mostly using *SWAS* or ISO, can be found in Table 4 of van Dishoeck et al. (2013). *Herschel* has advanced the field in several ways. First, thanks to HIFI, the different velocity components (see Sect. 4.3) can now be quantified separately. Although the precise origin of the broad component is still under discussion (see Table 1), this does not matter for the observational derivation of abundances, and this component will therefore be denoted in this section as shock. A second key advantage is the simultaneous measurement of (spectrally-resolved) high–J CO originating in the same gas. Moreover, *Spitzer* observations of the mid-IR H_2 lines are available for several off-source shock positions providing a direct measure of the warm H_2 (S(1)-S(5), few hundred K) or hot H_2 (S(5)-S(9), >1000 K) column densities. At the source position such data are alas not available since the mid-IR lines are too extincted (Maret et al. 2009). The availability of high-J CO or H_2 data removes one of the largest uncertainty in the $X(H_2O) = N(H_2O)/N(H_2)$ abundance determinations, namely the H_2 column (the denominator). Early measurements often used the line wings of low–J CO lines to estimate the H_2 column, which *Herschel* has now shown not to be appropriate (Sect. 4). Hence, any literature values using low-J CO as reference are not included in Table 2.

The most reliable determination of the water abundance as a function of velocity comes from the detailed study of 24 low-mass protostars by Kristensen et al. (2017b) using HIFI

Table 2. Summary of H_2O/H_2 abundance determinations using *Herschel* data in warm outflows and shocks.

Source	Type	Instrument	H_2O/H_2 (10^{-4})	H_2 from	Reference
On source					
Several	LM	HIFI	0.02 (LV+HV)	CO 16–15 [(a)]	Kristensen et al. (2017b)
AFGL 2591	HM	HIFI	0.001	CO 16–15	Kristensen (priv. comm.)
NGC 1333 IRAS 4B	LM	PACS	1.0	High-J CO	Herczeg et al. (2012)
Serpens SMM1	LM/IM	PACS	0.4 (hot)	High-J CO	Goicoechea et al. (2012)
NGC 7129 IRS	IM	HIFI/PACS	0.2–0.3	High-J CO	Johnstone et al. (2010) Fich et al. (2010)
NGC 6334I	HM	HIFI	0.4	Mid-J CO	Emprechtinger et al. (2010)
DR21(OH)	HM	HIFI	0.32 [(b)]	High-J ^{13}CO	van der Tak et al. (2010)
Outflow					
L1157 B1	LM	HIFI	0.008(LV) 0.8(HV)	Mid-J CO	Lefloch et al. (2010)
L1157 B2/R	LM-OF	HIFI/PACS	0.01	Warm H_2	Vasta et al. (2012)
L1448 B2	LM-OF	HIFI/PACS	0.03 (warm) 0.03–0.1 (hot)	Warm H_2 Hot H_2	Santangelo et al. (2012, 2013)
L1448	LM	HIFI/PACS	0.005–0.01	Warm H_2	Nisini et al. (2013)
VLA1623	LM-OF	HIFI	<0.01 [(c)]	Warm H_2	Bjerkeli et al. (2012)
Several B/R	LM/IM-OF	HIFI/PACS	0.003	Warm H_2	Tafalla et al. (2013)
HH 54	OF	HIFI	<0.14 (B)	Warm H_2	Santangelo et al. (2014a)
L1157 B1	LM-OF	HIFI/PACS HIFI/PACS	0.007–0.02 (warm) 1–3 (hot)	Warm H_2 Hot H_2	Busquet et al. (2014)
NGC 1333 I4A R2	LM-OF	HIFI/PACS	0.007-0.01 (warm) 0.3–0.7 (hot)	CO 16–15 [(a)]	Santangelo et al. (2014b)
NGC 2071 B/R	IM-OF	PACS	0.3–0.8	Warm H_2+high$-J$ CO	Neufeld et al. (2014)
Orion-KL	HM-OF	PACS	≤0.01 (warm,hot) >2 (very hot)	High-J CO [(a)] very high-J CO	Goicoechea et al. (2015)

Notes. Uncertainties claimed by the authors range are typically a factor of 2 to a few. HV = high-velocity; LV = low; B = Broad component velocity. In most cases, the abundance refers to the outflow at the central source position. B and R indicated blue- and red-shifted outflow spots (OF) offset from the source. [(a)]Assuming $CO/H_2 \approx 10^{-4}$; if $CO/H_2 = 2\times10^{-4}$ advocated in Sect. 3.1 is used, the water abundances are increased by a factor of two. [(b)]From para-H_2O assuming ortho/para = 3. [(c)]Ortho-H_2O abundance.

CO 16–15 spectra as the reference. A remarkably constant H_2O/CO abundance ratio of 0.02 is found, independent of velocity. This constant abundance ratio even holds for the EHV "bullet" component such as seen in L1448-MM. Assuming $CO/H_2 = 10^{-4}$, both the warm broad and hot spot shock components are found to have surprisingly low water abundances, with $H_2O/H_2 = 2\times10^{-6}$. Only very hot gas may have a higher water abundance (Franklin et al. 2008): using the H_2O and CO PACS lines in line-rich low-mass sources, H_2O abundances up to $\sim10^{-4}$ have been found for the hottest gas (Goicoechea et al. 2012).

For high-mass protostars, few observations of CO 16–15 are available as reference. For the case of AFGL 2591, the observed line intensity ratio of H_2O 557 GHz / CO 16–15 is ~0.1 in the outflow wing. This translates to an abundance ratio $H_2O/CO \sim 10^{-3}$ when taking beam dilution into account and following the same analysis as for the low-mass sources (Kristensen, priv. comm.). An early analysis of the DR 21 shock using ^{13}CO 10–9 as reference found an abundance ratio $H_2O/CO \sim 7\times10^{-3}$ in the shock. Thus, the H_2O abundance in high-mass outflows may be even lower than that inferred for low-mass protostars, although not as low as found by Choi et al. (2015). Indeed, van der Tak et al. (2019) conclude based on $H_2^{18}O$ absorption in line wings toward high-mass protostars that water abundances in outflows are an order of magnitude higher than in the cold envelopes, where values of 10^{-9}–10^{-8} have been found (Boonman et al. 2003a, and Sects. 7 and 8). Taken together, the H_2O/H_2 abundances for high mass outflows are found to be 10^{-7}–10^{-6}.

5.1.2. Outflow positions

At the outflow positions, where direct measurements of the warm H_2 columns are available, the largest uncertainty stems from the uncertainty in the physical parameters used to determine the H_2O column densities, since the same data can be fitted with different water column densities and filling factors. Nevertheless, if the H_2O, high-J CO and H_2 data are fitted simultaneously, the abundance of the warm H_2O component is better constrained. The derived abundance is universally found to be low, ranging between 10^{-7}–10^{-6} (Santangelo et al. 2012, 2013, 2014a; Bjerkeli et al. 2012; Nisini et al. 2013; Tafalla et al. 2013; Busquet et al. 2014). There are suggestions that the abundance in the hot component (>1000 K) component is higher, $>5\times10^{-6}$, but this is more difficult to constrain with the available data (Santangelo et al. 2013, 2014b). Abundances close to 10^{-4} have been found only for the very hot gas seen in the highest-J H_2O and CO lines but the lack of H_2O lines originating from very high energy levels (>1000 K) in the *Herschel* data make it more difficult to constrain this component (Lefloch et al. 2010; Busquet et al. 2014; Neufeld et al. 2014; Goicoechea et al. 2015).

Melnick et al. (2008) combined mid-infrared observations of pure rotational H_2O and H_2 lines to infer water abundances H_2O/H_2 in the range $(0.2–6)\times10^{-4}$ for shock positions in the intermediate mass source NGC 2071 offset from the source position. These mid-infrared data probe higher excitation H_2O levels than the *Herschel* data and are thus better suited to test the water predictions for >1000 K gas. The uncertainty in the inferred water abundances reflects the uncertainty in the gas density in the shock. Leurini et al. (2014) derived a fractional column density ratio $H_2O/H_2 \approx (1.2–2.5)\times10^{-5}$ for the IRAS 17233-3606 outflow by modeling consistently both *Herschel* H_2O and H_2 2 μm infrared data, finding a maximum fractional water abundance in the shock layer of 10^{-4}.

Independent evidence that H_2O does not contain all of the oxygen comes from mid-infrared absorption line observations with ISO and SOFIA of hot water and CO along the lines of sight to massive protostars, many of them the same sources as included in the WISH sample (van Dishoeck & Helmich 1996; Boonman & van Dishoeck 2003). In particular, high spectral resolution absorption line observations at 6 μm using SOFIA-EXES give $N(H_2O)/N(CO) \approx 0.7$ for gas at ~1000 K, a factor of 2–3 less than expected if all oxygen is in water (Indriolo et al. 2015a).

In conclusion, the water abundances observed by *Herschel* are two–three orders of magnitude lower than predicted by standard high temperature (shock) models that drive all volatile oxygen into water. This conclusion holds in both velocity components on-source, and at off-source positions as well. Water abundances as high as $\sim10^{-4}$ are perhaps only attained in the very hot (>1000 K) gas that is not well probed by *Herschel*. Even then, there is no firm observational evidence yet for any shock associated with outflows in which H_2O/H_2 is as high as 4×10^{-4}, the value expected if all volatile oxygen is in H_2O. See Sect. 10 and Appendix G for further discussion.

5.2. H_2O vs. OH

A key intermediate species in the O → H_2O reaction is OH, so given the fact that the H_2O abundance is found to be low, does this imply that the OH abundance is high? WISH targeted a number of OH transitions with PACS, particularly the low-lying transitions at 119, 84 and 163 μm (Fig. 3), and covered low-, intermediate-, and high-mass sources. The PACS instrument did not resolve the hyperfine components of the OH transitions (the splitting is typically <5 km s^{-1}), but it did resolve the Λ doubling. Strong indications for an enhanced OH abundance come from the observed OH/H_2O flux ratio in a large number of low-mass protostars, which is found to be much higher than expected based on models of shocks propagating into dark molecular clouds (Karska et al. 2014b, 2018). Strong OH emission is also detected with PACS for high-mass protostars (Karska et al. 2014a).

Apart from these velocity-unresolved PACS observations, the 1834 and 1837 GHz OH triplets, which make up the 163 μm lines, were observed with HIFI and detected toward W3 IRS5 and Ser SMM1 (Wampfler et al. 2011; Kristensen et al. 2013). The 1837 GHz triplet is completely resolved toward W3 IRS5 and consists of narrow (~5 km s^{-1}) hyperfine components superposed on top of a broad (~20 km s^{-1}) outflow component. Toward Ser SMM1, the 1834 GHz transition consists of a single broad component, which appears blue-shifted (~10 km s^{-1}) (Fig. 15). The hyperfine splitting is actually smaller for this triplet than for the 1837 triplet. The 1837 GHz line was also observed toward a number of other low-mass sources within WISH but not detected. Comparing their limits with the PACS 163 μm detections implies that the lines for these sources must also be broad (FWHM at least 10–15 km s^{-1}) (Wampfler et al. 2010).

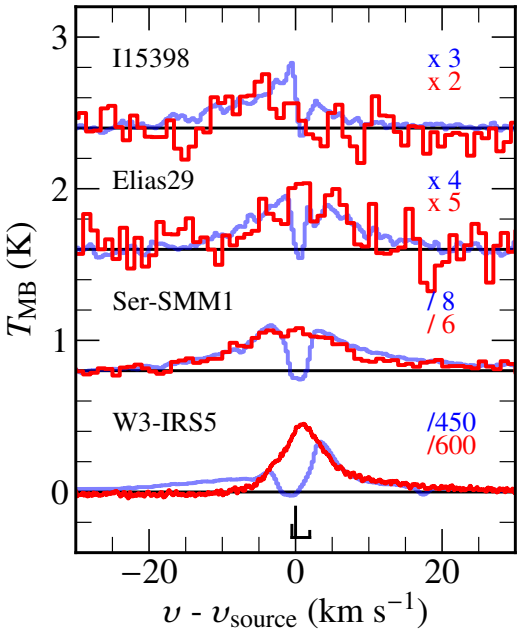

Fig. 15. Comparison of HIFI spectra of the H_2O $1_{10}–1_{01}$ 557 GHz line (blue) and the OH 1834 GHz triplet (red) toward a number of low and high-mass regions. The splitting of the three OH lines in the triplet and their relative strength are indicated at the bottom of the figure. Data from Kristensen & Wampfler (priv. comm.).

As part of WISH+, the COPS-HIFI program observed the 1834 GHz triplet together with CO 16–15 for 24 sources (Kristensen et al. 2017b; Kristensen & Wampfler, priv. comm.) (Fig. 15). Where detected, the OH line is broad and follows H_2O. The OH abundance with respect to H_2O in the broad outflow component has been constrained to >0.03 (Wampfler et al. 2011; Kristensen & Wampfler, priv. comm.). For comparison, OH/H_2O abundance ratios >1 have been found in classical PDRs such as the Orion Bar where UV photodissociation controls the chemistry (Goicoechea et al. 2011).

The OH line luminosity increases from Class 0 to Class I low-mass protostars when compared to the total FIR luminosity (Wampfler et al. 2013; Karska et al. 2018) (Fig. 9). To first order, this suggests that the OH abundance increases with evolutionary stage. As the sources evolve, the UV radiation from the accreting protostar is able to penetrate deeper into the outflow, adding to photodissociation of H_2O and thus increasing the abundance of OH. However, in no case has OH been found to lock up a significant fraction of the oxygen, perhaps implying that gas temperatures remain below the activation threshold of the critical reactions (see also Sect. 5.4.2, Fig. 16).

5.3. Hydrides: Evidence for UV-irradiated outflow cavity walls

The cold outer protostellar envelopes are punctured by outflow cavities on scales of a few thousand au. Besides shocks stirring up the gas, UV radiation can escape through the cavities and impinge on the walls thereby heating them up (Spaans et al. 1995). Thus, outflow cavity walls are a source of bright far-infrared line radiation and simple hydrides such as CH^+, OH^+ and H_2O^+ turn out to be a good probe of them. These hydrides are readily detected in the WISH data for many sources, often

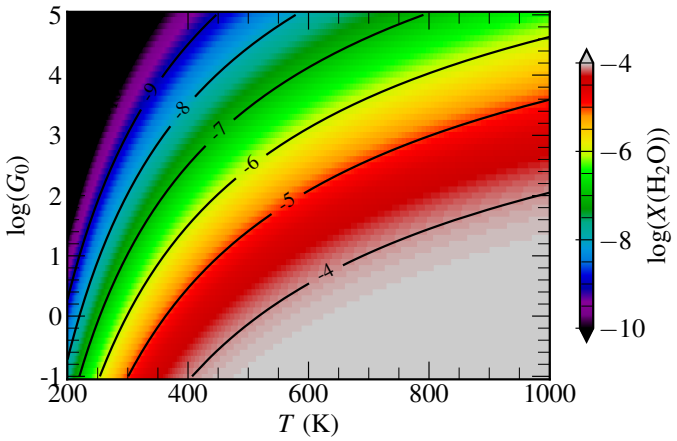

Fig. 16. Water abundance with respect to H_2 as function of temperature and UV radiation field using a simplified high-temperature chemistry model. The assumed density is 10^6 cm^{-3}; for higher or lower densities the abundance curves shift up or down, respectively, but the trend is the same. Based on Kristensen et al. (2017b).

in absorption, with their velocity offsets pointing to a spot shock or a more quiescent cavity wall origin. The results of the WISH hydride subprogram are summarized in Benz et al. (2016) with the analysis building on detailed modeling of the effects of UV and X-rays on protostellar envelopes by Stäuber et al. (2005) and Bruderer et al. (2009, 2010).

In brief, the observed hydride fluxes and flux ratios (e.g., CH^+/OH^+) can be reproduced by 2D models of UV illuminated outflow cavity walls on scales of the *Herschel* beam. The implied UV fluxes are up to a few $\times 10^2$ times the interstellar radiation field, at distances of ~2000 au and ~0.1 pc from low- and high-mass sources, respectively. If the FUV flux required for low-mass objects originates at the central protostar, a substantial FUV luminosity, up to 1.5 $L_\odot$, is required. Alternatively, some of the UV can be produced by the high-velocity shocks themselves. For high-mass regions, the FUV flux required to produce the observed molecular ratios is smaller than the unattenuated flux expected from the central object(s) at that radius, implying some extinction in the outflow cavity or, alternatively, bloating of the protostar (Hosokawa et al. 2010). Another important conclusion is that there is no molecular evidence for X-ray induced chemistry in low-mass objects on the observed scales of a few $\times$1000 au, even though X-rays may be important in destroying water on smaller scales (see Sect. 8).

5.4. Implications of low water abundances in shocks

5.4.1. Previous model predictions

Early shock models under dark cloud conditions find complete conversion of all volatile oxygen into water for any shock that has temperatures greater than ~250–400 K. Above this temperature, the O + H_2 and OH + H_2 reactions drive rapid water formation (Draine et al. 1983; Kaufman & Neufeld 1996; Flower & Pineau des Forêts 2010) (Fig. 4). The detection of high water abundances in the Orion shock by ISO was cited as a confirmation of this prediction (Harwit et al. 1998). For a non-dissociative shock, the temperature just behind the shock is typically $T_s = 375 b_M^{-0.36} [v_s/10 \text{ km s}^{-1}]^{1.35}$ K with the magnetic field strength $b_M = B/(n_H/\text{cm}^{-3})^{1/2}$ μG usually taken to be standard $b_M = 1$ (Neufeld et al. 2006). This then implies shock velocities $v_s = 10$–15 km s^{-1} to obtain the temperatures of a few hundred K required to drive the reactions.

If instead most oxygen is locked up in water ice in the pre-shocked gas, higher shock velocities are needed to sputter water ice, typically $\gtrsim$15 km s^{-1}. Such shocks have peak temperatures of $T_s \approx 650$ K (Draine et al. 1983; Jiménez-Serra et al. 2008; Gusdorf et al. 2011). Standard theoretical models for non-dissociative shocks predict the complete vaporization of ice mantles resulting in $H_2O/CO \sim (1.4$–$2)$ (Sect. 3.1). Even if the ice comes off as atomic O or OH, it should be quickly converted to H_2O at these temperatures and densities, if shielded from dissociating radiation.

In dissociative *J*-type shocks much higher temperatures $>10^4$ K can be reached at shock velocities $\gtrsim$25 km s^{-1} (McKee & Hollenbach 1980), which are sufficiently high to collisionally dissociate H_2 and H_2O. These molecules, together with CO, subsequently reform downstream in the cooling shock gas resulting in similar abundances.

In conclusion, the low water abundances and low H_2O/OH intensity ratios found by WISH+ are clearly in conflict with the standard shock model predictions.

5.4.2. UV-irradiated shocks

The above findings have led to the development of a new class of UV irradiated shock models (Melnick & Kaufman 2015; Godard et al. 2019). In such models, the H_2O abundance is lowered by photodissociation into OH and O. The UV radiation can either come from the shock itself, if fast enough (Neufeld & Dalgarno 1989), or it can be external, for example from the disk-star accretion boundary layer (Spaans et al. 1995).

Lowering the water abundance in the shocked gas by photodissociation is the simplest effect of UV radiation. If the pre-shocked gas is also UV irradiated and some of its H_2 dissociated, the entire shock structure changes: the UV photons increase the atomic and ionization fraction in the pre-shocked gas, resulting in a shock layer that is more compressed (smaller) and hotter for a given shock velocity and density. The UV radiation can also unlock more oxygen from water ice in the pre-shocked gas and thus increase the amount of atomic oxygen that can be converted into water.

Results from a limited set of irradiated shock models for UV fields of $G_0 = 0.1$–10 times the standard interstellar radiation field and pre-shock densities of 10^4–10^6 cm^{-3} indeed show much better agreement with *Herschel* data than the older models when $G_0 > 1$ (Karska et al. 2018). Such UV fluxes are plausible. In particular, enhanced UV fields with $G_0 = 10^2$–10^3 close to the protostar on scales of ~1000 au illuminating the outflow cavity walls have been independently inferred from bright narrow extended mid-*J* ^{13}CO emission lines (Spaans et al. 1995; Yıldız et al. 2012, 2015; Visser et al. 2012; Lee et al. 2013). Moreover, as noted above (Sect. 5.3), the presence of several hydrides such as CH^+ and OH^+ for both low- and high-mass protostars obtained as part of WISH points to UV-irradiated outflow walls with similar G_0 values (Bruderer et al. 2009, 2010; Benz et al. 2010, 2016).

Figure 16 illustrates the results of a simple chemical model balancing the high temperature formation of water through the reactions of O and OH with H_2 with photodissociation of H_2O, where the UV radiation field is given by its enhancement G_0 with respect to the standard interstellar radiation field (see Kristensen et al. 2017b, for details). For G_0 values of 10^2–10^3, the expected water abundance is indeed in the 10^{-7}–10^{-6} range at temperatures of several hundred K. Temperatures >1000 K are needed

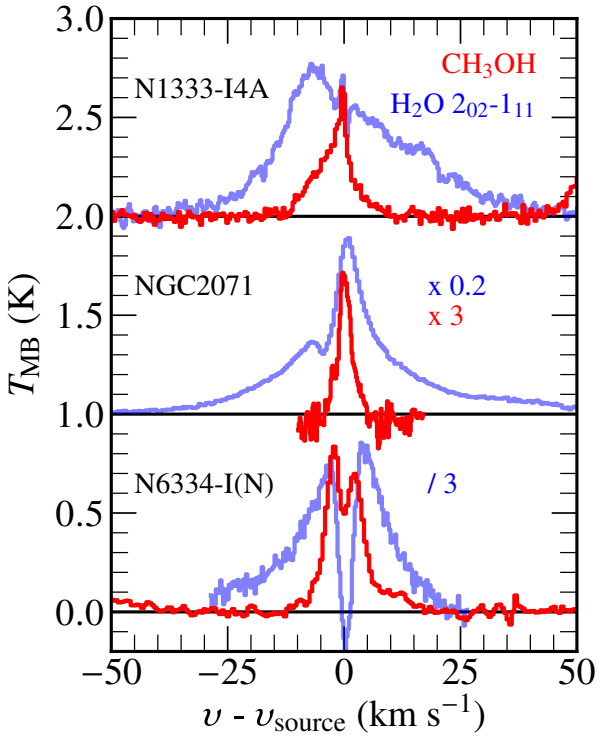

Fig. 17. Comparison of the H_2O $2_{02}-1_{11}$ 988 GHz line with that of an ice species, CH_3OH, for a low, intermediate and high-mass source. In all cases the CH_3OH line is seen to be much narrower than that of H_2O. For NGC 1333 IRAS 4A, the 7_0-6_0 line ($E_{up}=78$ K) at 338.4 GHz observed with the JCMT (15″ beam) is shown; for NGC 2071 the 6_2-5_1 line ($E_{up}=86$ K) at 766.7 GHz observed with HIFI is included (van Kempen et al. 2014) and for NGC 6334-I(N) the 5_1-4_0 line ($E_{up}=56$ K) at 538.5 GHz observed with HIFI is presented.

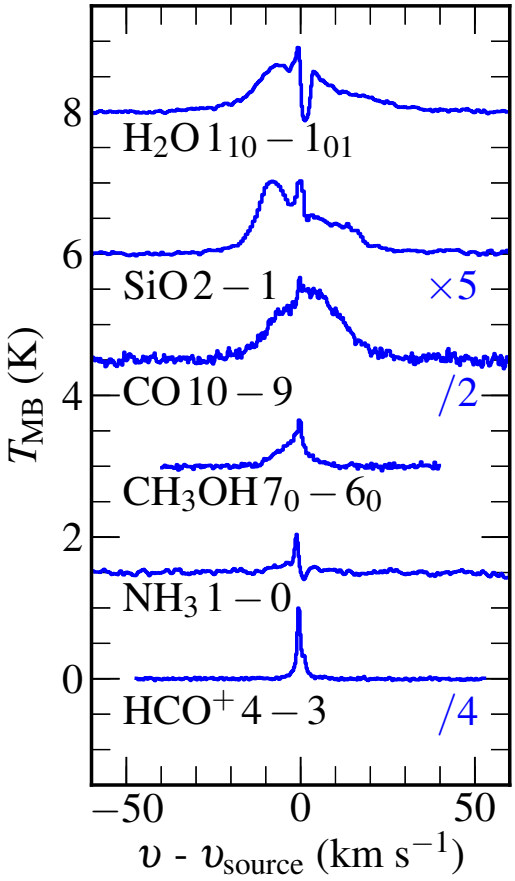

Fig. 18. Comparison of the line profile of water with those of other chemically or physically related molecules for the low-mass protostar NGC 1333 IRAS 4A. SiO and CO 10–9 trace shock and outflow; NH_3 and CH_3OH are both ice mantle products, similar to H_2O. The fact that their profiles are narrower suggests that H_2O is not just sputtered from ices but also produced by high temperature chemistry in the gas. The anticorrelation of the HCO^+ abundance with that of water is illustrated by its lack of broad line profiles.

to drive the bulk of the oxygen into water and reach water abundances as high as 10^{-4} if UV radiation is present.

5.5. High T chemistry vs. sputtering: SiO, CH_3OH, NH_3

To what extent is the water seen in shocks produced by high temperature gas-phase chemistry, as assumed in Fig. 16, versus ice sputtering? Shocks with velocities of 15 km s^{-1} needed for water ice sputtering are observed for most embedded sources, except perhaps for the low-mass Class I objects. To better distinguish the two mechanisms and isolate the contribution due to sputtering, it is useful to compare the H_2O line profiles with those of other abundant ice mantle constituents, most notably CH_3OH and NH_3.

Figure 17 compares H_2O and CH_3OH line profiles for a low, intermediate and high mass protostar, observed with *Herschel*-HIFI or from the ground in a similar beam (Suutarinen et al. 2014; van Kempen et al. 2014; Herpin et al. 2016). The H_2O profiles clearly extend to much higher velocities than those of CH_3OH, with the latter profiles dropping to zero beyond ±15 km s^{-1} from source velocity, independent of the source luminosity. A quantitative analysis shows one order of magnitude decrease in the CH_3OH/H_2O column density ratio as the velocity increases to 15 km s^{-1} (Suutarinen et al. 2014). A similar decrease in the CH_3OH/CO ratio is found, demonstrating that CH_3OH is destroyed in higher velocity shocks, and that not just H_2O increased at larger velocities. A similar lack of CH_3OH (and H_2CO) emission compared with H_2O at higher velocities has been seen at shock positions off source (e.g., Codella et al. 2010; Busquet et al. 2014; Vasta et al. 2012).

These data suggest that sputtering of ices does indeed occur but that the process either shuts off at velocities above 15 km s^{-1}, or that any CH_3OH that is sputtered at higher velocities is destroyed. Destruction of molecules can occur either during sputtering or by reactions with atomic H in the shock. The fact that H_2O is seen up to much higher velocities implies that either H_2O is not destroyed (see below) or that gas-phase formation of H_2O must be active above ±10 km s^{-1} to re-form any water destroyed during sputtering or by other processes such as UV photodissociation (Fig. 16). The data also suggest that sputtering takes place at somewhat lower velocities than the expected 15 km s^{-1}, or that the sputtered molecules have been slowed down since being released into the gas.

For NH_3, the same phenomenon is observed (Fig. 18). NH_3 is also found to emit only at low velocities up to ±15 km s^{-1} at shock positions off source (e.g., Gómez-Ruiz et al. 2016). Since NH_3 has similar excitation requirements as H_2O, this must be a chemical effect. Similar to the case for CH_3OH, destruction by atomic H in the shock is proposed (Viti et al. 2011). However, the barrier for the H + NH_3 reaction is about 5000 K, much higher than that for H + CH_3OH of about 2200–3000 K. The barrier for H + H_2O destruction is even higher, ~10^4 K, allowing H_2O

to survive following sputtering. If only temperature-sensitive destruction would play a role, the relative abundances of these three molecules could provide a thermometer for the higher velocity gas. More likely, however, high-temperature gas-phase formation of H_2O in the high velocity gas controls the difference between these three species.

Shocks are also expected to sputter silicates from grain mantles and cores for shock velocities above 20–25 km s^{-1}, with SiO long known to be one of the best tracers of shocks (e.g., Martín-Pintado et al. 1992; Caselli et al. 1997; Schilke et al. 1997; Jiménez-Serra et al. 2008). How do the SiO and H_2O profiles compare? Figure 18 presents the case of NGC 1333 IRAS 4A showing similarly broad profiles for the two molecules, as also found in some other sources (e.g., Leurini et al. 2014). In other sources such as L1448-MM, SiO is only found in the EHV bullets but not in the broad component (Nisini et al. 2013). In yet other cases, SiO is found at intermediate velocities (e.g., Vasta et al. 2012; Busquet et al. 2014). One explanation for L1448-MM is that the jet gas is rich in atomic Si originating from its dust-free launch position in the inner disk. This then leads to SiO formation in the jet by gas-phase processes, a mechanism proposed originally by Glassgold et al. (1991) and revisited theoretically by Tabone et al. (2020), not because of sputtering of ambient dust grains. Whether SiO is also seen in the broad component then depends on the details of the wind-cloud interaction. An alternative option is that these differences reflect the time evolution of the SiO profiles going from high to low velocities as the shocked gas slows down, as modeled by Jiménez-Serra et al. (2009). Spatial evidence for SiO evolution from high to lower velocities with distance from the source (or equivalently, time) is found in ALMA images of outflows (Tychoniec et al. 2019). Clearly, H_2O line profiles are less sensitive to such time evolution effects.

5.6. H_2O vs. HCO^+

As Fig. 4 shows, HCO^+ is effectively destroyed by reactions with H_2O so that an anticorrelation between these two species is expected, both in position and velocity (e.g., Phillips et al. 1992; Bergin et al. 1998). This anticorrelation has recently been demonstrated observationally through mm interferometric images of $H_2^{18}O$ (or CH_3OH as a proxy) and $H^{13}CO^+$ (Jørgensen et al. 2013; van 't Hoff et al. 2018a). These lines trace quiescent warm envelope gas, however, not the shocked gas.

The broad shocked H_2O gas line profiles observed with *Herschel*-HIFI can be compared with HIFI HCO^+ $J = 6$–5 profiles, covered serendipitously in the 557 GHz setting, or with JCMT HCO^+ $J = 4$–3 profiles from low- to high-mass sources convolved to the *Herschel* beam (Carney et al. 2016). Figure 18 shows that HCO^+ generally avoids the high velocities and is limited to ±5 km s^{-1} around source velocity, although in some sources a weak underlying component out to ±10 km s^{-1} is seen (e.g., Kristensen et al. 2010; San José-García 2015; Carney et al. 2016; Benz et al. 2016; Mottram et al. 2017). HCO^+ thus seems to trace primarily parts of the envelope that are away from locations in the outflow where water is enhanced, consistent with the chemical expectations.

In summary, the combination of H_2O data with those of other species confirm the chemical schemes outlined in Fig. 4, including the anticorrelation with HCO^+. Both high temperature chemistry and ice sputtering contribute to the water abundance, with ice sputtering limited to the low velocities. UV radiation reduces the water abundance in outflows to orders of magnitude below the expected abundance of $H_2O/H_2 = 4 \times 10^{-4}$.

6. Cold dense pre-stellar cores

Herschel-HIFI was unique in its ability to obtain velocity-resolved water line profiles in cold dense clouds, and will remain so in the coming decades. Such data allowed a much deeper analysis than just deriving beam-integrated column densities, as is normally done from spectra taken at a single position. In fact, the detailed line profiles combined with water's ability to probe motions at a fraction of a km s^{-1} make it possible to reconstruct the actual water abundance profile as a function of position in the core, in spite of not spatially resolving or mapping the cloud. This allows stringent testing of the primary chemical processes controlling the gaseous water abundance. At the same time, constraints on physical parameters that are difficult to determine otherwise are obtained, most notably the external and internal UV radiation fields that control photodesorption and photodissociation (Caselli et al. 2012; Schmalzl et al. 2014).

A similar analysis can be carried out for other species, in particular NH_3 observed with *Herschel*-HIFI. Since NH_3 is also abundant in ices, comparison with H_2O can be insightful into how, where and why the nitrogen chemistry in dark clouds is so different from that of other species (Hily-Blant et al. 2017; Caselli et al. 2017).

This section describes the results of the water abundance profile analysis for dense cores prior to star formation combined with our new analysis of the NH_3 profile; the next section does so for the cold outer parts of protostellar envelopes which have an internal heat source. In both cases, simplified chemistry networks as described in Sect. 3.2 are coupled with a physical structure of the source. These chemistry models can be run either in steady-state or in a time-dependent mode at each position in the cloud. For pre-stellar cores at densities $>10^6$ cm^{-3} the chemistry is faster than the free-fall time of 0.03 Myr, so the chemistry reaches steady-state before the physical conditions change (Keto et al. 2014). In the time-dependent case, abundances at $t = 0$ need to be assumed, with results depending on whether oxygen is initially in atomic or molecular form.

6.1. Observations and column densities

6.1.1. Low-mass cores

Within the WISH program, only one low-mass pre-stellar core, L1544, was observed deep enough with HIFI in the ground-state o-H_2O line for detection and detailed analysis (13.6 h integration) (Caselli et al. 2012). The line is very weak but shows an inverse P Cygni profile. Assuming an ortho/para ratio of 3, the inferred H_2O column for L1544 integrated over the entire line of sight is $>1 \times 10^{13}$ cm^{-2} from the absorption part of the feature. This corresponds to a fractional gaseous water abundance $H_2O/H_2 > 1.4 \times 10^{-10}$, with the lower limit stemming from the moderate optical depth of the line. The fact that water is seen in emission in the blue-shifted part of the line profile implies high central densities, about 10^7 cm^{-3}. The same deep spectrum also includes the o-NH_3 1_0–0_0 transition, showing clear emission lines and resolving the hyperfine structure for the first time in space (Caselli et al. 2017).

A second starless core observed in WISH, B68, has a slightly less stringent upper limit of $N(\text{o-}H_2O) < 2.5 \times 10^{13}$ cm^{-2}, or a fractional abundance $H_2O/H_2 < 2 \times 10^{-9}$. Both of these results re-inforce the original conclusions from *SWAS* and *Odin* (Bergin et al. 2002; Klotz et al. 2008) that the gaseous water abundance is very low in cold clouds and that most of the water must be locked up as water ice.

Two additional very deep integrations (15 h each) were obtained in an OT2 program (PI: P. Caselli; Caselli et al., priv. comm.) on the low-mass cores L183 and Oph H-MM1. Both show weak absorption features, with that for Oph H-MM1 included in Fig. 10. As for B68, their lower central densities compared with L1544 do not favor water emission but their central continuum emission is strong enough to absorb against. Upper limits on the gaseous H_2O abundance integrated along the line of sight are again low, $<10^{-9}$.

6.1.2. High-mass cores

Four high mass cores that were thought to have no associated star formation prior to *Herschel* launch were targeted within WISH. The low-lying H_2O lines are detected in all four sources (Shipman et al. 2014). Three of the four sources show outflow wings, however, demonstrating that they are not truly pre-stellar. Nevertheless, after subtraction of the outflow component, their inverse P Cygni profiles greatly resemble those of L1544 and of the low-mass protostars discussed below, but over a wider range of velocities. The fourth source, G11.11-0.12-NH_3, shows no signs of star formation. It has narrow ($FWHM \approx 2$ km s^{-1}) water absorption lines (Fig. 10), even in $H_2^{18}O$, that allow an accurate water column density determination. Assuming ortho/para = 3, the inferred abundance is again low, 4×10^{-8}.

6.2. Inferred H_2O and NH_3 abundance profiles

Herschel-HIFI confirmed the overall picture of low gas-phase water and high ice abundances in cold clouds, but could do much more by inferring the water abundance profiles across the cores. These profiles can then be compared with models such as those by Hollenbach et al. (2009) through coupling of the chemistry with a physical model of the source to infer critical parameters (Caselli et al. 2012).

L1544 is an excellent example, since it has gradients in temperature, density and velocity through the core that are well constrained by other observations. The observed inverse P Cygni profile allows the blue-shifted emission part to be connected with the dense central part of the core, and the red-shifted absorption with the infalling lower-density outer part. The strong absorption indeed points to a relatively high water abundance of $\sim 10^{-7}$ in the outer layer as expected due to photodesorption of water ice by the external UV radiation field (Fig. 19, Appendix D). The central emission requires a significantly higher water abundance than the original value of 10^{-12} in the Hollenbach et al. (2009) model. Adding cosmic-ray induced UV photodesorption of water ice to the model raises the central abundance to $\sim 10^{-10}$–10^{-9}, sufficient to explain the emission. The best fitting water abundance profile for L1544 is included in Fig. 19.

If grain surface formation followed by photodesorption would dominate the production of gas-phase NH_3 as well, its abundance structure should follow that of H_2O. However, such an abundance structure gives a poor fit to the data (Caselli et al. 2017). A much better fit is obtained with a constant or slightly increasing (rather than decreasing) abundance structure toward the center. Such an abundance profile was previously inferred from radio observations with the Very Large Array (VLA) of p-NH_3 by Crapsi et al. (2007). Thus, gaseous NH_3 and H_2O have very different distributions in dense cores, with a much higher contribution of cold gas-phase chemistry than ice chemistry for NH_3 compared with H_2O (Le Gal et al. 2014; Sipilä et al. 2019).

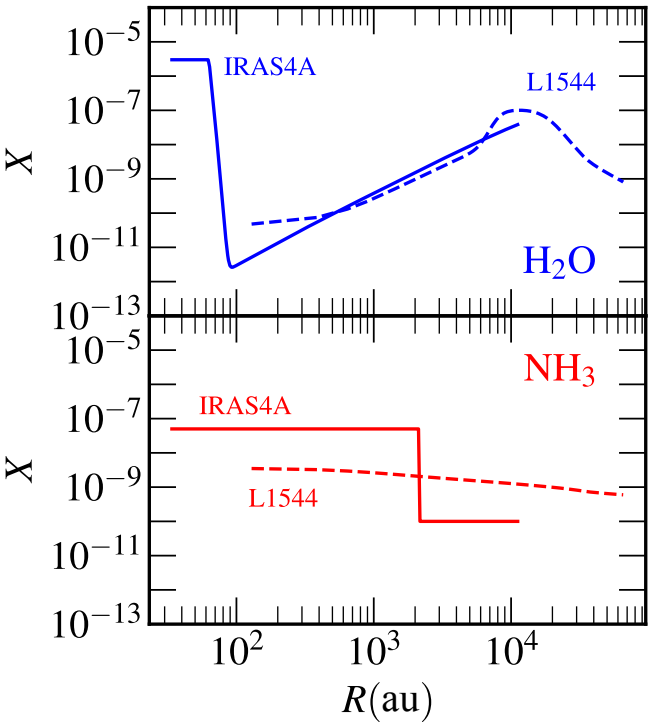

Fig. 19. Best-fit H_2O (*top*) and NH_3 (*bottom*) abundance profiles (with respect to H_2) as functions of position in the NGC 1333 IRAS 4A protostellar envelope (full lines) and the L1544 pre-stellar core (dashed lines) based on analysis of HIFI spectra. Note the similarity of the outer water abundance profiles for the pre-stellar core and outer protostellar envelope, and the very different chemical behavior of H_2O versus NH_3. Based on results from Caselli et al. (2012); Mottram et al. (2013); Caselli et al. (2017) and new analyses (see Fig. 22). The inner hot core H_2O abundance for IRAS 4A is taken from Persson et al. (2016).

7. Protostellar envelopes: cold outer part

Is this behavior for H_2O and NH_3 also seen for protostellar sources? The cold outer parts of protostellar envelopes are in many aspects similar to pre-stellar cores, but protostars have a more strongly centrally concentrated density structure as well as an internal heating source, facilitating both absorption in the outer layers and emission from the inner part of their envelopes. As discussed in Sects. 4.3 and 4.5, the low-lying H_2O lines toward protostars – from low to high mass – indeed show narrow (inverse) P Cygni profiles superposed on the outflow components in some fraction of sources (Fig. 11), indicating either infall or expansion. When the outflow components are subtracted, the residual line profiles can be analyzed in a similar way as those for the pre-stellar cores.

7.1. Inferred abundance profiles

7.1.1. Simple chemistry analysis using SWaN network

To analyze the water data, the temperature and density structure of protostellar envelopes has been coupled with the (simplified) SWaN water network (Sect. 3.2) (Schmalzl et al. 2014). An important difference with pre-stellar cores is the temperature structure: as soon as a protostar has turned on in the center, a temperature gradient is established throughout the envelope, with temperature decreasing with radius R as roughly $R^{-0.4}$ in the region where the far-infrared dust emission is optically thin.

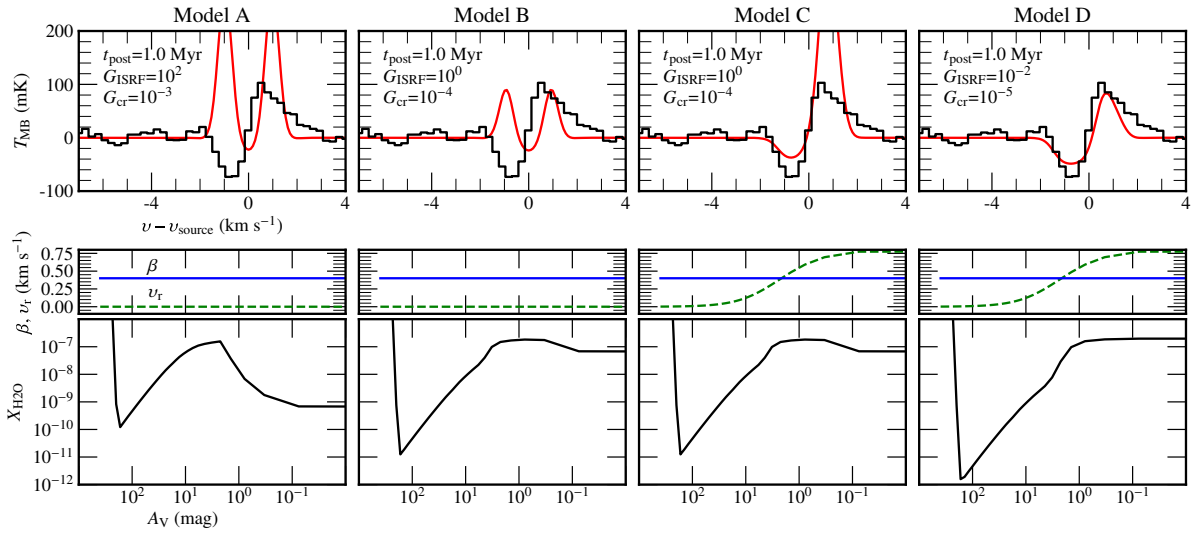

Fig. 20. Illustration how various physical and chemical parameters can be constrained using the SWaN network. H_2O $1_{01}-1_{01}$ 557 GHz observations of the Class I source L1551-IRS5 are compared with SWaN models assuming different parameters for the FUV fluxes and velocity profile. *Top row*: observations (black) together with the synthetic spectra (red). *Bottom row*: adopted velocity profile (green) and water abundance profile (with respect to H_2) (black). A constant Doppler broadening of $\beta = 0.4$ km s^{-1} is assumed, whereas the radial velocity profile is either taken to be constant at 0 (Models A and B) or to have an expansion profile (Models C and D). The radiation fields G_{ISRF} and G_{CR} strongly decrease from model A to model D. A pre-stellar stage duration of 0.1 Myr is used. Based on Schmalzl et al. (2014).

The actual dust temperature structure can be computed with full continuum radiative transfer calculations given a luminosity and density structure of the core, both fitted to the SED and extent of the submillimeter continuum emission assuming spherical symmetry (e.g., Jørgensen et al. 2002; Kristensen et al. 2012). Gas and dust temperatures are taken to be coupled, which is a valid assumption at these high densities. The chemistry is run in time-dependent mode. The initial abundances for the protostellar phase are taken from a model of a cold, constant density ($n_H = 2 \times 10^4$ cm^{-3}) pre-stellar cloud at an age of ~1 Myr, starting the chemistry with oxygen in atomic form. Thus, protostellar models consist of a two-stage approach: a pre-stellar and protostellar stage, with the duration of each of these stages as free parameters.

Figure 19 shows the resulting gaseous water abundance with radius of a typical low-mass source (NGC 1333 IRAS 4A) (Mottram et al. 2013; Schmalzl et al. 2014) in comparison with that inferred for L1544 (Keto et al. 2014). In the coldest outer part of the cloud with $T < 100$ K, the abundance structure is remarkably similar to that of L1544, with a water peak abundance of $\sim 10^{-7}$ due to ice photodesorption at $A_V \approx$ few mag and then a rapid decrease in gaseous water abundance going inward. This steep decrease is largely due to the steeply increasing H_2 density, which is the denominator in H_2O/H_2, coupled with H_2O freeze-out on grain mantles. Once the threshold for thermal desorption is reached, the gaseous water abundance quickly returns to the overall oxygen abundance in the model of $\sim 10^{-4}$.

This general behavior has been demonstrated in detail for a number of low-mass protostars, both Class 0 (Mottram et al. 2014) and Class 0-I (Schmalzl et al. 2014). The main parameters that control the shape of the line profiles are the external UV radiation G_{ISRF} and the internal cosmic ray field G_{CR} (all in units of the Habing 1968 field[5]), together with the details of the velocity profile (infall or expansion). Best fit models generally find an internal cosmic ray induced UV field that is slightly below the normal value ($G_{CR} \lesssim 10^{-4}$), with 10^{-4} the standard number for a cosmic-ray ionization rate of $\sim 10^{-17}$ s^{-1} (Shen et al. 2004). More precisely, the amount of water vapor produced by photodesorption scales with the product $n_{gr}\sigma_{gr}G_{CR}$ with n_{gr} the number of grains and σ_{gr} its geometrical cross section. Thus, the results scale with the inverse of grain radius a, and somewhat lower values of this product can also imply dust growth to micron-sized particles deep inside the core, as has been found observationally (Pagani et al. 2010).

The results are insensitive to the timescale of the protostellar phase t_{proto} over the 0.1–1 Myr range. The absolute values are, however, highly sensitive to the duration of the pre-stellar stage. In fact, the observations of both water gas and ice for the same line of sight can only be reconciled within this modeling framework if a rather short pre-stellar phase is assumed of ~0.1 Myr to avoid turning all oxygen into water ice (see discussion in Sect. 10.1).

Figure 20 illustrates the power of the simple SWaN network to constrain these parameters for the case of the L1551-IRS5 Class I source. From left to right, the external interstellar radiation field, the velocity profile, and the internal cosmic-ray induced radiation fields are systematically adjusted to get the best fit to the observed H_2O $1_{01}-1_{01}$ 557 GHz line profiles. For this source, both a low external and internal radiation field are required, together with a radially expanding velocity field to get the P Cygni line profile. The best-fitting H_2O abundance profile in model D is similar to that found in Fig. 19 for IRAS 4A.

More generally, the inferred external UV field is very low for all sources analyzed, $G_{ISRF} \approx 0.01$, suggesting that the outer protostellar envelopes on scales of ~10 000 au are shielded from UV radiation by a water-free column with $A_V = 2-3$ mag in extent. For a few sources an elevated ISRF with $G_{ISRF} > 1$ is found, most notably for sources in Corona Australis where the young B-star R CrA sets up a PDR across the cloud (Schmalzl et al. 2014).

7.1.2. Step-function analysis

The alternative approach to analyze water data is to use a simple step-function profile with an outer (freeze-out at $T < 100$ K)

[5] To convert to units of Draine (1978) field, divide G_0 by a factor of 1.7.

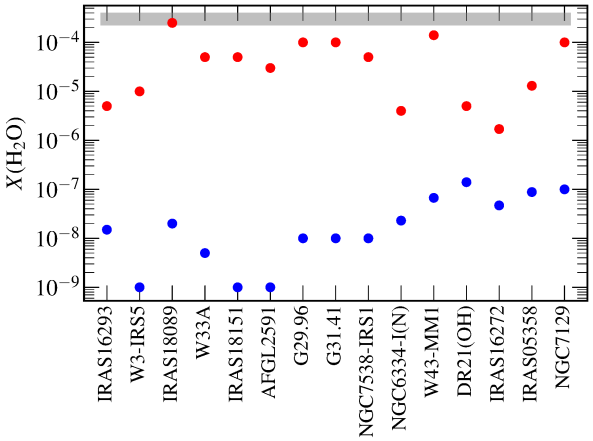

Fig. 21. Inner hot core (red circles) and outer cold envelope (blue circles) water abundances with respect to H_2 in high mass protostars, derived using a step-function analysis. Inferred abundances for a low mass (IRAS 16293-2422) and an intermediate mass (NGC 7129) source are shown for comparison. Uncertainties are typically factors of a few, but see text for the limited meaning of outer abundances. The gray bar at the top shows the warm water abundance expected if all oxygen is driven into water. Based on Herpin et al. (2016); Choi (2015); Coutens et al. (2012); Johnstone et al. (2010).

and inner (sublimation >100 K) abundance. A slightly more sophisticated method is a "drop abundance" profile, with the latter including an outer ice photodesorption layer (Coutens et al. 2012). As shown in Mottram et al. (2013, their Figs. 4 and 14), the main features of the water chemistry are captured by the drop profile, but the outer abundances have a limited meaning. For example, for NGC 1333 IRAS 4A the best fit drop abundance profile has an outer abundance of 3×10^{-10} and a photodesorption layer abundance of 3×10^{-7}, whereas Fig. 19 shows a steadily decreasing abundance profile between 10^{-7} and 10^{-11}.

One intermediate (NGC 7129) and thirteen high-mass protostars have been analyzed using the step-function profiles (Johnstone et al. 2010; Marseille et al. 2010; Chavarría et al. 2010; Herpin et al. 2016; Choi 2015). The inferred outer abundances $X_{\rm out}$ (with respect to H_2) range from 10^{-9} to 10^{-7} and are plotted in Fig. 21. There is no obvious trend with luminosity or envelope mass, which is not surprising given its sensitivity to external UV and the discussion above on analysis methods.

7.2. H_2O vs. NH_3 abundance profile

HIFI observations of the NH_3 1_0-0_0 572 GHz line have been taken for a number of low-mass sources as part of an open time program (PI: P. Hily-Blant). As for pre-stellar cores, the gas-phase NH_3 abundance in the outer envelope would be expected to follow that of H_2O if both were produced primarily on the grains and returned to the gas by photodesorption of ice. However, such an abundance profile is again a poor fit to the NH_3 spectrum in the best studied case of NGC 1333 IRAS 4A. The best-fit NH_3 abundance is a constant abundance of 7×10^{-8} over much of the envelope, with a slightly lower value in the outermost photodissociation layer (Fig. 22). Overall, the inferred NH_3 abundance profile for this low-mass protostar is similar to that found for the pre-stellar core L1544 (Fig. 19). The similarity of the observed NH_3 spectra for other sources suggests that this abundance structure is a common feature.

The inferred constant NH_3 abundance is inconsistent with current chemical models (Caselli et al. 2017). Yet NH_3 ice is observed at an abundance of a few % of that of H_2O ice in a wide variety of sources (e.g., Bottinelli et al. 2010; Öberg et al. 2011a; Boogert et al. 2015), so the abundance of $s-NH_3$ is known to be about 10^{-6} with respect to hydrogen. The bulk of the observed gaseous NH_3 with HIFI has an abundance of a few $\times10^{-8}$, which is a few % of that of ice. This value is higher than can be explained by photodesorption of ice. Thus, the observed gas-phase NH_3 is likely formed primarily through gas-phase reactions (Le Gal et al. 2014) in a route that preserves a constant abundance with increasing density and that is apparently not included, or with a too low rate coefficient, in current gas-phase models (Caselli et al. 2017; Sipilä et al. 2019).

7.3. Cold water deuteration

Lines of deuterated water, HDO, have been observed as part of the (extended) WISH program, most notably the $1_{11}-0_{00}$ line at 893 GHz connecting with the HDO ground state. Figure 23 provides examples of high quality HIFI $1_{11}-0_{00}$ spectra near 1 THz of both H_2O, $H_2^{18}O$ and HDO, all obtained in a similar beam of ~20″.

Similar to the H_2O lines, the 893 GHz line is very well-suited to determine the HDO abundance profile, and thus the HDO/H_2O abundance ratio, in the cold outer envelope. Higher-lying HDO lines such as $2_{11}-2_{12}$ at 241 GHz and $3_{12}-2_{21}$ at 225 GHz, both of which can be observed from the ground, are more sensitive to the inner warm HDO abundance (see Sect. 8).

The HDO abundance profile has been determined using the same procedure as for H_2O and NH_3. The simplest assumption is that HDO follows H_2O but scaled by a constant factor. Figure 22 shows that this assumption works very well for HDO: a constant HDO/H_2O abundance ratio of 0.025 provides a very good fit to the observed HDO and outflow-subtracted H_2O line profiles for the case of the low-mass protostar NGC 1333 IRAS 4A. A flat abundance profile, such as for NH_3, does not fit well. Thus, HDO follows H_2O.

Since the observed gaseous H_2O results from photodesorption of water ice, this result could imply that the same holds for HDO. Detailed modeling of the H_2O and HDO photodesorption processes by Arasa et al. (2015) has shown that differences in efficiencies are very small, so that no significant corrections to the observed numbers are needed because of differences in desorption efficiencies. However, since photodesorption only proceeds from the top few ice layers, these data would then only probe HDO/H_2O in the outermost ice layers, not in the bulk of the ice (Fig. 5). Moreover, cold gas-phase chemistry can also contribute to the observed ratios (Sect. 3.3 and below).

Using a step-function model, Coutens et al. (2012, 2013a) also infer very high HDO/H_2O ratios of 0.05 for the outermost photodesorption layers of the NGC 1333 IRAS 4A and IRAS 16293-2422 envelopes. Averaged over the entire cold part of the envelopes, however, values of 0.002–0.02 are found (Coutens et al. 2013a). For the Serpens SMM1 source, narrow unsaturated $H_2^{18}O$ and HDO absorption lines are detected (Fig. 23) implying HDO/H_2O = 0.002 integrated along the line of sight. For one high-mass source, G34.26+0.15, Coutens et al. (2014) obtain HDO/H_2O = 0.001–0.002 in the cold part of the envelope.

All observed HDO/H_2O ratios are much higher than the overall [D]/[H] ratio of 2×10^{-5} in the gas, suggesting significant fractionation of water in cold cores, with the upper range values close to those found of some other highly-deuterated molecules such as H_2CO or NH_3 (Ceccarelli et al. 2014). It is important to stress once more, however, that the observed cold HDO/H_2O values do not reflect the bulk HDO/H_2O ice ratios, which are

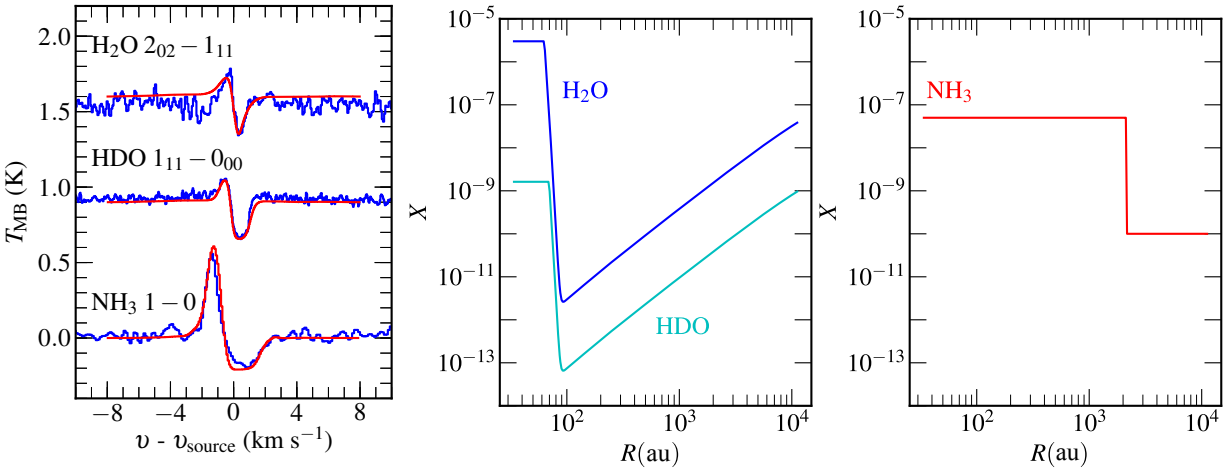

Fig. 22. *Left*: outflow-subtracted HIFI line profiles of H_2O, HDO and NH_3 (blue) toward the low-mass protostar NGC 1333 IRAS 4A overlaid with the best fit model line profiles (red). These model spectra correspond to the abundance structures presented in the *middle and right panels*. The inner H_2O and HDO abundances are set to those found by Persson et al. (2014, 2016).

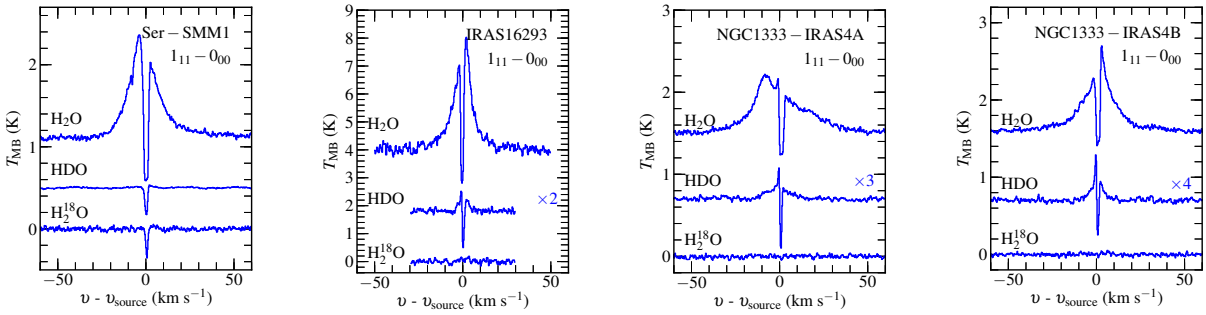

Fig. 23. HIFI observations of H_2O and $H_2^{18}O$ 1_{10}−1_{01} 557 and 548 GHz lines together with the HDO 1_{11}−0_{00} 893 GHz line toward a number of low-mass protostars.

typically $(0.5–1)\times10^{-3}$ as measured in warm hot cores where all ices have just sublimated (Persson et al. 2014; Jensen et al. 2019).

As discussed in Sect. 3.3 and illustrated in Fig. 5, high levels of cold water deuteration are well reproduced by various gas-grain chemical models (Cazaux et al. 2011; Aikawa et al. 2012; Taquet et al. 2013; Albertsson et al. 2014; Wakelam et al. 2014), especially if the multilayer structure of the ice is taken into account (Taquet et al. 2014; Furuya et al. 2016). The bulk of the H_2O is formed early in the cloud evolution, whereas most of the deuteration takes place in the subsequent high density stage where the forward reaction producing H_2D^+ receives a boost from CO freeze-out. The outer layers of the ice are therefore expected to be richer in deuterated water than the inner layers.

Figure 24 presents models of H_2O, HDO and D_2O by Furuya et al. (2016) that follow the chemistry along an infalling stream line from the cold outer part to the warm inner envelope (see also Fig. 3 in that paper). No free atomic oxygen is needed in the high density phase to make deuterated water: the OH resulting from photodissociated water ice can be used to produce HDO. The models of Furuya et al. (2016) and Taquet et al. (2014) find that cold gas-phase chemistry dominates over water ice photodesorption in setting the cold gaseous HDO/H_2O value, and that both result in a roughly constant HDO/H_2O ratio with depth into the envelope (Fig. 24, bottom, full lines at $T < 100$ K). The model value of $HDO/H_2O > 0.1$ in cold gas is however higher than the HDO/H_2O ratio of 0.025 that has been observed for NGC 1333 IRAS 4A.

The main message is that the observed HDO/H_2O ratios in cold gas can be understood using multilayer ice models but that they do not reflect at all the bulk ice ratio. To obtain the HDO/H_2O ratio for the bulk of the ice, for example for comparison with cometary values, observations of hot cores are needed where the entire ice mantle is thermally desorbed above 100 K, as mentioned above and further discussed in Sect. 8.

Alternatively, the bulk HDO/H_2O ice ratio could be measured by infrared absorption. The deepest direct observational limits of infrared ice features give $HDO/H_2O < 0.005–0.02$ (Dartois et al. 2003; Parise et al. 2003). These limits are lower than the tentative HDO ice detections of Aikawa et al. (2012) at a level of HDO/H_2O of a few %. Deeper limits may be obtained with JWST toward ice-rich sources although values down to 10^{-3} or lower, as expected for bulk ice, will remain difficult to probe due to limitations on feature-to-continuum ratios that can be achieved with the instruments.

7.4. Water and the mystery of low O_2 abundances

Standard gas-phase-only chemistry models of cold dark clouds predict that most oxygen is transformed into O_2 with time (e.g., Goldsmith & Langer 1978; Millar et al. 1997). The low abundance of gaseous O_2 in dense clouds measured by the *SWAS* (Goldsmith et al. 2000) and subsequently *Odin* (Larsson et al. 2007) satellites therefore initially came as a surprise. They were readily explained by models that include gas-grain chemistry

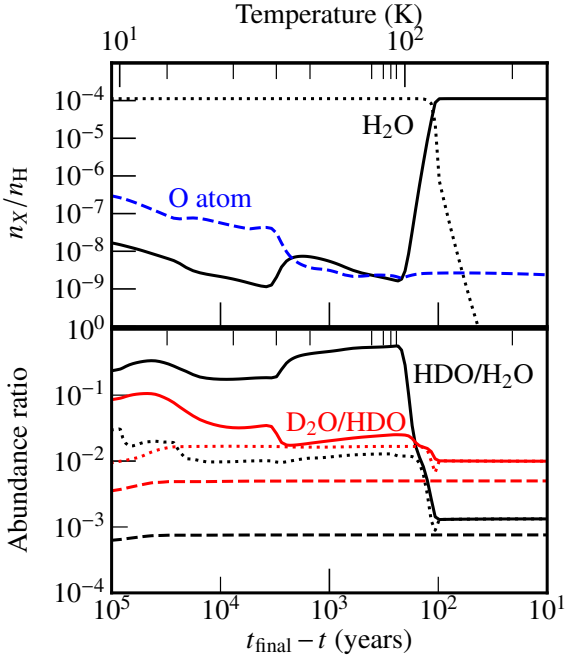

Fig. 24. H_2O, HDO and D_2O gas and ice abundances as function of time following an infalling trajectory from cold outer envelope (*left*) to inner hot core (*right*) using the full multilayer chemistry by Furuya et al. (2016). *Top panel*: water ice abundance (dotted line) in the cold outer part of the envelope, sublimating into gaseous water (solid line) when the parcel enters the ~100 K region. *Bottom panel*: computed HDO/H_2O (black) and D_2O/HDO (red) abundance ratios along the trajectory. Solid lines: gas phase, dotted lines: ice surface layers (*top* ~5% of ice); dashed lines: bulk ice (*bottom* ~95%). The bulk D_2O/HDO ice ≫ bulk HDO/H_2O ice, as also reflected in the warm gas ratios. The cold gaseous HDO/H_2O ratio is very high in this model due to cold gas-phase chemistry; the observed HDO/H_2O value for IRAS 4A is HDO/H_2O = 0.025.

which turn most oxygen into water ice (Bergin et al. 2000), a process now also demonstrated to proceed in laboratory ice experiments at low temperatures (Ioppolo et al. 2008; Miyauchi et al. 2008; Oba et al. 2009). *Herschel*-HIFI has been able to push the observational limits on O_2 even deeper, with gaseous O_2 remaining undetected in most sources. O_2 has only firmly been identified through multiple transitions in the Orion shock (Goldsmith et al. 2011; Chen et al. 2014) and one region in the Oph A cloud (Liseau et al. 2012; Larsson & Liseau 2017), but not, for example, in the Orion PDR (Melnick et al. 2012). Its abundance is only $O_2/H_2 = 5 \times 10^{-8}$ in the Oph A cloud.

It is clear that the stories of the O_2 and H_2O chemistries are intimately linked, and that any model that explains water gas and ice also needs to be consistent with the O_2 data (Fig. 4). Unfortunately, deep upper limits on the O_2 487 GHz line exist for only one low-mass protostellar envelope, the Class 0 source NGC 1333 IRAS 4A (Yıldız et al. 2013a). Using a drop-abundance profile, the inferred 3σ limit is $O_2/H_2 < 6 \times 10^{-9}$ in the cold outer part, the lowest O_2 limit so far. Even in the inner hot core, the observed O_2 abundance cannot be more than 10^{-6}, so O_2 is not locked up in ice at high abundances and released at high temperatures in this particular source. Recent ALMA interferometer data also imply a similarly low gaseous O_2 abundance in the IRAS 16293-2422 hot core (Taquet et al. 2018). Deep unpublished *Herschel* O_2 487 GHz data in a few high-mass protostars such as NGC 6334I and AFGL 2591 have also failed to detect any line at the 3 mK km s^{-1} (3σ) level, pointing to similarly low O_2 abundances as for IRAS4A.

The low observed O_2 abundance of IRAS 4A has been modeled by Yıldız et al. (2013a) by coupling the temperature and density structure of the source with a full gas-grain chemical model. Subsequent radiative transfer models provide line intensities that can be compared directly with the HIFI observations. The results indicate that only models with a long and cold pre-stellar stage of (0.7–1) Myr, coupled with a protostellar stage of about 10^5 yr, are consistent with the data. A long timescale at low temperatures is needed to transform all O and O_2 into water ice, leaving no free oxygen to form O_2. These same models are also able to reproduce a very low O_2 abundance in the hot core. The long timescale seems in contradiction with the conclusion in Sect. 7.1 of a short pre-stellar timescale to avoid the overproduction of water ice. However, no water ice observations exist for IRAS 4A to test this model because it is too faint at mid-infrared wavelengths. This conundrum of reproducing both water gas, water ice and O_2 will be further discussed Sect. 10.

A new twist to the O_2 puzzle has been provided by the detection of abundant O_2 ice in comet 67P by the ROSINA instrument on board the Rosetta mission (Bieler et al. 2015; Rubin et al. 2019). The inferred ratio is $O_2/H_2O \approx 0.03$ in the ice, which would correspond to $O_2/H_2 \approx 3 \times 10^{-6}$ if released in the gas assuming $H_2O/H_2 = 10^{-4}$. This is several orders of magnitude higher than the limit for cold O_2 measured for IRAS 4A and close to the warm O_2 hot core limit (see also Taquet et al. 2018).

A detailed parameter study by Taquet et al. (2016) shows that a O_2/H_2O ice abundance as high as a few % found for comet 67P can only be achieved if the atomic H/O ratio in the gas is low, so that water ice formation is suppressed and O_2 ice production promoted. This, in turn, implies a rather specific narrow range of physical parameters: a relatively high temperature, ~20–25 K, high density, $>10^5$ cm^{-3}, and low cosmic ray ionization rate, $<10^{-17}$ s^{-1}, for the pre-stellar cloud out of which our Solar System formed. A key result of these models is that they are also consistent with the low observed HO_2, H_2O_2 and O_3 abundances in 67P, in contrast with alternative models such as water ice "radiolysis" (that is, processing of ice with ionizing photons) (Mousis et al. 2016). Similarly, other recent models that argue for a primordial origin of the high O_2 in comet 67P by formation in a cold pre-stellar cloud (e.g., Rawlings et al. 2019) do not attempt to simultaneously reproduce these other species.

Such a relatively warm model could also explain the detection of O_2 in the SM1 core of the ρ Oph A cloud, which is known to have enhanced dust temperatures due to illumination by nearby massive B-type star(s). A high gaseous O_2/H_2O abundance is only found at an early chemical age (Taquet et al. 2016) which may not be unrealistic given the measured infall speeds in this core (Larsson & Liseau 2017). For IRAS 4A, these same models are consistent with the low observed limits because the pre-stellar cloud is much colder, 10 K.

8. Hot cores: dry or wet

8.1. Inferred abundances from observations

In the warm inner envelopes close to the protostar, the dust temperature becomes higher than 100 K, at which point all water ice sublimates back into the gas. The size of this so-called "hot core" region scales roughly as $R_{T=100K} \approx 2.3 \times 10^{14} (\sqrt{L/L_\odot})$ cm in a spherically symmetric envelope (Bisschop et al. 2007). For $L = 1$, 100 and 10^4 $L_\odot$, the 100 K radius is at 15, 150 and 1500 au, respectively. Thus, whether for low-mass sources at 200 pc or

high-mass sources at 2 kpc, the hot core region is <1″ on the sky and thus heavily beam diluted in the *Herschel* beams. The region where $T > 250$ K, the temperature at which all volatile oxygen would be driven into water by gas-phase reactions, is even smaller.

Hot core water abundances have been derived by fitting the HIFI line intensities of the higher-lying water lines, especially those of $H_2^{18}O$ or $H_2^{17}O$ that are not affected by outflow emission (see Fig. C.3). Detailed radiative transfer models using a step-abundance profile have been performed for most of the WISH high-mass sources (Herpin et al. 2016; Choi 2015) and one intermediate mass source (NGC 7129) (Johnstone et al. 2010). The resulting inner abundances $X_{\rm in}$ (with respect to H_2) are included in Fig. 21, together with a few results from the literature using a similar approach: the low-mass source IRAS 16293-2422 (Coutens et al. 2012) and the high-mass source NGC 6334I (Emprechtinger et al. 2013), both from the CHESS program. The narrow $H_2^{18}O$ absorption lines toward high-mass sources also indicate a jump in water abundance of at least an order of magnitude at the ∼100 K radius (van der Tak et al. 2019). For most low-mass sources, a step-function analysis has not been possible due to the lack of narrow HIFI $H_2^{18}O$ lines (Fig. 11).

It is clear from Fig. 21 that the inner water abundances range from 5×10^{-6} to $>10^{-4}$, with no trend with luminosity or envelope mass, nor with the ratio $L/M_{\rm env}$, which is thought to be an evolutionary indicator. A few sources have inner abundances of 10^{-4} or higher, as expected from ice sublimation and high temperature chemistry driving oxygen into water, although none as high as the expected value of 4×10^{-4}. The only region with a water abundance that may be as high as 6.5×10^{-4} is a small compact dense clump near the Orion hot core found using HEXOS data Neill et al. (2013). Among a subset of WISH high-mass sources, Herpin et al. (2016) have found a possible trend of higher inner water abundances with higher infall or expansion velocities. This could suggest that sputtering of ice mantles contributes to the water production in the inner region.

In an attempt to probe the inner warm water abundance for LM protostars with *Herschel*, very deep (5 h) HIFI observations of the $H_2^{18}O$ $3_{12}-3_{03}$ 1095 GHz ($E_{\rm up} = 249$ K) lines have been obtained for 6 sources (Visser et al. 2013). This $H_2^{18}O$ line is detected in two low-mass sources, NGC 1333 IRAS 2A and Serpens SMM1 (Fig. C.3), and actually shows narrow profiles with $FWHM \approx 3$ km s^{-1}, so the emission is clearly not associated with the outflow. Deep limits are obtained for the other sources (NGC 1333 IRAS 4A, IRAS 4B; GSS30, Elias 29); the $H_2^{17}O$ line covered in the same setting is not detected at the same noise level (8 mK in 0.5 km s^{-1} bin).

A detailed combined analysis of the IRAS 2A $H_2^{18}O$ HIFI 1095 GHz spectrum and $H_2^{18}O$ $3_{13}-2_{20}$ 203 GHz NOEMA data reveals that even the HIFI water isotopolog line is likely optically thick when coming from a hot core with a radius of 100 au. In contrast, the 203 GHz emission is optically thin. It results from the fact that the Einstein A coefficient for the 1095 GHz line, 1.65×10^{-2} s^{-1}, is a factor of 3400 larger than that of the 203 GHz line, 4.8×10^{-6} s^{-1}. Moreover, the dust continuum emission from the hot core starts to become optically thick at 1 THz on 100 au scales, thus shielding some of the water emission. Altogether, this means that only a lower limit can be placed on the hot core water abundance of $H_2O/CO > 0.25$ or $H_2O/H_2 > 2\times10^{-5}$. Here the $C^{18}O$ 10–9 ($E_{\rm up} = 290$ K) line obtained in the same spectrum has been used as reference for the warm gas assuming $CO/H_2 = 8\times10^{-5}$ inferred for this source (Visser et al. 2013; Yıldız et al. 2012).

Are most hot cores indeed "dry", or is this an artifact of the analysis method? For high-mass sources, the $H_2^{18}O$ 203 GHz line ($E_{\rm up} = 203$ K) has long been recognized to be an excellent diagnostic of water in hot cores, with inferred water abundances of $\sim10^{-5}-10^{-4}$ (e.g., Jacq et al. 1988; van der Tak et al. 2006; Wang et al. 2012). Millimeter interferometers can now also image this line in low-mass hot cores with sub-arcsec resolution (Jørgensen & van Dishoeck 2010b; Persson et al. 2012; Jensen et al. 2019). These data show narrow water lines ($FWHM \approx$ 1–2 km s^{-1}) located within a ∼100 au radius region. Inferred water abundances are low, only $10^{-8}-5\times10^{-6}$ (with respect to H_2) if analyzed within a spherically symmetric model. However, on these scales much of the gas and dust is likely in a flattened disk-like structure, even in the Class 0 phase (Murillo et al. 2013; Tobin et al. 2012, 2016). The temperature in the shielded midplane of the disk, where most of the mass is located, is much lower than 100 K, so the amount of warm H_2 in the denominator can be much smaller.

Modeling the small scale interferometer structure with a nonspherically symmetric model consisting of a disk (compact source) + envelope indeed confirms that only a small fraction of the mass in the inner region is above 100 K (Persson et al. 2016). This raises the fractional water abundances with respect to H_2 by an order of magnitude to $10^{-7}-6\times10^{-5}$, with the latter value applying to IRAS 2A. These water abundances are closer to, but still below, the expected water abundance of 4×10^{-4}.

In summary, when corrections for nonspherical symmetry and optical depths are included, hot cores are not as "dry" as previously thought, but they are not "wet" either, with water abundances still a factor of a few to two orders of magnitude lower than expected (see also Fig. 11 in Persson et al. 2016). Overall, this comparison highlights the fact that *Herschel* was not well suited to determine hot core water abundances, due to the combination of severe beam dilution, high optical depths in line and continuum, and difficulties in isolating the hot core emission from that in the outflows. Studying the chemistry of hot cores is squarely an interferometer project, with NOEMA and now also ALMA opening up the opportunity to image the 203 GHz line, and other $H_2^{18}O$ lines with small Einstein A coefficients and low continuum optical depth, for large numbers of sources. The challenge remains to constrain the amount of warm gas on small scales to determine the water abundance, that is, the denominator in the H_2O/H_2 ratio remains the main uncertainty, rather than just the water column. This will require unravelling the detailed disk-envelope physical structure on <100 au scales.

8.2. Water deuteration in hot cores

There has been no shortage of determinations of the HDO/H_2O ratio in warm gas, using both ground-based and *Herschel*-HIFI observations. Single-dish ground-based determinations of high-mass protostars, using typically the 225 and 241 GHz HDO lines to measure HDO, typically find values as low as $HDO/H_2O = (2-8)\times10^{-4}$ (e.g., Jacq et al. 1990; Gensheimer et al. 1996; Helmich et al. 1996; van der Tak et al. 2006; Emprechtinger et al. 2013; Coutens et al. 2014), with occasionally values up to $(2-5)\times10^{-3}$ (Neill et al. 2013). Interferometer observations of high-mass protostars are still sparse but indicate values of $\sim5\times10^{-3}$ for the disk-like structure of AFGL 2591 (Wang et al. 2012). For low-mass protostars in clustered regions, the interferometer data give HDO/H_2O ratios in the range $(0.6-1)\times10^{-3}$ (Jørgensen & van Dishoeck 2010a;

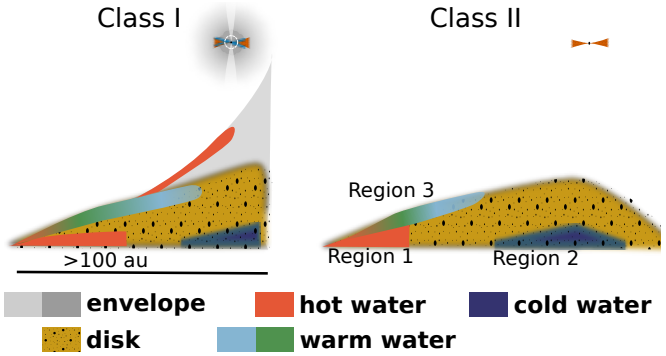

Fig. 25. Water vapor reservoirs in young Class I systems and mature Class II disks. Region 1 lies inside the water ice line where high temperature chemistry drives all oxygen into water near the midplane ($\sim 10^{-4}$ abundance). Region 2 lies beyond the snow line and produces a small amount of water vapor (10^{-11} up to 10^{-7}) through photodesorption of water ice. Region 3 concerns the warm surface layers of the disk out to large radii with moderate water vapor abundances limited by UV radiation ($\sim 10^{-6}$). Regions 1 and 3 extend further out into the disk for the warmer Class I sources. Also, hot water can be emitted in the hot core and in outflows or shocks along the outflow cavity in Class I sources. The small cartoons at the top illustrate the larger scale disk-envelope-outflow cavity system.

Persson et al. 2014). Interestingly, for isolated low-mass protostars, the HDO/H_2O ratios are a factor of ~2 higher (Jensen et al. 2019). Error bars on these ratios for nearby sources observed with interferometers are small, of order 30% or less, since many assumptions about excitation temperature and emitting region for the two species cancel out.

Even with this fairly large range of inferred values, it is clear the HDO/H_2O ratios in warm gas are lower than those for the cold gas of 0.025 presented in Sect. 7.3 by an order of magnitude or more. This is consistent with the models of Taquet et al. (2014) and Furuya et al. (2016) discussed in that section and presented in Fig. 24 (bottom panel, compare full lines at $T <$ and >100 K), namely that the bulk water ice sublimated in hot cores has a lower deuteration fraction than the top ice layers and cold chemistry probed in the cold outer envelopes (see also Fig. 5).

9. Protoplanetary disks

To address the question of the water trail from clouds to planets, the water content of disks at different evolutionary stages needs to be addressed. This section discusses *Herschel*'s contribution to our knowledge of water in forming disks in the embedded Class 0/I protostellar stages as well as in mature disks in the optically visible Class II stage.

To put the *Herschel* observations in context and set the stage for the discussion, it is useful to summarize the expected water vapor reservoirs in disks based on chemical models (Fig. 25). Disks, whether young or mature, have large gradients in temperatures and densities, both radially and vertically. Their surface layers are exposed to intense UV radiation from the young star. Thus, the chemistry varies strongly with position in the disk, with the "snow" or ice-lines of different molecules playing a key role (Öberg et al. 2011b). Overall, models of protoplanetary disk chemistry have identified three different water chemistry regimes (e.g., Woitke et al. 2009; Gorti & Hollenbach 2008; Walsh et al. 2012; Albertsson et al. 2014; Furuya et al. 2013; van Dishoeck et al. 2014; Walsh et al. 2015). Region 1 lies inside the water ice line of ~160 K and has a high water abundance of at least 10^{-4}, with most oxygen contained in water vapor by ice sublimation and high temperature chemistry. Region 2 lies in the outer disk well beyond the ice line, and has a low water vapor abundance ranging from 10^{-11} up to $\sim 10^{-7}$. This water vapor is produced at intermediate disk heights where UV radiation can penetrate and water ice can be photodesorbed from grains (Dominik et al. 2005; Bergin et al. 2010a). Finally, in the warm surface layers of disks (region 3), water vapor is produced by high temperature chemistry in the "warm finger" which has also abundant OH. There the water abundance is limited by photodissociation to a value of $\sim 10^{-6}$.

9.1. Young disks

The preceding sections have shown that most of the water emission from low-mass protostars detected with *Herschel* arises in warm outflows and shocks associated with jets and winds and their interaction with the surrounding envelope, with the gas heated by kinetic energy dissipation. However, as the protostellar system evolves from the deeply embedded Class 0 phase to the late Class I phase, the envelope mass and outflow force decrease whereas the disk grows in mass and size (Hueso & Guillot 2005). Has *Herschel* detected any water emission from these young disks?

Prior to the launch of *Herschel*, the presence of young disks was heavily debated since numerical studies suggested that strong magnetic fields inhibit the formation of disks (Galli & Shu 1993; Li et al. 2014). Recent millimeter interferometric observations of optically thin molecular lines have however revealed flattened disk structures for several Class 0 and I sources targeted by WISH+ that are characterized by Keplerian motion (e.g., Lommen et al. 2008; Tobin et al. 2012; Murillo et al. 2013; Harsono et al. 2014; Yen et al. 2017; Takakuwa et al. 2018; van 't Hoff et al. 2018b; Artur de la Villarmois et al. 2019). Since these data clearly show that young disks are present, the disk's contribution to the H_2O lines observed with *Herschel* needs to be reassessed.

The sizes of the embedded disks are typically 50–100 au, so ~1″ diameter at 140 pc (Harsono et al. 2014). Young disks in the Class 0 and I phase are expected to be warmer than their Class II counterparts with similar mass due to their higher accretion rate and higher bolometric luminosity ($L \gtrsim 1\ L_\odot$, Harsono et al. 2015). Thus, warm young disks may have sufficient amounts of water vapor that could contribute to the HIFI spectra.

9.1.1. Cold water in young disks

A first, purely observational look is to compare the H_2O 1_{10}–1_{01} 557 GHz spectra toward a number of Class 0/I protostars with and without disks (Fig. 26). ALMA observations of the Class 0 protostar B335 ($L = 3.3\ L_\odot$) show no clear evidence for a Keplerian disk inside of 20 au (Bjerkeli et al. 2019). In contrast, the Class I protostar L1489 with a similar luminosity ($L = 3.8\ L_\odot$) is surrounded by a very large rotating structure with a ~700 au radius that may be in transition to the Class II stage (e.g., Brinch et al. 2007; Yen et al. 2014). L1527 is a borderline Class 0/I source (1.9–2.6 $L_\odot$) with a ~100 au warm young disk seen edge-on (Tobin et al. 2012; van 't Hoff et al. 2018b). TMC1A (3.8 $L_\odot$) is a Class I source with a bonafide disk with 50–100 au radius (Harsono et al. 2014, 2018). Finally, the young Class II source DG Tau is included since Podio et al. (2013) suggest that their *Herschel*-HIFI observations of the water ground-state lines at 557 GHz and 1113 GHz are emitted by the disk ($M_{\rm disk} = 0.1\ M_\odot$, $L = 1\ L_\odot$). DG Tau is an interesting case in that it also has a

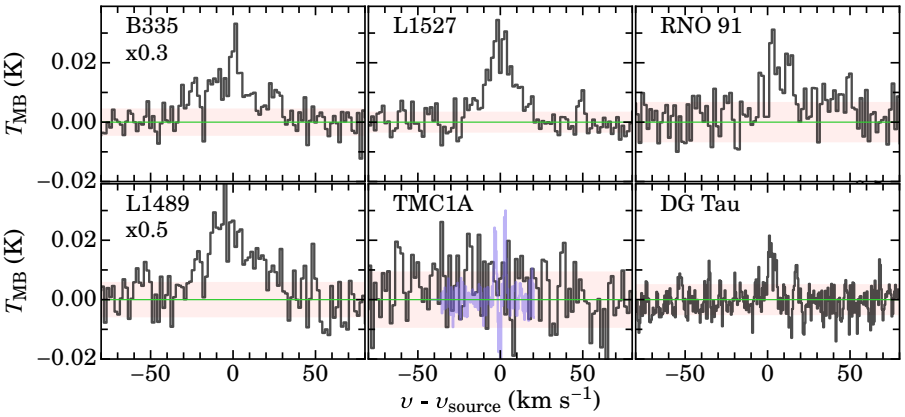

Fig. 26. H_2O $1_{10}-1_{01}$ spectra toward low-mass embedded protostars with and without disk-like structures. RNO91, TMC1A and L1489 are Class I sources with disks; L1527 is a Class 0/I source with an embedded disk whereas B335 is a Class 0 source with no clear evidence for a disk down to 20 au. DG Tau is a young Class II source with disk and jet. These are WBS spectra binned to 0.3 km s^{-1} while B335 is binned to 0.6 km s^{-1} velocity resolution. The horizontal green line indicates the baseline. For TMC1A, the blue line indicates the ALMA ^{13}CO spectrum of the rotating disk to indicate its width (Harsono et al. 2018).

powerful optical jet which emits strong UV and X-rays onto the disk surface (Güdel et al. 2010, 2018).

At first glance, all of these profiles look similar. The B335 spectrum stands out because of its broad line profile with a FWHM of 40 km s^{-1} typical of Class 0 sources while the water lines toward the Class I protostars, when detected, have a typical FWHM of 15–20 km s^{-1} (see Sect. 4.3). Water is also detected toward the Class 0 L1527 source with a FWHM of 20 km s^{-1} but its comparatively low value could be due to the outflow lying close to the plane of the sky. No water emission is detected from TMC1A, which does have a large disk as well as a blue-shifted disk wind (Bjerkeli et al. 2016). Except for TMC1A, the integrated water line intensities follow the observed correlation of $I(H_2O)$ with envelope mass M_{env} and measured outflow force established for a much larger sample (Kristensen et al. 2012; Mottram et al. 2017), but there is clearly no relation with L_{bol} for this subsample. The former relation suggests that the line profiles largely reflect the warm gas associated with the outflow, which has weakened for the Class I sources. Association with the outflow is further strengthened by the fact that spatially resolved H_2O emission has been seen for several of these sources in the PACS data along the outflow direction, see Figs. 4, D.1 and D.2 in Karska et al. (2013) for L1527, L1489 and TMC1A.

Could the "double peaked" profile reflect disk emission? Fig. 26 includes the observed ^{13}CO 2–1 line profile observed with ALMA from the inclined TMC1A disk and its disk wind showing a typical FWHM of 8 km s^{-1}. This is close to the maximum line width expected for outer disk rotation: even for mature disks around Herbig stars ($M_* > 1$ $M_\odot$), CO line profiles do not span more than 10 km s^{-1} (Thi et al. 2001; Dent et al. 2005). The comparison between L1489 and DG Tau shows that the DG Tau line is narrower than most Class I sources, as expected from a disk, although cloud or wind absorption can also (asymmetrically) affect the profiles.

Are the observed line intensities consistent with those from a disk? The simplest approach is to compare expected line intensities from optically thick water emission within the ice line. For high accretion rates, the midplane temperature increases and the water ice line shifts outward, from radii of only a few au in mature, nonaccreting disks to values as high as 60 au for accretion rates of 10^{-4} $M_\odot$ yr^{-1} (Harsono et al. 2015). There could also be water emission from the remnant warm inner envelope (Sect. 8). The maximum water emission can then be computed by considering optically thick line emission within a ∼100 au radius at 100 K and then diluted by the *Herschel* beam. This gives an integrated line intensity of ∼20 mK km s^{-1} for the 557 GHz line for disks at 150 pc, which is a factor of 5 below the upper limit for TMC1A of ∼100 mK km s^{-1}. For low accretion rates, the model intensities drop steeply with the reservoir of photodesorbed water (region 2) providing a minimum floor.

In order to further quantify the young disk's water contribution to the observed spectra, a good physical model of the envelope + disk system inside of 100 au is required. This limits such an analysis to two Class I sources, TMC1A and L1489. Here the case of TMC1A is illustrated, for which the physical model is taken from Harsono et al. (2018). In these models, the water abundance in region 2 is assumed to vary from 10^{-11}–10^{-7}. Region 3 is assumed to have an abundance of 10^{-6} and is taken to lie at $T_{gas} > 250$ K and A_V between 0.5 and 2 mag. The UV radiation is typically $G_0 > 5000$ at $A_V < 0.5$ mag, so that water is easily photodissociated there.

The gas temperature is decoupled from the dust temperature in the surface layers following Bruderer et al. (2012) whereas an accretional heating rate of 10^{-7} $M_\odot$ yr^{-1} is included in the midplane. The predicted H_2O $1_{10}-1_{01}$ peak line temperatures from such a model are low, ranging from 0.15 to 2 mK for the highest abundance in region 2, well below the noise level of 8–13 mK rms in 0.3 km s^{-1} bin in the *Herschel* spectra. In these models, most of the emission comes from region 3 ($T_{gas} >$ 250 K) due to the combined high excitation and column density that extends up to 100 au. Region 2 only contributes if the water abundance is as high as 10^{-7}.

In conclusion, to detect cold water vapor emission from young disks with *Herschel* the observations would need to have been much deeper than the typical 15–30 min integration times used in WISH+ for Class I sources. For Class II disks, much longer integration times of >10 h have been adopted, but even then only few detections have been found (see Sect. 9.2). Given that Class 0 and I disks are overall warmer and more massive than their Class II counterparts with dust less evolved, they could have higher water fluxes but future far-infrared space missions will be needed to test this.

9.1.2. Warm water in young disks

Exploratory searches for warm water in young disks have recently been undertaken with NOEMA and ALMA through the (nonmasing) $H_2^{18}O$ $3_{1,3}-2_{2,0}$ ($E_{up} = 203$ K) 203 GHz and $4_{1,4}-3_{2,1}$ ($E_{up} = 322$ K) 390 GHz lines (e.g., Jørgensen & van Dishoeck 2010b; Persson et al. 2016; Harsono et al. 2020). By targeting $H_2^{18}O$, any outflow emission is minimized, as evidenced by the narrow lines observed for Class 0 sources. In contrast with Class 0 sources, however, no $H_2^{18}O$ lines are detected for

Class I sources. The current limits for four Class I sources suggest that any warm water must be located inside of 10 au (region 1) (Harsono et al. 2020). No ALMA 203 GHz data have yet been taken toward Class I sources, so future ALMA observations that are up to an order of magnitude more sensitive and higher angular resolution than was possible with NOEMA are needed. For region 3, the $H_2^{18}O$ column is too low to contribute, in contrast with the case for the main water isotopolog discussed in Sect. 9.1.1.

The nondetections of warm water with ALMA are significant for other reasons as well. It is well known that the infall of high velocity envelope material onto the low velocity disk can cause a shock, raising temperatures of gas and dust at the disk-envelope interface to values much higher than those provided by heating by stellar photons alone. These accretion shocks are widely found in models and simulations (Neufeld & Hollenbach 1994; Li et al. 2013) but have not yet been unambiguously observed. In the early stages of disk formation, the accretion occurs close to the star at high velocities, but that material ends up in the star, not the disk. With time, the accretion quickly moves to larger disk radii (tens of au) with typical shock speeds of <10 km s^{-1} impacting gas with densities >10^7 cm^{-3}. For these conditions, molecules in the infalling gas largely survive the shock but gas temperatures just behind the shock reach up to 4000 K. These high temperatures drive most of the oxygen in OH and H_2O and should result in bright far-infrared lines. The dust temperature is also raised, but only to about 50 K (assuming 0.1 μm grains), enough to release weakly bound molecules but not strongly bound species such as H_2O (Visser et al. 2009; Miura et al. 2017). Some sputtering of ice mantles can also occur. The fact that no warm water vapor emission is detected with ALMA near the young disk on 50 au scales for either L1527, Elias 29 or TMC1A (Harsono et al. 2020) limits the importance of any such shocks.

Interestingly, warm water emission in the $H_2^{16}O$ $10_{2,9}$–$9_{3,6}$ (E_{up} = 1863 K) line at 321.2 GHz has been observed with the SMA toward the Class I source HL Tau, known to have a large disk structure seen in the continuum (100 au radius) with ALMA (ALMA Partnership 2015). The nonmasing part of this line is blueshifted by 20 km s^{-1}, has a FWHM of 25 km s^{-1}, and extends over 3–4″, or ~500 au. These characteristics suggest that the bulk of the water emission originates in the protostellar jet or wind, not in the rotating disk itself. Similarly, Watson et al. (2007) found highly excited water lines in the *Spitzer* mid-infrared spectra of the Class 0 source NGC 1333 IRAS 4B which they attributed to an accretion shock onto the young disk. However, Herczeg et al. (2012) concluded based on *Herschel*-PACS data (taken as part of WISH), that both the mid- and far-infrared water emission is consistent with an outflow origin.

For high-mass protostars, bonafide Keplerian disks of several hundred au radius have been identified using the high spatial resolution of ALMA (e.g., Johnston et al. 2015; Moscadelli et al. 2019; Izquierdo et al. 2018). The large beam of *Herschel* makes it difficult to isolate the water coming from young disks for these objects, so they will not be considered here. Also, these disks are warm and are therefore better targets for ALMA. Indeed, vibrationally excited water lines (v_2 = 1, $5_{5,0}$–$6_{4,3}$, E_{up} = 3462 K) with Keplerian rotation have been detected toward disks around proto-O and B stars on <1000 au scales (Ginsburg et al. 2018; Maud et al. 2019), but no water abundance has yet been quantified. Nevertheless, further spatially resolved water observations of rotational transitions in vibrational states toward disks around high-mass protostars will be interesting to understand the water evolution during disk formation in different environments.

9.2. Protoplanetary disks

9.2.1. Cold water in mature disks

Background. *Herschel*-HIFI was unique in probing the cold water vapor reservoir in planet-forming disks, through velocity-resolved observations of the two ground-state rotational transitions of ortho-H_2O 1_{10}–1_{01} line at 557 GHz and the para-H_2O 1_{11}–0_{00} line at 1113 GHz. With upper-level energies of 53 and 61 K, and critical densities of ~1×10^8 and ~7×10^8 cm^{-3}, respectively, emission can be expected from across the disk. This includes the cold (<50 K) outer disk regions, although subthermal excitation conditions need to be taken into account when interpreting the observations. It is these outer disk regions that will dominate the signal in the large *Herschel* beams of 38″ and 19″ at the respective line frequencies if the water vapor abundance is sufficiently high. Since the beam sizes exceed those of disks (typically diameters of no more than a few arcsec), the expected main-beam antenna temperatures are small. Although *Herschel* cannot spatially resolve the emission, HIFI's high spectral resolution (<0.1 km s^{-1}) allows the emission lines from suitably inclined disks to be velocity-resolved, thus providing constraints on the radial origin of the emission if standard Kepler orbital speeds are assumed.

As discussed above, theoretical considerations predict water vapor to occur in three distinct regions in disks, as illustrated schematically in Fig. 25 and in Fig. 27 for one specific Herbig disk (e.g., Dominik et al. 2005; Woitke et al. 2009; Cleeves et al. 2014). The small radial extent of the region 1 results in a negligible contribution of the expected flux in the *Herschel* beam in the ground-state lines (<10% of total emission). In contrast with young disks, region 3 also contributes little to the emission in the ground-state lines in the *Herschel* beam (<30%), because of the low column density and the low H_2 density that precludes efficient excitation of the lines. Outside these two regions, water is generally expected to be frozen out onto cold (<150 K) dust grains, as evidenced by the handful of detections of water ice in planet forming disks (e.g., Chiang et al. 2001; McClure et al. 2015; Min et al. 2016; Honda et al. 2016). Region 2 consists of the cold water vapor reservoir produced by UV photodesorption of water ice into the gas phase (e.g, Andersson & van Dishoeck 2008; Öberg et al. 2009), with water vapor abundances of up to 10^{-7} relative to H_2 predicted at intermediate disk scale heights out to large radii. In this region, densities of a few times 10^7 cm^{-3} and temperatures of 30–45 K are sufficient to generate detectable emission in the *Herschel* beam.

HIFI results and models. The main observational result from *Herschel* on the ground-state rotational water lines from mature disks, is that the emission is even weaker than expected on theoretical grounds. *Herschel*-HIFI observed the ortho-H_2O 1_{10}–1_{01} line toward ten disks around T Tauri stars and four disks around Herbig Ae stars as part of the WISH+ programs (Table A.1). A subset of these targets were also observed in the para-H_2O 1_{11}–0_{00} line with similar results and are not further discussed here. The observations and their results are presented in Hogerheijde et al. (2011) and Hogerheijde et al. (priv. comm.), Salinas et al. (2016), and Du et al. (2017).

In summary, out of the fourteen observed sources, only two yielded detected lines (TW Hya and HD 100546; Fig. 28) in spite of long integrations and rms levels down to 1.2–2.0 mK in 0.27 km s^{-1} channels. A stacked spectrum of AA Tau, DM Tau, LkCa 15 and MWC 480 also yielded a significant detection of the line. These detections correspond to the data with the longest

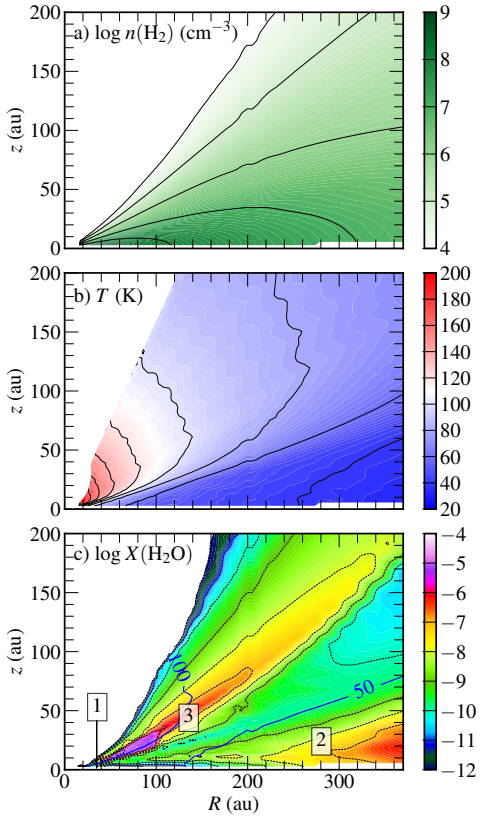

Fig. 27. Cross section of one quadrant of a model of a Herbig disk, tailored to that around HD 100546. (*a*) H_2 number density, (*b*) gas temperature (taken equal to the dust temperature), and (*c*) calculated H_2O abundance. Further details of the model can be found in the text and references. The H_2O abundance can be divided in three regions as indicated (see also Fig. 25).

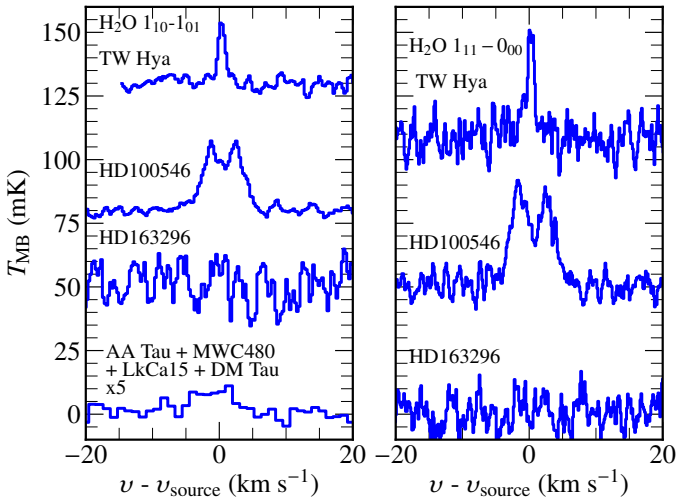

Fig. 28. Overview of detected emission of H_2O 1_{10}–1_{01} (*left*) and 1_{11}–0_{00} (*right*) with *Herschel*-HIFI to TW Hya, HD 100456, HD 163296 and the stacked results of AA Tau, MWC 480, LkCa 15, and DM Tau. Data from Hogerheijde et al. (2011); Du et al. (2017), *Herschel* archive and Hogerheijde et al. (priv. comm.).

integration times (typically >10 h) and thus lowest noise levels. For all other sources, observed to various rms levels, only upper limits were obtained. Figure 29 shows the detections and upper

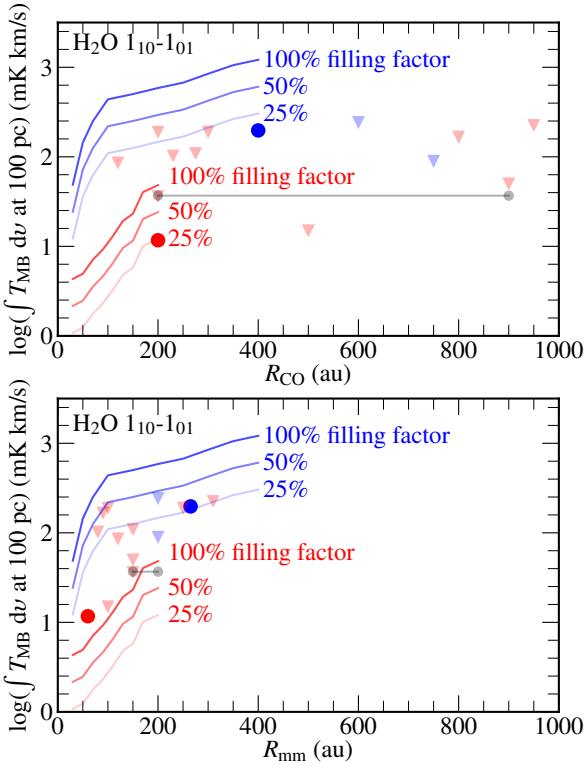

Fig. 29. Line luminosities of models and observations of ortho-H_2O 1_{10}–1_{01} for planet-forming disks observed with *Herschel*-HIFI. Solid blue and red lines show predicted line luminosities for a Herbig disk model (blue) and a T Tauri disk model (red); see text for details. Note the logarithmic scale. The effects of non-unity filling factors are illustrated by shaded lines at 50 and 25%. The observational data are from Hogerheijde et al. (2011); Du et al. (2017) and Hogerheijde et al. (priv. comm.). Filled circles show detections, blue for the Herbig star HD 100546 and red for the T Tauri star TW Hya. The gray circles connected by the solid gray line show the detected line luminosity of the stacked detection of AA Tau, LkCa15, MWC 480 and DM Tau. Down-pointing triangles show upper limits (blue: Herbig disks; red: T Tauri disks). Data are plotted versus the observed size of the disk as measured through CO emission (*upper panel*) and mm-wavelength continuum emission (*lower panel*); for the stacked detection (gray line) the range of disk sizes is plotted. Observed disk sizes are taken from Walsh et al. (2014); Andrews et al. (2012); Loomis et al. (2017); Bergin et al. (2016); Kudo et al. (2018); Jin et al. (2019); Qi et al. (2003); Liu et al. (2019); Fedele et al. (2017); Huang et al. (2016); Dutrey et al. (2003, 2016); Hughes et al. (2009); Macías et al. (2018); Isella et al. (2016); Boehler et al. (2018); Huélamo et al. (2015); Cleeves et al. (2016). Line luminosities and disk sizes are scaled to the latest *Gaia* distance estimates.

limits in terms of velocity-integrated line luminosities, using the most up-to-date distances of the sources obtained from *Gaia*.

Figure 29 plots the observed line luminosities and the upper limits as function of the gas and dust outer radii of the disk as measured in ^{12}CO emission and through the mm-continuum emission. It also compares the observations to the expected emission for a "typical" T Tauri disk (red) and a "typical" Herbig Ae disk (blue). For the T Tauri disk, the TW Hya model of Hogerheijde et al. (2011) and Salinas et al. (2016) is used: a disk mass of 0.04 $M_\odot$, disk outer radius of 200 au, and a disk inclination of 7°. For the Herbig disk, a model of the HD 100546 disk is adopted (Hogerheijde et al., priv. comm.): a disk mass of 0.01 $M_\odot$, a disk outer radius of 400 au, and a disk inclination of 42°. In both cases, the disk temperature is calculated

self-consistently and the disk chemistry includes photodesorption due to stellar UV photons. The H_2O excitation and emission line luminosity is calculated using LIME version 1.9.5[6] (Brinch & Hogerheijde 2010) and H_2O collisional rates from Dubernet et al. (2009) (taken from the LAMDA database Schöier et al. 2005). While the T Tauri and Herbig disk models have a fixed outer radius, the effect of confining the emission from water to a smaller region is mimicked by artificially setting the water abundance to zero outside a certain radius. Figure 29 plots the predicted emission from these models against this radius. Predicted fluxes for Herbig disks are higher than for T Tauri disks because of the higher temperature of the former; due to the subthermal excitation of the water molecule, a factor of two difference in temperature strongly affects the excitation.

Comparison of the model curves with the two detected disks (TW Hya and HD 100546) and many of the upper limits confirms the earlier reported results, namely that the H_2O ground-state rotational emission from disks is weaker than expected by factors of 5–10. Bergin et al. (2010a) and Hogerheijde et al. (2011) suggested that this indicates a reduction of water ice at intermediate disk heights where stellar ultraviolet photons can still penetrate. These authors hypothesize that settling of (icy) grains can, over time, remove significant fractions of the water ice reservoir (see also Kama et al. 2016; Krijt et al. 2016, 2020). A similar overall reduction of volatile material was inferred by Du et al. (2017) for the full sample.

Salinas et al. (2016) put forward a different scenario for TW Hya, where the observed fluxes are reproduced when the icy grains are taken to spatially coincide only with the millimeter-sized grains as probed by the submm continuum emission. Andrews et al. (2012) find that in the TW Hya disk, these grains are confined to ~60 au, much smaller than the 200 au found for the gaseous outer disk radius as seen in CO emission. Figure 29 shows that much better agreement between the TW Hya detection and the model curve is found when the former is plotted at the detected radius of the mm emission. Although in this case the model underpredicts the line luminosity of TW Hya, it should be remembered that these model curves are produced by setting the water abundance to zero outside the plotted radius, and do not include transporting the water ice from larger radii to smaller radii. No exact agreement would therefore be expected in this simple minded comparison. In contrast to TW Hya, for HD 100546 reducing the emitting area to that of the millimeter-sized grains (~265 au, Walsh et al. 2014) does not sufficiently reduce the emission.

Instead of reducing the size of the emitting region radially, introducing a non-unity filling factor can also produce a reduction of the line luminosity. Figure 29 shows that scenarios where as little as 25% of the disk out to the CO outer radius is filled with H_2O emitting material, reproduces the observed line fluxes and many of the upper limits. Such filling factors may be appropriate for several of the disks in the sample, if most of the water ice is spatially coincident with the mm-continuum emitting grains. High-resolution ALMA studies show that such grains are confined in many (bright) disks to rings or bands covering only small fractions of the disks (e.g., Andrews et al. 2018; Long et al. 2019; van der Marel et al. 2015). For the particular case of TW Hya, the disk is found to be relatively uniformly filled with mm-continuum emitting grains out to ~60 au, while for HD 100546 the disk's mm emission is dominated by a 15–45 au ring (Pineda et al. 2019). While such a ring takes up only 1% of the total disk area (out to 400 au), it does leave open the possibility that the H_2O emission originates from only limited radial ranges inside the disk.

The three scenarios outlined above can all explain the weak H_2O emission found in the spatially unresolved *Herschel*-HIFI observations: (i) overall reduction of volatile material in the vertical regions of the disk subjected to UV radiation; (ii) a uniform radial confinement to the disk area rich in mm-continuum emitting grains; and (iii) H_2O emission regions carved up in rings or bands reminiscent of the resolved submm substructures seen in many bright disks.

For one disk, it is possible to go one step further. The detected spectrally resolved line toward the suitably inclined disk of HD 100546 (Fig. 28) holds information on the radial origin of the emission. A simple model with a radial power-law dependency for the line emission suggests that the H_2O emission originates from radii between 40 au out to 250–300 au (Hogerheijde et al., priv. comm.). While the outer radius is not very well determined due to the adopted radial power-law drop off of the emission, the inner radius is robust and indicates that the emission originates outside the bright ring of mm continuum emission seen with ALMA (Pineda et al. 2019). Likely, this dust ring is optically thick at the frequencies of the observed water lines (557 and 1113 GHz), obscuring the water emission. The inferred region of water vapor emission actually overlaps with the 40–100 au region where water ice absorption has been detected (Honda et al. 2016).

Summary and future prospects. In summary, the *Herschel*-HIFI observations of the water rotational ground state lines toward fourteen planet-forming disks show that water vapor is present in at least five of these for which the lowest noise levels were obtained. Theoretical models suggest that this water vapor likely originates from photodesorption of icy grains, but that the reservoir of available water ice is smaller than expected. Radial confinement in a single region or several radial rings or bands, or vertical confinement at heights below where UV photons can penetrate, can all explain this. Whichever mechanism is at work, a close relation with the settling, growth and radial transport of dust grains seems implicated. The low gas-phase abundance of cold water vapor is also in line with the inferred low gas-phase oxygen and carbon abundances in the TW Hya outer disk (Favre et al. 2013; Du et al. 2015, 2017; Bergin et al. 2016; Bergner et al. 2019). If low oxygen and carbon abundances go together, then the low volatile carbon abundances inferred from weak CO emission in many other mature disks (e.g., Miotello et al. 2017; Long et al. 2017) suggests that this is a common feature.

The prospects of further investigating the distribution of cold water vapor across disks requires spatially resolved observations. ALMA observations of lines of water isotopologs provide a possible avenue. However, available $H_2^{18}O$ transitions such as the 203 GHz line (Sect. 8) have lower-level energies exceeding 200 K, and do not trace the cold reservoir of water ice (<150 K). Several low-lying HDO transitions are observable with ALMA in Bands 8 and 10, but their interpretation is complicated by the required knowledge of the deuteration fractionation.

A highly promising avenue to constrain the radial distribution of gas-phase water was pioneered by Zhang et al. (2013), who analyzed multiple transitions of water from HIFI and PACS in TW Hya to derive a radial abundance profile and snowline location by adopting a temperature structure for the disk. SPICA and the Origins Space Telescope (25–588 μm) offer the possibility to extend such studies to a statistically significant sample of disks.

[6] https://github.com/lime-rt/lime

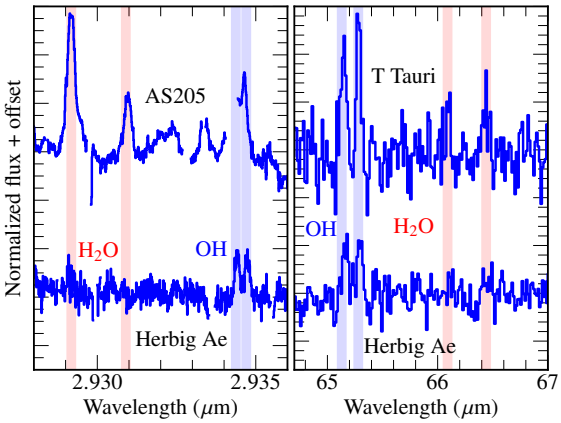

Fig. 30. Water observations of protoplanetary disks at near-infrared wavelength with VLT-CRIRES and far-infrared wavelengths by *Herschel*-PACS in typical T Tauri and Herbig disks. The VLT-CRIRES spectra are for individual disks, AS 205 and HD 250550, whereas the PACS spectra are obtained by stacking multiple spectra. Data from Fedele et al. (2011, 2013).

9.2.2. Warm water in mature disks

The *Spitzer*-IRS detected a wealth of highly-excited pure rotational lines of warm water at 10–30 μm in disks around a significant fraction of T Tauri stars (Carr et al. 2004; Carr & Najita 2008, 2011; Salyk et al. 2008, 2011, 2015; Pontoppidan et al. 2010b), with line profiles consistent with a disk origin (Pontoppidan et al. 2010a; Salyk et al. 2019). Typical water excitation temperatures are $T_{\rm ex} \approx 450$ K. Spectrally resolved groundbased near-IR vibration-rotation lines around 3 μm show that in some sources the hot water originates in both a disk and a slow disk wind (Salyk et al. 2008; Mandell et al. 2012).

Abundance ratios extracted from the *Spitzer* observations are uncertain because the lines are highly saturated and spectrally unresolved. Nevertheless, within the more than an order of magnitude uncertainty, $H_2O/CO \approx 1-10$ has been inferred for emitting radii up to a few au (Salyk et al. 2011; Mandell et al. 2012). This indicates that the inner disks of those sources where water is prominently detected have high water abundances of order 10^{-4} and are thus not dry, at least not in the surface layers down to where the dust becomes optically thick at mid-IR wavelengths.

In contrast with the case for young disks in the Class 0 and I stages, no NOEMA or ALMA observations of warm $H_2^{18}O$ lines in Class II disks have yet been published. Emission of more highly excited lines, however, has been detected using *Herschel*-PACS (e.g., Fedele et al. 2012, 2013; Rivière-Marichalar et al. 2012) and these transitions, when combined with longer wavelength HIFI and shorter wavelength *Spitzer*/VLT/Keck infrared lines, provide insight into the gas-phase water abundance inside the water snowline (Fig. 30).

Interestingly, the HD 100546 Herbig disk, which has prominent HIFI lines pointing to cold water in the outer disk (Fig. 28), does not show any detection of warm water lines from the inner disk with PACS or VLT. In contrast, the HD 163296 disk has no detected HIFI lines, but does show a (stacked) detection of warm water with PACS (Fedele et al. 2013). These two stars and their luminosities are similar, so the global disk thermal structure cannot be the explanation. Instead, disk substructures in gas and dust likely are. One possibility is that water ice is trapped in the outer disk of HD 100546 by the bright dust ring at 40 au (Pineda et al. 2019) (see discussion in Sect. 9.2.1), whereas the icy pebbles have drifted inward for HD 163296. This would be consistent with the high CO abundances detected inside the CO snowline in the HD 163296 disk (e.g., Booth et al. 2019).

Another illustrative case of the importance of dust traps in regulating the inner warm water reservoir is provided by the TW Hya disk, the only other disk for which HIFI ground-state cold water lines are clearly detected. Based on *Spitzer* spectra of warm water combined with H_2, the inner few au of the TW Hya disk are found to be oxygen poor by a factor of ~50. This points to an efficient water ice dust trap just outside the snowline around 2.4 au (Bosman & Banzatti 2019).

More generally, Banzatti et al. (2017) find a correlation between water line fluxes and size of an inner disk gas cavity, as measured from CO ro-vibrational line profiles for a set of T Tauri and Herbig disks. Water emission first disappears at near-infrared wavelengths (hot water) and then at mid-infrared wavelengths (warm water) as the radius of gas emission expands out to the water ice line. This suggests that infrared water spectra are a good tracer of inside-out water depletion in regions 1 and 3 from within to outside the snow line. Banzatti et al. (2020) also find an anticorrelation between the water line fluxes in *Spitzer* data and the radius of the mm-sized dust disk, suggesting that small disks where icy dust grains have drifted inward have higher warm water abundances.

10. Water and the oxygen budget

Sections 5–9 have quantified the abundances of water vapor and other oxygen-containing molecules such as OH and O_2 in different components of protostellar sources: outflows and shocks, pre-stellar cores, cold and warm envelopes around protostars, and in young and mature disks. This section looks at the question whether we have now accounted for all of the oxygen.

The broader issue of the oxygen budget from the diffuse ISM to dense clouds and comets was introduced in Sect. 3.1 and is summarized in much more detail in Appendix G. The overview Table 3 and Fig. 32 are included here in the main text of the paper. As discussed in Sect. 3.1, some fraction of oxygen appears to be locked up in an unknown form called UDO (Unidentified Depleted Oxygen) even in the diffuse ISM, assuming a total oxygen abundance of $[O] = 5.75 \times 10^{-4}$ or 575 ppm.

10.1. Water gas + ice abundance in protostellar envelopes: the oxygen budget mystery

The HIFI lines have allowed a detailed gaseous water abundance profile through the envelope to be derived (Sect. 7), but this chemical analysis ultimately has to be consistent with observations of other oxygen carrying species, most notably water ice and O_2 gas (Sect. 7.4). There are only a limited number of sources for which both water ice and gas have been observed along the same line of sight, since most deeply embedded Class 0 sources were too faint at mid-infrared wavelengths for ice absorption studies with *Spitzer*. In fact, there is no source for which all three species – water gas, water ice and deep O_2 gas limits – are available.

Nevertheless, surveys of water ice exist for large samples of infrared-bright low- and high-mass protostars, revealing typical water ice column density ratios $N_{\rm s-H2O}/N_{\rm H} \sim 5 \times 10^{-5}$ (e.g., Gibb et al. 2004; Pontoppidan et al. 2004; Boogert et al. 2008, 2015; Öberg et al. 2011a; Whittet et al. 2013). Similar values of $(2-6) \times 10^{-5}$ are measured toward stars behind dark quiescent clouds (Boogert et al. 2013). The column density of hydrogen

Table 3. Oxygen budget of various species in ppm assuming overall [O] = 575 ppm.

Form	Species	Diffuse clouds	Low-mass YSO	High-mass YSO	Shocks	Comets
Dust	Refr. Dust	140	140	140	140	140
	Refr. Organics	–	–	–	–	50
Gas	O	320	?	?	30	–
	H_2O	<1	40	≤62	80	–
	CO	1	100	100	100	–
	CO_2	–	<1	<1	<1	–
	O-other	–	–	–	–	–
Ice	H_2O	<2	38	31	–	323
	CO	<1	10	3	–	10
	CO_2	<1	24	8	–	30
	CH_3OH	<1	3	4	–	1
	O-other	<1	1	1	–	21
UDO		115	219	226	225	–

Notes. See Appendix G for references to the adopted numbers in this table and their uncertainties. The ice abundances for protostars are as observed, without hiding ices in large grains.

nuclei, $N_H \approx 2N(H_2)$, is inferred either from the silicate optical depth, or from the color excess toward the star, or from a combination of the two. Observed values show a range of a factor of two around this mean.

The important implication of these water gas + ice observations is that water gas contains a negligible fraction of oxygen and that even water ice locks up only a moderate fraction, $\lesssim$20%, of the volatile interstellar oxygen abundance with respect to total hydrogen of 3.2×10^{-4}, that is, the oxygen that is not locked up in silicates (Sect. 3.1). In other words, not all volatile oxygen observed in diffuse clouds ends up as water ice in the dense cloud phase. A similar conclusion was reached by comparing gas and ice for high-mass protostellar envelopes by Boonman et al. (2003a). As shown in Sect. 7.4, O_2 contains at most a few %.

There are four possible explanations for this conundrum: (i) water ice formation is suppressed, with most oxygen locked up in other volatile species; (ii) water ice or gas is destroyed after formation, with oxygen driven into other species; (iii) the water ice abundance inferred from observations is underestimated; and (iv) the fraction of oxygen locked up in refractory UDO increases from diffuse to dense clouds. The following analysis focuses on low-mass protostars, but the same arguments hold for high-mass protostellar envelopes.

10.1.1. Suppressing water ice formation

Regarding option (i), our modeling of both the water gas and ice using the SWaN network demonstrates that the only way to get a low water ice column is to start with a low water ice abundance in the pre-stellar stage (Schmalzl et al. 2014). Water ice cannot be effectively destroyed in protostellar envelopes at temperatures lower than 100 K, but some additional water ice can be made in the coldest outer parts where the dust temperature is below $\lesssim$15 K, which could increase the ice column by up to a factor of ~2 (see Fig. 4 in Schmalzl et al. 2014). This limiting temperature of ~15 K is set by the binding energies of atomic and molecular oxygen, either of which is needed to make water ice. Once the temperature is above this critical temperature, which holds for the bulk of the protostellar envelope, no new water ice can form and the water ice abundance is 'frozen in' at the value given at the start of the protostellar phase, $t = 0$. The Schmalzl et al. models use $E_b = 800$ K for atomic O, but the more recent higher values of $E_b = 1660$ K on water ice (He et al. 2015) only exacerbate the problem by increasing the amount of water ice that can be formed in the protostellar stage.

How can the water ice abundance in the pre-stellar stage be limited? Starting from oxygen in atomic form, as would be appropriate for an earlier more diffuse cloud phase, water ice formation is fast (Cuppen & Herbst 2007). Current models thus require a short pre-stellar phase, typically only 0.1 Myr at densities $>10^4$ cm^{-3}, to limit water ice formation (Schmalzl et al. 2014). This timescale is shorter than the estimated duration of ~0.5 Myr from pre-stellar core statistics (Enoch et al. 2008).

Full gas-grain models can test how much oxygen is processed into other species than O, O_2 and H_2O. Figure 31 presents the abundances in gas and ice of major oxygen-bearing species as functions of position in the IRAS 4A envelope, together with their sum, using the three-phase chemical network of Furuya et al. (2016, 2017). Initial abundances are identical to those in Schmalzl et al. (2014), with $[O_{vol}] = 3.2 \times 10^{-4}$. The temperature and density structure of the source is taken to be the same as that used to analyze the H_2O and HDO spectra in Sect. 7.1 (Fig. 22).

After a short cold pre-stellar phase of 0.1 Myr, most oxygen is still in atomic form with an O abundance of 1.6×10^{-4} (Fig. 31, left panels). The water ice abundance varies with depth, but its integrated abundance along the line of sight is only 0.5×10^{-4} with respect to total H, consistent with the ice observations. In contrast, for a long pre-stellar phase of 10 Myr (right panels), all oxygen is in water ice at the start of the protostellar phase with no change with depth. Velocity resolved observations of cold atomic [O I] in emission or absorption could in principle distinguish between these scenarios, but may be difficult to interpret because of large optical depths.

In what form is the remaining oxygen in these models? As expected, the O_2 abundance is indeed strongly affected by the duration of the pre-stellar phase: at 10 Myr, all the oxygen is in water ice with very little gaseous O_2, in contrast with the 0.1 Myr case. As the bottom panels of Fig. 31 show, some fraction is in CO and CO_2 gas or ice. At most 20% of the volatile oxygen, about 60–70 ppm, is in other species in either model, mostly H_2CO, CH_3OH and minor oxygen-containing species. All of these results are consistent with those presented in Schmalzl et al. (2014), which used a much simpler chemical model.

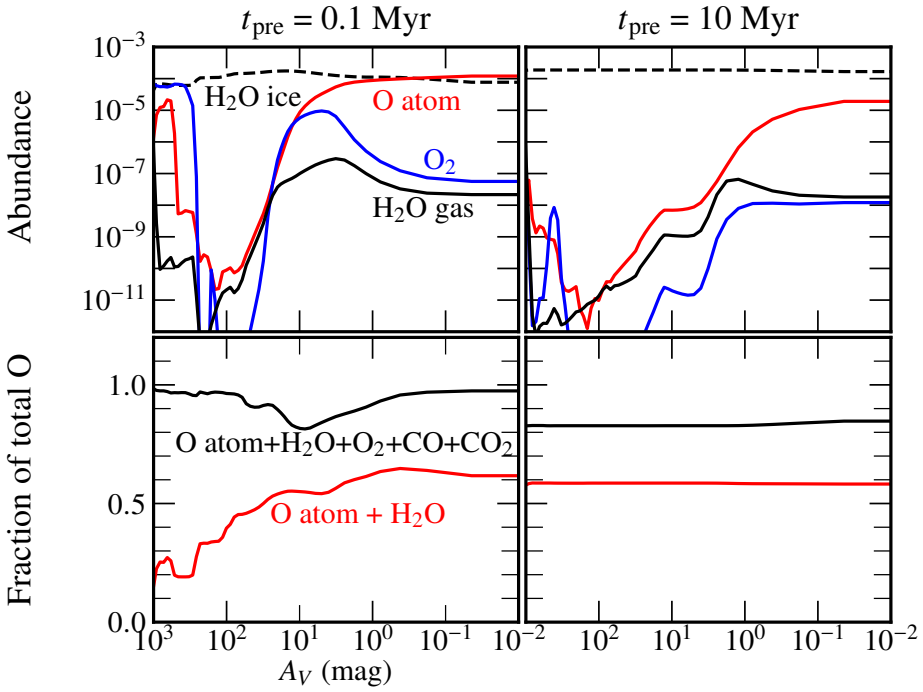

Fig. 31. Full multilayer gas-grain model results for water and related chemical species for the temperature and density structure of the NGC 1333 IRAS 4A envelope model using the Furuya et al. (2016) chemical network, for two different timescales of the pre-stellar phase: 0.1 and 10 Myr. *Top panel*: gaseous O, O_2 and H_2O (full lines) and H_2O ice (dashed lines). O_2 is seen to be strongly reduced in the 10 Myr case. *Bottom figure*: includes the sum of the abundances of other major O-bearing species in the models in both gas + ice. The remaining oxygen is in H_2CO, CH_3OH and other larger organic species.

The models presented in Fig. 31 assume a static physical structure with time. Figure 24 (top) shows the result of the water chemistry in a collapse model such as described by Furuya et al. (2016) in one dimension and Visser et al. (2009) in two dimensions. There a streamline is followed from the outer edge of the envelope inward, assuming a pre-stellar phase of 10 Myr. Consistent with the static case, the H_2O ice abundance stays high even though different conditions are experienced "en route". In conclusion, the only way to suppress H_2O ice formation is through a short pre-stellar stage.

10.1.2. Water destruction after formation

For option (ii), episodic accretion and heating during the protostellar phase has been proposed as a possible way to decrease the water ice abundance. It is now well established that most protostars undergo multiple luminosity outbursts during the embedded phase of star formation, increasing the luminosity by up to a factor of 100 for a short period of time, typically <100 yr (e.g., Evans et al. 2009; Dunham & Vorobyov 2012; Audard et al. 2014). The enhanced luminosity heats the envelopes to higher temperatures, sublimating water ice out to larger radii and re-freezing it once the envelope has cooled back down again, but with some delay due to the fact that the freeze-out time is longer than the cooling time (Visser & Bergin 2012; Frimann et al. 2017). If water gas could be driven into other oxygen-containing molecules during a luminosity burst before re-freezing, this could suppress the water ice abundance compared with the pre-stellar stage and lessen the requirement on its short time scale. However, detailed chemical models have failed to make this scenario work in practice under protostellar conditions (e.g., Taquet et al. 2016; Eistrup & Walsh 2019).

10.1.3. Ice columns underestimated due to grain growth

Another solution (iii) is that the water ice absorption measurements underestimate the true water ice column. This could be the case if some fraction of grains along the line of sight are large enough (typically a few μm) that they do not show any absorption feature. This situation has been proposed for the diffuse ζ Oph cloud where also some fraction of oxygen is unaccounted for (Poteet et al. 2013). For our much denser protostellar sources, only a small fraction of the grains needs to be large. As a toy-model example, assume two dust populations: a standard one with grain size $a_s = 0.1$ μm, and a large-grain population with $a_\ell = 10$ μm. The latter population would not show water ice absorption even if covered with ice. The relative abundances are adjusted so that the overall grain abundance is 6.5×10^{-13} with respect to hydrogen if all grains have $a = 0.1$ μm (corresponding to a gas/dust mass ratio of ~100). The parameter to vary is the ratio of large to small grains $f_{\rm large}$. The equations in the SWaN network by Schmalzl et al. (2014) have been adjusted for oxygen freeze-out onto the two different grain sizes. The fraction of traceable water ice by infrared absorption is then taken to be the amount of ice on small grains relative to the total amount of water ice on both small and large grains. This analysis shows that a fraction $f_{\rm large} = 0.01\%$ of the grain population in 10 μm-sized grains (by numbers) would catch 50% of the atomic oxygen during freeze-out and make it invisible. Assuming $a_\ell = 1$ μm would move the 50% point to $f_{\rm large} = 1\%$.

This scenario is highly plausible, given the substantial observational evidence for grain growth to μm size in dense clouds (e.g., Pagani et al. 2010; Boogert et al. 2013; Steinacker et al. 2015) and protostellar envelopes (e.g., Chiang et al. 2012; Miotello et al. 2014). These μm-sized grains likely coagulated from ice-coated small particles (since they carry the largest surface area), thereby natively locking up water ice within larger grains. This would have the added benefit that there does not need to be a major fraction in atomic oxygen but there is still room for some fraction of UDO. For dark quiescent clouds prior to star formation, which also show low water ice abundances, the observed low water ice abundances could be an early evolutionary effect with water ice still being formed, although even there grain growth could start in the denser parts.

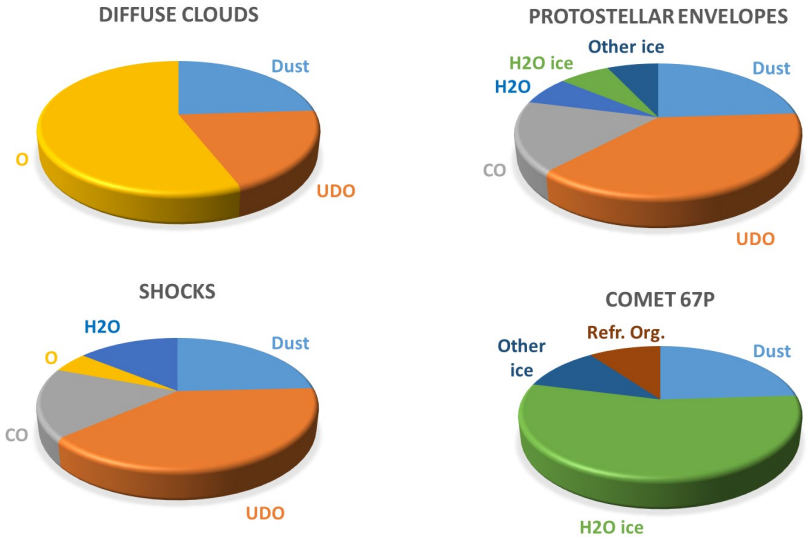

Fig. 32. Partitioning of oxygen in different forms of gas, ice and dust in (*a*) diffuse clouds; (*b*) protostellar envelopes (low- and high-mass); (*c*) shocks; and (*d*) comet 67P. The amount of oxygen in refractory dust is kept constant at 140 ppm in all cases.

10.1.4. Increasing UDO from diffuse to dense clouds

The fourth possibility is that oxygen is locked up in increasing amounts in some refractory form called UDO as the density increases (Table 3) (Jenkins 2009; Whittet 2010). This scenario is further discussed in Sect. 10.4.

In summary, the combined observations of gaseous and solid water in protostellar envelopes allow the water gas and ice abundances to be constrained quantitatively as functions of radius. The initial pre-stellar ice abundance is a crucial parameter that sets the ice abundance profile in protostellar envelopes. Unless the pre-stellar stage is very short, it is difficult to prevent all volatile oxygen being turned into water ice. Alternatively, the pre-stellar stage could be longer, and the observed low ice abundances are then most easily explained by some fraction of grains having grown to at least μm size. The final option is that the fraction of oxygen in UDO has increased from diffuse to dense clouds.

10.2. Hot cores

The above models and discussion concerned the outer part of the protostellar envelope where water is frozen out. Section 8 shows that the gaseous water abundance in the inner hot core region inside the water ice line is also generally lower than the expected value of $H_2O/H_2 = 4 \times 10^{-4}$. If most hot cores are indeed dry, where is the remaining oxygen? Any water ice locked up in large grains, as in option (iii), should also have sublimated. Photodissociation by UV radiation from the young star-disk accreting boundary layer (LM) or the stars themselves (HM) can rapidly destroy water, but only in a narrow region of visual extinctions or in outflow cavities through which UV photons can escape (Stäuber et al. 2004; Visser et al. 2012). X-rays may be more effective in destroying water, but only if the gas temperature is less than ~250 K (Stäuber et al. 2006; Notsu et al. 2021). Once the temperature is higher, water persists thanks to the rapid gas-phase reactions that drive oxygen back into water in regions shielded from high energy radiation (see also Fig. 16).

Which oxygen species are left as reservoirs? The lack of *Herschel*-HIFI O_2 detections from the hot core region in low- and high-mass protostars limits its contribution to less than a few %. CO_2 gas is also known to be a minor contributor, at least for high-mass protostars (van Dishoeck 1998; Boonman et al. 2003b). This leaves atomic O as the major unknown in hot cores, even though models expect any atomic O to be rapidly transformed into either H_2O or O_2 under dense warm conditions. There are currently no observations that can constrain the amount of atomic O in hot cores. The only alternative would be to have a large fraction of oxygen locked up in UDO which is apparently not vaporized or atomized above 100 K.

10.3. Shocks

Section 5 and Table 2 have shown that the abundances of H_2O in the different velocity components probed by *Herschel* are well below the expected value of $H_2O/H_2 = 4 \times 10^{-4}$. Even if enhanced due to UV radiation, OH is also not a major oxygen reservoir (Sect. 5.2). Is the bulk of the oxygen in warm outflows and shocks in atomic oxygen, if not in H_2O or OH? Irradiated shock models indeed predict that atomic oxygen may be a primary reservoir, although published results are for pre-shock densities of only 10^4 cm^{-3} (Godard et al. 2019). There are numerous low resolution spectra of the [O I] 63 and 145 μm lines taken toward protostars (e.g., Green et al. 2013; Watson et al. 2016; Mottram et al. 2017), but those data are generally used to determine mass outflow rates assuming an oxygen abundance with emission dominated by the jets (Nisini et al. 2015). Without spectrally and/or spatially resolved data, no independent atomic oxygen abundance can be derived.

Velocity-resolved observations of the [O I] 63 μm line with the GREAT instrument on SOFIA show that most of the [O I] emission in star-forming regions indeed originates in shocks (Leurini et al. 2015; Kristensen et al. 2017a; Gusdorf et al. 2017). However, for the NGC 1333 IRAS4A shock position R1, atomic oxygen accounts for only 15% of the oxygen budget in the high velocity hot gas. CO appears to be the dominant oxygen carrier at an abundance of $CO/H_2 \approx 2 \times 10^{-4}$; H_2O is a minor component, as is OH at this position (Kristensen et al. 2017a). For the distant high-mass source G5.89-0.39, Leurini et al. (2015) use spectrally resolved [O I] data to derive atomic oxygen column densities which could be as large as those of CO, or even larger depending on assumptions, but no hydrogen columns are available to quantify abundances. H_2O and OH are again minor components.

Thus, even in high temperature (shocked) gas, some significant fraction of oxygen may still be unaccounted for since it is also not observed in [O I]. Only in the very hottest gas could the

H_2O abundance approach the value required to contain most of the oxygen (Melnick et al. 2008; Neill et al. 2013). The important conclusion from this and related work (see Appendix G) is that this fraction of UDO must be locked up in a highly refractory form (such as refractory organic material) that is not vaporized or atomized even for shock velocities up to 50 km s^{-1} and temperatures up to several hundred K.

10.4. Oxygen budget from clouds to comets

Figure 32 summarizes the partionizing of oxygen between dust, gas and ice in the various regions discussed above. The adopted numbers are summarized in Table 3 with detailed references and motivation for choices presented in Appendix G. Uncertainties in each entry are difficult to quantify and are discussed in the appendix, but they are such that they do not change the overall picture.

Interestingly, the amount of unaccounted oxygen in the form of UDO is comparable between low-mass protostars, high-mass protostars and shocks at ~225 ppm, even though each individual UDO number is uncertain by ~50% and very different techniques and instruments have been used in all three cases, with a mix of emission and absorption lines involved. It is roughly double the amount of UDO compared with diffuse clouds, consistent with the finding that the amount of UDO increases with density (Jenkins 2009; Whittet 2010). The absolute amount of UDO depends in all cases strongly on the adopted overall [O] budget at 575 ppm; if the lower solar abundance of 490 ppm is used, the fraction of UDO may be halved but it does not disappear. In fact, Draine & Hensley (2020) argue for a higher ISM [O] abundance of 682 ppm with 66 ppm in UDO unaccounted for in diffuse clouds.

Table 3 and Fig. 32 include the oxygen reservoirs in comet 67P/Churyumov-Gerasimenko, which has been studied in exquisite detail by the Rosetta mission. Rubin et al. (2019) provide an overview of the abundances in volatiles measured by the ROSINA instrument, and those in refractory solids (dust) measured primarily by the COSIMA instrument. This table assumes an ice:dust mass ratio of 1:1. By definition, there is no room for UDO in these measurements. However, some fraction of oxygen is found to be in refractory organic material, about 9% or 50 ppm.

There has been some speculation that UDO could consist mostly of refractory organic material that is unobserved in diffuse and dense clouds (Whittet 2010). The measurements for comet 67P suggest that this component is not enough to explain all of the UDO in protostars and shocks. However, its amount is quite close to that found locked up in complex organic molecules in large chemical models of protostellar envelopes (Sect. 10.1). This suggests that the chemistry may proceed from the more volatile small organic molecules to larger more refractory species as material is exposed to higher temperatures and UV radiation "en route" from cloud to the comet-forming zones of disks (e.g., Greenberg & Hage 1990; Drozdovskaya et al. 2016).

For diffuse clouds, the measurement uncertainties are large enough that refractory organics of the type seen in comet 67P could be the major UDO reservoir, especially if the diffuse cloud numbers of Draine & Hensley (2020) are adopted.

In summary, the observations of protostars and shocks discussed in Sects. 5–9 indicate that a significant fraction of oxygen, of order 100–200 ppm, is not accounted for. This section provides possible solutions to this conundrum. In all cases, some small fraction of order 50 ppm may be in refractory organics, assuming that this fraction is similar in the ISM as in comets. For cold protostellar envelopes, an elegant solution for the remaining missing oxygen is that ice columns are much larger than assumed because grains have grown to larger sizes suppressing the ice features. For hot cores and shocks, this solution does not work since the water ice in large grains should have been sublimated or sputtered so the situation is more puzzling. If gaseous atomic oxygen is indeed negligible, then the oxygen must be in some refractory form that does not vaporize or atomize, even in strong shocks up to 1000 K.

Two sets of observations are urgently needed. First, more measurements of velocity resolved atomic oxygen lines (both [O I] 63 and 145 μm) in protostars and shocks can quantify its contribution in more sources. The current numbers hinge on just a couple of heterodyne [O I] spectra. Only the upGREAT instrument on SOFIA is capable of such measurements (Risacher et al. 2018).

Second, deep observations of mid-infrared lines of H_2O and H_2 probing the hottest gas in shocks are warranted to determine whether the UDO material is vaporized at $T > 1000$ K and the H_2O abundance starts to approach $H_2O/H_2 = 4 \times 10^{-4}$. So far, only the data for NGC 2071 and Orion-KL point in this direction (Sect. 5). This will be possible with the JWST-MIRI instrument (Wright et al. 2015) at shock positions offset from the protostar to avoid large extinctions. The simultaneous measurement of H_2 and other atomic and molecular lines should provide better constraints on shock density, which is one of the largest uncertainties in the analysis.

11. Discussion

Based on the detailed analyses for individual physical components and evolutionary stages, we can now come back to the three questions that WISH aimed to address (Sect. 1), as well as the two axes of WISH: from low- to high mass, including implications for extragalactic water observations, and the evolution of water from cloud to disk. The focus is on *Herschel*'s contributions to these questions. Finally some current and future opportunities for observing water will be summarized together with lessons for future far-infrared missions.

11.1. How and where water is formed in space

Herschel observations, in particular the velocity-resolved HIFI data, have allowed the main chemical processes leading to water in star- and planet forming regions to be identified and quantified (Fig. 33). Of the three routes illustrated in Fig. 4, the water chemistry in star-forming regions is clearly controlled by a close coupling between the gas and ice phases. Water ice builds up in the cold dilute phase with some gaseous water vapor produced by ion-molecule reactions and destroyed by UV photodissociation. In cold dense cores, the bulk of the water ice has formed, with a small fraction released into the gas by nonthermal processes such as photodesorption (see Sects. 6 and 7 for more details). The new *Herschel* observations have highlighted the importance of cosmic-ray induced photodesorption deep inside clouds. Also, the multilayer nature of ice formation is key to interpreting data on deuterated water.

Once the protostar turns on, heating occurs both actively through shocks and winds associated with the outflows and passively by warming up the dust and gas in the surrounding envelope through the protostellar luminosity. Shocks can sputter ices and produce copious water vapor through high-temperature

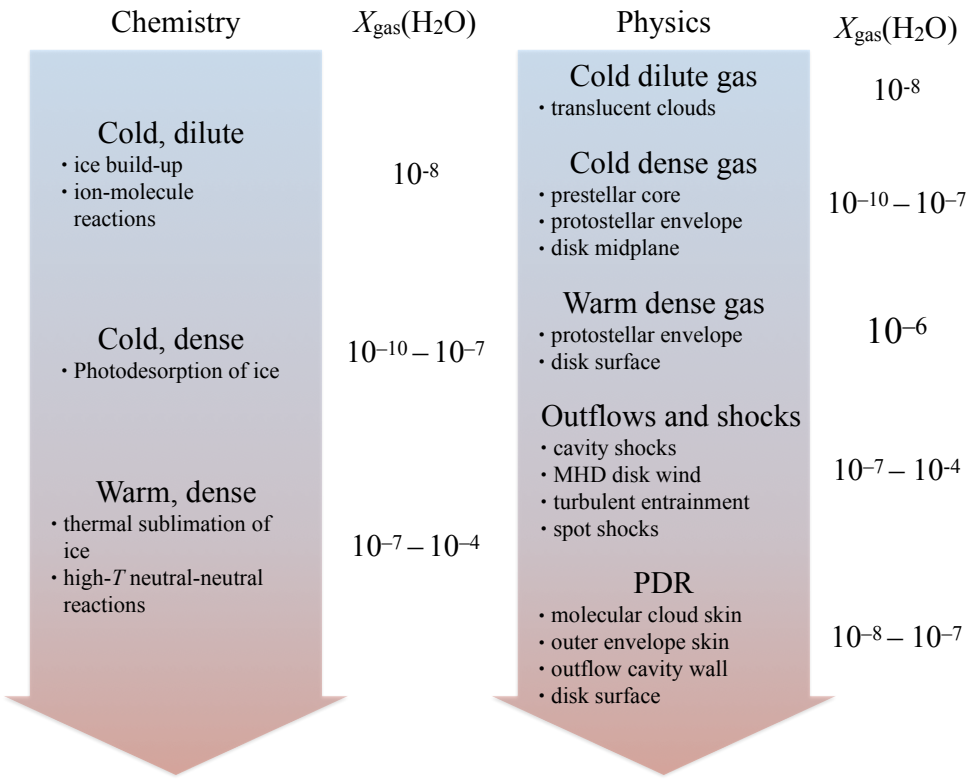

Fig. 33. Physical components dominating water emission with evolutionary stage (*right*) and principal chemical processes at each temperature regime (*left*). Typical water abundances with respect to H_2 associated with each evolutionary or temperature regime are indicated.

gas-phase reactions: the *Herschel* data provide evidence that both processes are taking place with high temperature gas-phase chemistry dominating at the high velocities. Envelope heating results in water ice sublimation at its iceline around 100 K. Once the star has formed, it emits strong UV radiation setting up a PDR on the neighboring cloud, envelope or disk surface. X-rays may also play a role in destroying water in the inner envelope and hot core. Figure 33 (left) summarizes the chemical processes, whereas Sect. 11.3 discusses the abundances.

11.2. Physical components traced by water vapor

11.2.1. Water

Table 1, Figs. 2 and 10 summarize the main water vapor line characteristics at each of the physical stages, for low and high-mass sources. Water vapor in cold low-density gas is primarily seen in narrow (~1 km s^{-1}) absorption lines against a bright far-infrared continuum. Narrow emission lines are seen only in cold high density quiescent gas such as those found in pre-stellar cores, in PDRs, and in the outer parts of protoplanetary disks near the midplane. Relatively narrow water emission lines (a few km s^{-1}) originate in warm, dense gas in protostellar envelopes (isotopologs, away from outflows).

The water vapor emission seen by *Herschel* is, in contrast, mostly in broad lines associated with various types of kinetic heating (cavity shocks, disk winds, turbulent entrainment) and medium-broad offset lines (spot shocks). Regions of strong water vapor emission are generally compact, with an extent comparable to or less than one *Herschel* beam ($\lesssim$20″, Sect. 4.1). Even within this beam, the emitting sizes are generally small, of order 100 au for low-mass protostars.

Three possible heating mechanisms are suggested for the broad warm component involving kinetic energy dissipation (component 1, Sect. 4.3, Fig. 34). First, cavity shocks heat and compress the envelope along the cavity walls via non-dissociative, 15–20 km s^{-1}, *C*-type shocks (Mottram et al. 2014). Second, dusty MHD disk winds (Yvart et al. 2016) launch dense gas from the inner disk at 0.2 out to 5–20 au, with heating taking place via ion-neutral drift in the accelerating flow. This results in a broad range of outflow velocities, spanning a few to 80 km s^{-1}. Finally, turbulent entrainment heats gas within a mixing layer flowing between the wide-angle protostellar wind and the infalling envelope (Liang et al. 2020) and also provides a natural explanation for broad line profiles peaking at systemic velocity. In addition, the mixing-layer model allows for a static outflow cavity that does not expand beyond observed sizes over the typical Class 0 phase duration. It is possible that all three mechanisms operate simultaneously. Spatially resolved observations of the warm dense gas together with mid-infrared searches for shock tracers (e.g., atomic lines of Fe, S or Si) will be required to determine which dominates.

Overall, the conclusion from the *Herschel* data is that water emission is a highly sensitive probe of the physics of different star-formation phases with unique absorption or emission line characteristics that are not easily seen by any other molecule. Viewed from a more global perspective: strong water emission with large line luminosities clearly points to active star-formation sites.

11.2.2. Other molecules

Herschel has also provided insight into the physical components traced by other molecules and their lines, with a summary

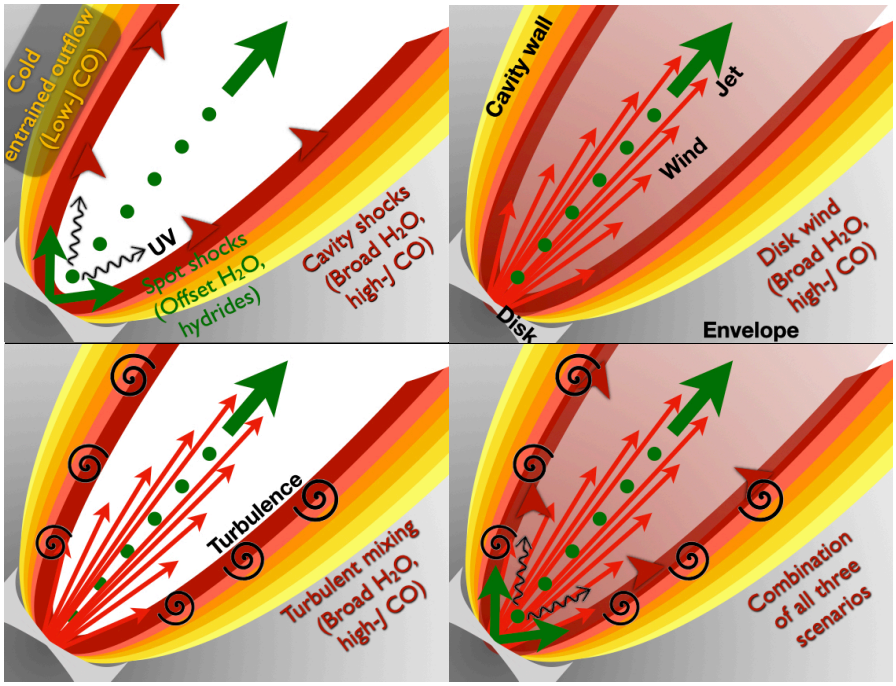

Fig. 34. Cartoon illustrating in which physical components most of the H_2O, CO and other molecular line emission originates for the different scenarios presented in the text. These include the outflow cavity shocks and spot shocks (*top left*), the disk wind (*top right*), the turbulent entrainment (*bottom left*), or a combination of the three (*bottom right*). Each panel shows the jet with bullets (green), the outflow cavity wall (red/yellow gradient), disk and envelope (gray-scale). Arrows are meant to indicate gas motion.

provided in Fig. 34 (see also Fig. 8 in San José-García et al. 2016 and Fig. 5 in Mottram et al. 2014). High-J CO lines with $J_{up} \geq 14$ trace the same regions as water. In contrast, the low-J CO lines probe the entrained outflow gas physically separated from the actively heated and shocked material.

OH shows broad line profiles consistent with those of H_2O and thus probes the same components (Sect. 5.2). Its abundance is enhanced because the warm gas is exposed to UV radiation dissociating H_2O into OH and changing the overall shock structure. Hydrides such as OH^+, H_2O^+ and CH^+ have narrower lines (but not as narrow as those of CH) and originate primarily in the UV irradiated outflow cavity walls and spot shocks (Benz et al. 2016).

Other molecules that are abundant in ices, such as NH_3 and CH_3OH, mostly trace the hot core region and the low-velocity part of the shock. HCO^+, whose abundance anticorrelates with that of H_2O, largely avoids the outflow region. SiO can trace the fast EHV part of the shock similar to H_2O, but its abundance and line profiles show a more rapid evolution across sources than that of H_2O.

11.2.3. Cooling budget

Water lines are a significant coolant of gas in warm gas, but not dominant. For low-mass Class 0 and I sources, water contributes typically at the 20% level, whereas CO does so at 30–45% of the total far-infrared line cooling. The remainder of the far-infrared cooling budget is provided by OH and [O I]. For high mass sources, CO becomes more important, up to 70% of total, whereas the contribution from water lines drops because more water lines occur in absorption rather than emission.

Significant gas cooling is also provided by the H_2 mid-infrared lines (Maret et al. 2009). These are not considered here but will be further quantified by future JWST observations.

11.3. Typical water abundances in each physical component

Figure 33 summarizes the typical water vapor abundances inferred for each of the physical components. Only average order of magnitude values for each type of source are given, with details described in Sects. 5–9. For individual sources, abundances are accurate to typically a factor of a few or better.

This figure illustrates that the gaseous water abundance varies significantly and is thus a good diagnostic of different physical regimes. However, it never reaches the maximum abundance of $H_2O/H_2 \approx 4 \times 10^{-4}$ expected if all volatile oxygen is driven into water. Only the warmest gas has abundances approaching 10^{-4}, but in most cases the gas components probed by *Herschel* have abundances of 10^{-7}–10^{-6} with respect to hydrogen.

In cold gas, water is mostly frozen out as ice so water vapor abundances are very low, down to 10^{-10}. Interestingly, the most accurate constraints on water abundance profiles have been made for cold cores or outer protostellar envelopes, where the velocity profile permits reconstruction of the water abundance as a function of position (see Sect. 7.1). At the edge of the core, H_2O gas is produced by photodesorption of water ice at an abundance of $\sim 10^{-7}$; deeper into the core it drops to less than 10^{-10}. The same holds for protoplanetary disks, but then in the vertical direction: water vapor is UV photodesorbed in layers at intermediate heights, dropping to very low abundances near the midplane.

11.4. Water: from low to high mass

Section 4, together with Figs. 2 and 10 and Table 1, demonstrate the large similarity in water line profiles from low- to high-mass YSOs. As summarized in San José-García et al. (2016), the profiles can be decomposed in similar physical components associated with kinetically-heated gas (warm outflows and shocks) and warm dense envelopes, but with the relative contribution from the envelope increasing from low- to high mass (see Appendix C). The same physical components can also be seen in high-J CO lines, but only for $J_{up} > 14$. Even then, they are less prominent than in water lines. The similarity in profiles means that common physical mechanisms are at work in the outflows of sources across more than five orders of magnitude in luminosity and that the gas cooling structure appears universal. The water lines probed by *Herschel* and the high-J CO emission are always

dominated by material at similar conditions: temperatures of a few hundred K and densities from 10^5–10^8 cm^{-3}.

The water line luminosities show a strong, near-linear correlation with bolometric luminosities of the sources, $L_{\rm bol}$. For optically thick, but effectively optically thin lines such as those of water, this empirical relation simply implies that there is more gas at the required conditions for more luminous sources: material is heated further from the source and deeper into the cavity wall. This is consistent with the larger emitting areas found for high mass sources from the water radiative transfer analysis compared with that for their lower mass counterparts (few thousand au versus 100 au).

Overall, the intensity ratios of the various water lines probed by *Herschel*-HIFI are also very similar across the luminosity range (and even as function of velocity, modulo absorption features), pointing to the similar physical conditions inferred above. Surprisingly, however, one line ratio stands out: the 752 GHz 2_{11}–2_{02}/988 GHz 2_{02}–1_{11} ratio is generally less than 1 for a wide range of sources, but lies above 1 for high-mass protostars (San José-García et al. 2016). One possible explanation is that radiative pumping plays a more significant role for higher-mass protostars than for their lower- and intermediate-mass counterparts. Alternatively, absorption in the 988 GHz line affects the line ratio in high-mass sources (van der Tak et al. 2019). In many aspects, the intermediate mass sources look more similar to low-mass protostars, or an unresolved cluster of low-mass protostars within the *Herschel* beam, than a scaled-down version of high-mass sources.

The water abundances in the various physical components are also found to be similar across the luminosity range. Inner and outer envelope water abundances, when analyzed in a similar manner, show a comparable range of values (Fig. 21). Water abundances in warm outflowing gas are low by at least two orders of magnitude due to UV irradiation in all sources, although there is some debate to what degree shocks associated with high-mass sources have even lower abundances than their low-mass counterparts due to more intense UV (Table 2).

11.5. Implications for extragalactic water observations

The inferred linear relations of line luminosity with bolometric luminosity for Galactic protostars hold over many more orders of magnitude when observations of extragalactic sources from Yang et al. (2013) are included, both for water and for mid- to high-J CO lines (San José-García et al. 2013, 2016). Figure 35 shows an updated version of this correlation for the 988 GHz line including the low-mass sources from the WILL survey (Mottram et al. 2017) and low- to intermediate-mass sources in the Cygnus star-forming cloud (San José-García 2015). This strong relation with FIR emission has been interpreted differently by the two communities, however (Kristensen & Bergin 2021). In Galactic sources, it is well known from the *Herschel* data that water and high-J CO are associated with shocked gas where the lines are collisionally excited (e.g., Mottram et al. 2014). The emission is spatially compact, not extended over entire molecular cloud scales (Sect. 4.1). In fact, away from the immediate surroundings of protostars and their outflows, the water emission and abundance drops steeply, within a single *Herschel* beam for high-mass sources ($\lesssim$0.1 pc) (Jacq et al. 2016; van der Tak et al. 2019). PDRs do not contribute significantly on cloud scales (Melnick et al. 2020). The far-infrared luminosity in this interpretation traces the material in which stars are currently forming (the protostellar envelopes), but this infrared radiation does not affect the water excitation: there is no direct causal relation.

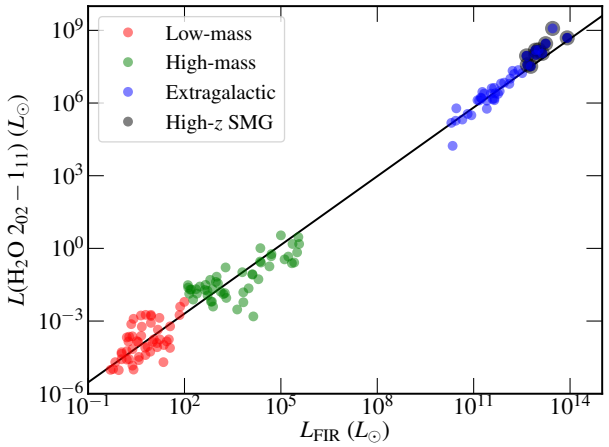

Fig. 35. Line luminosity of the H_2O 2_{02}–1_{11} transition at 988 GHz versus the FIR luminosity for low- and high-mass sources and extragalactic sources. The gray line is the best-fit power-law function, with an index of 0.95 ± 0.02.

In contrast, the extragalactic community uses the tight correlation between the H_2O line luminosity and FIR luminosity to infer that the water excitation is dominated by FIR pumping, as opposed to collisional excitation in outflows. In the extragalactic scenario, water emission thus originates in the entire molecular cloud in which stars form, and is not directly associated and co-located with star formation (e.g., van der Werf et al. 2011; González-Alfonso et al. 2014; Yang et al. 2016; Liu et al. 2017; Jarugula et al. 2019).

As shown by Kristensen & Bergin (2021), the low- and mid-J water line ratios ($E_{\rm up}$ < 300 K) do not change significantly between Galactic and extragalactic sources. Most notably, the peculiar 752/988 GHz line ratio found for high-mass sources is not found for extragalactic sources (Yang et al. 2013; San José-García et al. 2016). Thus, the baseline interpretation is that the same mechanism that is responsible for water emission in Galactic sources also holds for extragalactic sources: water emission arises in outflows and shocks associated with (clusters of) currently forming stars. Thus, any water line that does not suffer significant self-absorption is a good and clean tracer of buried star formation activity.

By inference, the same interpretation would hold for mid- to high-J CO lines. For high $J_{\rm up} \geq 14$, there is an observed close relation between CO and water lines with both tracing currently active outflow heating (Sects. 4.1 and 4.3). For mid-J CO lines there can also be a contribution from the warm envelope. For example, for ^{12}CO $J = 10$–9, the fraction of envelope emission is around 50% for high-mass sources (San José-García et al. 2016). Since envelope emission also traces current star formation, it does not necessarily affect the interpretation, albeit that there could be extra scatter due to the variation in outflow versus envelope contribution for each source.

Is all water emission associated with current star formation activity? A subset of extragalactic sources are known to drive outflows on much larger galaxy scales, often seen perpendicular to the galactic disk where they can escape freely. The jets and flows are thought to be driven by Active Galactive Nuclei (AGN) buried in the center of the galaxy (see Blandford et al. 2019, for a review). These large galaxy-scale outflows are well traced by OH lines, not by H_2O lines, observed by *Herschel*-PACS (Sturm et al. 2011; González-Alfonso et al. 2017). OH is much more abundant than H_2O due to the intense UV radiation in the outflows and

cavity walls away from the shielded regions. Thus, H_2O is the better probe of star formation activity whereas OH may be the better probe of AGN activity.

A big advantage of extragalactic observations is that even for small redshifts, the water lines shift into frequency ranges that are not obscured by the Earth's atmosphere and can be well observed from the ground. ALMA is already providing a rich database on water lines in extragalactic sources and will continue to do so in the coming decades. The *Herschel* mission studying water in Galactic star-forming regions was needed to properly interpret these ALMA observations, thereby revealing the physical origin of emission. The next step will be to calibrate water emission with measured star-formation rates on galactic scales, such that water emission can be used to quantify star-formation rates in distant high-redshift galaxies.

11.6. Water: from cores to disks

The third goal of the WISH+ program was to follow the trail of water from its formation in molecular clouds to the sites where new planets are formed. Addressing this question requires observations of both water vapor and water ice using a wide range of instruments. The broader picture of water from clouds to planets is reviewed elsewhere (van Dishoeck et al. 2014; Hartmann et al. 2017; Morbidelli et al. 2018). Here the unique contributions that *Herschel* has made are highlighted, in concert with recent millimeter interferometry (ALMA, NOEMA) results for warm water.

11.6.1. Molecular clouds: water ice formation

Herschel-HIFI data of cold clouds and outer protostellar envelopes coupled with detailed chemistry and radiative transfer modeling have demonstrated that most water is formed as ice in the early stages of cloud evolution (Sects. 6 and 7). This is consistent with direct observations of water ice at infrared wavelengths in quiescent and star-forming clouds. *Herschel* studies, most notably those as part of WISH, have demonstrated a good quantitative understanding of the cold water chemistry and ice formation in the pre-stellar stage. The amount of water ice that can be produced at subsequent warmer protostellar stages is only a small fraction of the total ice.

It is likely that a significant fraction of available volatile oxygen (i.e, not locked up in silicates) is contained in water ice in cold clouds. The fact that not all of this ice is detected in infrared absorption spectra either points to a short pre-stellar stage, or to a small fraction of grains that have grown to at least micrometer size by the dense cloud stage. Some ill-determined fraction of oxygen is contained in other forms, either in volatile O-containing species or more refractory material called UDO (Sect. 10). While the UDO fraction may change with evolutionary stage, it is not expected to affect the bulk of the water trail.

How much water ice is made in dense clouds? A typical 1 $M_\odot$ cloud forms about 6×10^{52} water molecules assuming a water ice abundance of 10^{-4} with respect to H_2, over a period of about 10^6 yr. This amounts to more than 1 million oceans of water available for new planetary systems that are formed in the cloud (1 Earth ocean = 1.5×10^{24} gr of water = 5×10^{46} water molecules). This large number of "oceans" implies that a significant water reservoir is available to be supplied. However, there are a number of overall loss factors, both in the supply to the natal disk and then to a nascent planet (see below). Thus this number should not be taken to imply a direct link to Earth's water (e.g., van Dishoeck et al. 2014).

11.6.2. Protostars: rapid water production in outflows and shocks but lost to space

Herschel data have confirmed the rapid production of water in warm kinetically heated gas associated with protostellar outflows and winds and their impact on the surrounding envelope. Using the observed mass outflow rates and water abundances, of order 1–5 oceans of water vapor per year can be produced in a single low-mass outflow over the period of the lifetime of the embedded phase, which is about 10^5 yr (Kristensen & Dunham 2018). Thus, the amount of water molecules formed in outflows per year is comparable to that in cold clouds. However, all of this water is carried away by the outflows and thus lost to space. There water is either photodissociated or frozen out back onto the grains as ice (Bergin et al. 1998).

11.6.3. From clouds to disks: inheritance versus reset

The transport and survival of water ice from the collapsing core onto the forming disk is a crucial step in the water trail. How and where material falls into the disk and with what speed is still poorly understood and ill constrained observationally. Directly linked to this question is the extent to which the chemical composition is preserved from cloud to disk ("inheritance"), or whether it will be modified en route ("reset") due to the changing temperatures and UV radiation along the infall paths (e.g., Visser et al. 2009; Hincelin et al. 2013; Drozdovskaya et al. 2016). In the most extreme case of strong accretion shocks, reset implies complete vaporization of all molecules and dust grains back to atoms, with subsequent reformation; milder versions of reset include sputtering of ices, and gas and ice chemistry modifying abundances.

To test the inheritance versus reset scenarios, key observational diagnostics of these processes are needed. There is some observational evidence for chemical changes near the centrifugal barrier in the form of strong SO and SO_2 emission (e.g., Sakai et al. 2014; Artur de la Villarmois et al. 2019), but implied temperatures are low, ~50 K, and their origin and implications for any shock are still unclear.

The results for young disks found in Sect. 9.1 argue for significant inheritance of water ice since no water vapor, warm or cold, is observed to be associated with young disks in the Class I phase, as would be expected when accretion shocks onto the disk would sputter the ices or produce abundant water gas. Also, a water-vapor rich warm envelope is ruled out by the current *Herschel* and ALMA+NOEMA data, although deeper and higher spatial resolution ALMA data could put up to an order of magnitude stronger constraints on any warm water produced by accretion shocks. Even the disks themselves are cold enough by the Class I stage that they have very low water vapor abundances in the outer disk and surface layers, suggesting that the bulk of the water is locked up as ices onto grains at an early stage of disk formation.

Models by Visser et al. (2009) and Furuya et al. (2017) that follow the water chemistry along many infall trajectories have found that most water in disks is indeed inherited as ice. A small fraction may be sublimated during a luminosity burst of the young (proto)star moving the water ice-line outward, as often happens in the Class 0 and I phases, but this water ice quickly refreezes again without chemical alteration (Taquet et al. 2016).

Only trajectories that come close to the outflow cavity wall result in water dissociation due to exposure to UV radiation or X-rays.

11.6.4. Disk evolution and transport

Figure 25 provides a useful framework to illustrate the different water reservoirs in disks. *Herschel* has shown that gas and dust evolution as well as dynamics can alter this simple picture, as discussed in Sect. 9.2. Once in the disk, the icy grains can grow further and settle to the midplane (Krijt et al. 2016). There is observational evidence based on the spectral index at mm wavelengths, as well the required dust opacity for hiding lines in the inner disk, that grains have already grown to mm or cm size in disks during the embedded phase (e.g., Kwon et al. 2009; Testi et al. 2014; Harsono et al. 2018). These large icy grains will drift inward or be trapped in pressure bumps where they can grow further to water-rich planetesimals (e.g., Raymond & Izidoro 2017; Schoonenberg & Ormel 2017). The *Herschel*-HIFI data of disks indicate that water vapor likely follows the large icy dust grains that have settled and drifted inward.

Once the drifting icy pebbles cross the ice line, they will release their water into the gas resulting in an inner disk that is rich in water vapor, with abundances that can even exceed the canonical value of 10^{-4} by more than two orders of magnitude within 1 Myr (Ciesla & Cuzzi 2006; Bosman et al. 2018a). Accretion onto the star will however remove this oxygen-rich gas and there is some disagreement on the relative importance of replenishment versus removal. If removal dominates, it may drain the inner disk of water-rich gas in as little as 0.1 Myr (Ali-Dib et al. 2014). Tracing the water vapor in this inner disk requires mid-infrared observations. *Spitzer* data have indeed provided evidence for both high and low water abundances in the inner disk linked to dust disk size and structures (e.g., Banzatti et al. 2017, 2020) (see Sect. 9.2.2).

What do the HIFI data imply for the availability of water in new planetary systems? The HIFI detection of gaseous H_2O in the TW Hya disk implies a reservoir of water ice of a few thousand oceans, which suggests plenty of water to build a habitable planet such as Earth. However, it is unclear whether all of this water can reach the habitable zone close to the star. The formation of a single Jupiter-like planet in a disk could lock up the bulk of this available oxygen reservoir. Also the flow of icy pebbles from outer to inner disk can be stopped at a dust trap outside the ice line. Indeed, the inner TW Hya disk is known to be poor in oxygen and carbon, likely due to a dust trap outside of 20 au locking up CO and one at 2.4 au locking up H_2O (Zhang et al. 2013; Schwarz et al. 2016; Bosman & Banzatti 2019; McClure et al. 2020) (see also Sect. 9.2.2). In such cases, scattering of ice-rich planetesimals from the outer to the inner disk could happen only at later evolutionary stages when the gas has disappeared, and in that way deliver water to forming terrestrial planets in the habitable zone (Morbidelli et al. 2012).

11.6.5. Deuteration as a probe of water inheritance

An alternative way to probe water ice processing en route from cloud to disk is ice deuteration, which is particularly sensitive to physical parameters (Ceccarelli et al. 2014): if most water ice is inherited, the HDO/H_2O ice ratio set in the cold pre-stellar stage should be preserved in subsequent stages. The situation is however not as simple as initially thought because the layered structure of ices needs to be taken into account. Also, HDO has not yet been detected in mature Class II disks.

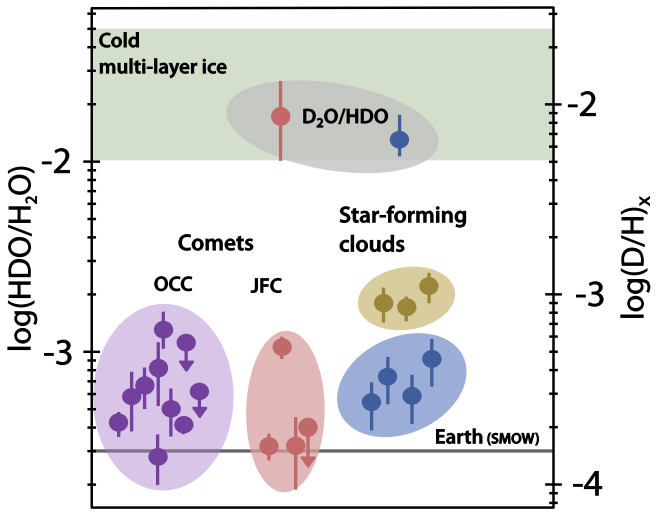

Fig. 36. HDO/H_2O (lower points) and D_2O/HDO (two top points) abundance ratios measured for warm gas in low-mass protostellar regions and in comets (JFC = Jupiter Family Comets; OCC = Oort Cloud Comets). The HDO/H_2O data are taken from the summary in Jensen et al. (2019) (brown: isolated protostars; blue: protostars in clustered regions), the D_2O/HDO star-forming cloud ratio from Coutens et al. (2014) and the HDO/H_2O and D_2O/HDO ratios in comet 67P (JFC high points) from Altwegg et al. (2017). The much higher HDO/H_2O ratios found in the top layers of multilayer ice models are indicated with the light green zone and are similar to the HDO/H_2O values of 0.025 measured with *Herschel*-HIFI in cold outer envelope gas.

Ice formation models that include a multilayer structure have shown two stages: the initial cloud formation stage in which most of the H_2O ice is formed, and the later dense core phase in which the bulk of the HDO and D_2O ice are made, with only little additional H_2O ice (Taquet et al. 2014; Furuya et al. 2016) (Fig. 5). A typical grain of ~0.1 μm has nearly 100 ice layers if all oxygen is converted to ices. The bottom 75–95% of those layers have HDO/H_2O around 10^{-4} whereas the top 25–5% have HDO/H_2O as high as 10^{-2}–10^{-1} (Fig. 24). This results in overall bulk HDO/H_2O ice ratios of ~10^{-3} within a factor of two (Taquet et al. 2014; Furuya et al. 2016). A characteristic feature of this cold, layered ice chemistry is that doubly deuterated water is even more enhanced: the bulk D_2O/HDO$\gg$ bulk HDO/H_2O by about a factor of 10 (Fig. 24).

What do the *Herschel* and new NOEMA+ALMA mm interferometry data tell us? Figure 36 summarizes the observational results for protostellar envelopes compared with comets, using data summarized in Jensen et al. (2019). First, the derived high gaseous HDO/H_2O of 0.025 in the cold outer core (Sect. 7.3) from the HIFI data is entirely consistent with the multilayer ice formation (green shaded area), and is much higher than the values found in hot cores. The high value reflects both the fact that only the top, deuterium-enriched ice layers are photodesorbed, with low-temperature ion-molecule chemistry further enhancing the deuteration (Fig. 24) (Furuya et al. 2016). Also, Coutens et al. (2013b) found D_2O/HDO > HDO/H_2O in the cold outer layers of the IRAS16293-2422 core from *Herschel*-HIFI D_2O, HDO and $H_2^{18}O$ lines consistent with the models.

Second, the "hot core" HDO/H_2O abundances of $(0.5–1)\times10^{-3}$ (Sect. 8), which presumably represent thermally sublimated ices, are consistent with the bulk ice deuteration found in models of the cold pre-stellar phase (Fig. 24). They also cover the same range as the cometary data shown in Fig. 36. The three brown HDO/H_2O ratios for star-forming clouds that

lie somewhat higher in this figure refer to isolated cores that are generally somewhat colder than the clustered regions (Jensen et al. 2019). Since our Solar System is thought to be born in a cluster (Adams 2010), the lower blue points are more appropriate for comparison with comets.

The "smoking gun" for the inheritance scenario comes from the observed high abundance of D_2O, with $D_2O/HDO \approx 7$ HDO/H_2O for the NGC 1333 IRAS2A hot core (Coutens et al. 2014). Similarly, the detection of D_2O in comet 67P/Churyumov Gerasimenko provides an important clue (Altwegg et al. 2017). The inferred D_2O/HDO ratio for 67P is a factor of 17 higher than the HDO/H_2O ratio. Both values (high points in Fig. 36) are consistent with pre-stellar multilayer water ice formation and not with water reformed in the outer part of the solar nebula disk.

Could the deuteration fractions actually be modified en route from cloud to disks or be established within disks? The delivery of layered ice mantles from cloud to disk has been investigated by Furuya et al. (2017). These models confirm that the majority of pre-stellar water ice is retained upon delivery to the disk without significant UV processing and ice sublimation. The HDO/H_2O ratio is somewhat lowered (by up to a factor of two) because of selective loss of the upper ice layers but is largely retained when averaged over the entire disk, as is D_2O/HDO. Locally, the HDO/H_2O can deviate more from the original value, especially in the upper layers of the outer disk.

How can this inheritance case be distinguished from the full reset case in disks? Cleeves et al. (2014) show that starting from the elemental [D]/[H] ratio, mature Class II disks cannot produce enough HDO to explain the measured level of water deuteration in comets of $HDO/H_2O \approx (0.5-1)\times10^{-3}$ (see also Willacy & Woods 2009), a conclusion that is strengthened if cosmic rays are excluded from disks by stellar winds. There have been some claims that disk models with vertical turbulent mixing can reach the required HDO/H_2O levels (Furuya et al. 2013; Albertsson et al. 2014), but the recent observational limits on turbulent mixing (e.g., Flaherty et al. 2018, 2020; Teague et al. 2018) make those models less realistic.

In any case, there would be two clear ways to distinguish the inheritance and reset models: (i) in situ disk chemistry models predict an increasing HDO/H_2O ratio with radius due to the decreasing temperature profile, whereas this is not always the case for the inheritance models; (ii) reformed ices in the disk have $D_2O/HDO \sim 0.1\times HDO/H_2O$ whereas the original pre-stellar ices have $\sim10\times$ HDO/H_2O (Furuya et al. 2017).

Although the results for D_2O/HDO hinge on only one protostar and one comet observed so far, the HDO/H_2O ratios as well as the models discussed above point to the same conclusion. Further observations of D_2O in protostellar sources should have high priority, and new ALMA data indeed strengthen the inheritance case (Jensen et al. 2021).

In conclusion, several lines of observational and modeling evidence on deuterated water, together with the results for young disks (Sect. 9.1), point toward the bulk of the water being formed in the cold pre-stellar stage and incorporated largely unaltered into disks and comets, where they are locked up quickly into larger grains and planetesimals.

11.7. Lessons for future missions

A general lesson from WISH+ is that most of the new science comes from the deepest and longest integrations, either to detect weak lines or to get high signal-to-noise on strong line profiles, pushing the instruments to the limits. For WISH, such long integrations were possible to plan because of the freedom that the GTO time offers. In contrast, time allocation committees, in particular on Galactic science, are often reluctant to grant significant time per source. Future missions should allow for a mechanism for deep integrations on Galactic sources early in the mission.

The importance of future mid- and far-infrared observations and millimeter interferometry to trace water has been highlighted near the end of each of the sections, Sects. 5–10. Summarized per facility or instrument, each has its strength in providing (part of the) answers on the water trail from cloud to disk. In fact, it is clear from the discussions in Sects. 5–10 that the full picture can only be pieced together by the combination of many different observations, with the far-infrared wavelength range providing a central role. Roughly in order of when instruments become available, the opportunities for adding to our understanding of water are as follows.

– Millimeter interferometers, most notably ALMA, will be very powerful to image warm water on subarcsec scales (<30 au radius in nearby star-forming clouds) in large numbers of hot cores and (young) disks through the $H_2^{18}O$ 203 and 390 GHz and various HDO and D_2O lines. Mm arrays can observe optically thin water isotopologs at low frequencies at which the dust continuum emission is optically thin, in contrast with space-based data at high frequencies. So far, ALMA has observed just a few sources; large surveys are needed. ALMA can also put constraints on water released or produced at the accretion shock. By observing HDO and D_2O in the same beam, direct and model-independent probes of HDO/H_2O and D_2O/HDO in warm gas are obtained. For outflow shocks, higher excitation (nonmasing) $H_2^{16}O$ lines that are not obscured by the atmosphere can be imaged.

– The VLT-CRIRES+ and SOFIA-EXES high-resolution $R \approx 10^5$ near- to mid-infrared spectrometers are well suited to observe hot water absorption lines at 3 and 6 μm arising in the inner envelope or outflow toward protostars. By spectrally resolving the lines, both the origin as well as accurate optical depths and thus column densities can be determined.

– VLT-CRIRES+ and Keck-NIRSPEC, and in the future ELT-METIS (planned ~2028), can also spectrally resolve H_2O vibration-rotation emission lines at 3 μm in disks at $R \approx 10^5$ and constrain their location through systematic velocity patterns. Moreover, ELT-METIS can spatially resolve the lines down to a few au and distinguish a disk surface layer versus disk wind origin. These 3 μm vibration-rotation lines are also bright in comets, and provide an accurate way to determine cometary HDO/H_2O when combined with near-simultaneous observations of HDO.

Individual mid-infrared lines in the 10 μm region can be targeted with VLT-VISIR at $R \approx 10^4$ in bright sources; higher resolution instruments such as TEXES on Gemini are only offered sporadically. ELT-METIS will offer high spatial resolution at N-band, but with a spectral resolving power of only a few hundred, limiting the line-to-continuum ratio.

– The SOFIA-GREAT instrument is unique in observations of spectrally resolved lines above 1 THz, most notably of the [O I] 63 and 145 μm lines. Such observations will be of crucial importance to nail down the oxygen budget in shocks and other warm regions. OH, NH_3 and high-J CO can also be observed, albeit with reduced sensitivity compared with *Herschel*. SOFIA-4GREAT now also allows observations of the $H_2^{18}O$ ortho-ground state line in bright sources, including comets. Also, velocity resolved [C II] line mapping as a tracer of UV radiation on molecular cloud scale is possible with SOFIA-UPGREAT.

– The JWST-MIRI instrument will probe hot and warm water abundances in shocks and inner disk surface layers, through the 6 μm vibration-rotation band and the pure rotational lines at >10 μm. For disks, this combination of lines will allow more accurate assessments whether the inner regions inside the ice line are enhanced or depleted in water. For shocks, the combination of observed H_2O and H_2 lines will be key to determine whether water accounts for the full oxygen budget in hot gas, or whether any UDO is still required. JWST-NIRSPEC can probe the hottest water emission at 3 μm, as well as the primary H_2O, HDO and CO_2 ice absorption bands at 3–5 μm, even spatially resolved on 10–20 au scales.

– The approved SPHEREx mission with a launch date around 2024 will obtain low resolution absorption spectra at 0.75–5 μm toward $>10^6$ lines of sight with strong background sources and thus measure H_2O ice and other oxygen-containing ices such as CO_2, OCN^-, CO, and OCS along the lines of sight, further testing and quantifying ice formation and ice chemistry models.

– Future far-infrared missions such as the proposed Origins Space Telescope and the proposed but recently cancelled SPICA mission are particularly well suited to trace the water trail by observing a very wide range of mid- and far-infrared water lines (Fig. 1), covering both hot (1000 K), warm (~200 K), and cold (~30 K) gas with a resolving power of up to 3×10^5 for Origins. This includes the critical 179 μm line connecting with the ground state. For protostellar envelopes and shocks, the analysis would have to take into account that there are likely multiple physical components (as found by WISH) that are not spectrally resolved. Also, the flux of low-lying water lines and [O I] may be significantly affected by absorption.

For disks, far-infrared missions would be a very powerful tool to locate the water snowline and quantify the water vapor in the different disk water reservoirs in statistically significant samples of disks. Indeed, models show that the largest sensitivity to the location of the snow line is provided by lines in the 40–60 μm region, which is exactly the wavelength range without recent observational facilities. Moreover, the 44 and 62 μm (crystalline) water ice features can be observed in emission, allowing to quantify the bulk of the water and oxygen in the emitting layer at intermediate disk heights. In the current design Origins is four orders of magnitude more sensitive to the mass of cold water vapor emission in disks compared to *Herschel*. Observing a thousand disk systems across the range of stellar masses will enable meaningful comparison to the exoplanet composition and inventory.

None of these planned space missions include a THz heterodyne capability. Only the Russian-led Millimetron proposal has such an instrument in its baseline plan, whereas the Origins-HERO instrument is an upscope option. This lack of heterodyne facility will strongly limit studies of cold quiescent water gas in clouds and outer envelopes as well as in protoplanetary disks for which $R > 10^6$ is needed to retrieve abundance profiles, whether from absorption or emission line profiles. For example, relating the water abundance to substructures in disks, such as appears the case for the HD 100546 disk (Sect. 9.2), cannot be done without full velocity resolution. All three water lines connecting with the ground-state – 557, 1113, 1670 GHz (179.5 μm) – are important, as are their isotopolog lines. ALMA cannot do such studies due to the blocking of these lines by the Earth's atmosphere. To determine HDO/H_2O in cold gas, the 893 GHz 1_{11}–0_{00} HDO line is particularly useful. For warmer regions such as protostars and shocks, spectrally resolved profiles of the 988, 1097 and 1153 GHz lines should be added to retrieve physical parameters of individual velocity components.

12. Conclusions

Here we summarize in abbreviated form the main conclusions that water observations with *Herschel* have taught us on the physics and chemistry in star-forming regions, and their evolution from cloud to disk. We also reiterate some of the broader implications of the WISH+ program, for example for the interpretation of extragalactic data on water. Key points are that *Herschel* has revealed new physical components, has tested and confirmed basic chemical networks, and has pointed the way for the interpretation of subsequent (ground-based) data of other molecules, including the various transitions of CO itself, both in Galactic and extragalactic sources.

12.1. Water line profiles and the physical components they trace

– *Water traces active star formation sites:* the bulk of the observed gaseous water emission with *Herschel* in star-forming regions is associated with warm kinetically heated gas in outflows and shocks that trace gas of several hundred K. This same gas is traced by CO lines with $J_{up} > 14$, but not by lower-J CO lines.

– *Water spectral profiles are complex:* at least two different physical components are universally seen in water and high-J CO lines for low-mass sources: a broad component (cavity shock, disk wind, turbulent entrainment) with $T_{rot}(CO) \approx$ 300 K, and a medium-broad offset (slightly blue-shifted) dissociative J−type 'spot shock' with $T_{rot}(CO) \approx 700$ K. The latter category includes extremely high velocity features with velocities out to ±100 km s^{-1} seen in a small fraction of sources. For higher-mass sources, only the broad component is seen. Very few cloud positions show narrow (FWHM < few km s^{-1}) water emission lines.

– *Water profiles probe small motions:* inverse P Cygni profiles due to infall are seen in a fraction of protostellar sources, indicating mass infall rates from cloud onto envelope of 10^{-5}–10^{-4} $M_\odot$ yr^{-1} for low-mass protostars, and increasing up to 10^{-4}–10^{-2} $M_\odot$ yr^{-1} for high-mass sources. A slightly smaller fraction of sources show regular P Cygni profiles indicating expansion.

– *Water emission is compact:* for most low-mass sources, the water emission, and thus the mechanisms that produce it, is limited to ~1000 au radius from the central source, with emitting areas even smaller. Even for high-mass sources such as Orion, bright water emission is compact and limited to <25 000 au (<0.1 pc) scale. For cases where water emission is observed off source, the emitting areas are larger as the warm gas can expand in more directions.

– *Water traces warm, dense gas:* the inferred physical conditions in the water emitting gas are high density ($>10^5$ cm^{-3}) and kinetic temperature (300–1000 K) with small emitting areas on source, of order 100 au for low-mass protostars and 1000 au for high-mass protostars. *Herschel* was not sensitive to a possible very hot component of several thousand K.

– *Water points to UV-irradiated outflow cavities and shocks:* the data on H_2O, OH and other hydrides indicate UV fields up to 10^2–10^3 times the general interstellar radiation field in both low- and high-mass sources in outflow cavity walls on scales of the *Herschel* beam (~20″). A new class of UV-irradiated outflows or shocks is required to explain the data.

– *Water is a significant but not dominant coolant:* far-infrared line cooling in low-mass protostars is dominated by CO and H_2O

in the earliest low-mass Class 0 and I stages, with [O I] becoming relatively more important in the later stage. The total H_2O line cooling does not change from Class 0 to Class I, whereas that of CO decreases by a factor of 2. The absolute [O I] cooling is similar from Class 0 to Class II, but its fraction increases as the jet changes from being mostly molecular to being primarily atomic. For high-mass sources, line cooling is dominated by CO, with a much lower fraction of H_2O and OH cooling than for low-mass sources.
– *Water in extragalactic sources traces buried star formation activity*, originating from scales much smaller than entire molecular clouds.

12.2. Water abundances in different components

– *Water abundance in outflows and shocks is low:* the water abundance in warm outflows and shocks is universally found to be low, only $\sim 10^{-6}$, much less than the H_2O/H_2 abundance of 4×10^{-4} expected if all volatile oxygen is driven into water. Only very hot gas (>1000 K) may have water abundances close to 10^{-4}. Simplified chemical models confirm that such high temperatures are needed to drive the bulk of the oxygen into water in dense gas with high UV fields.
– *High temperature routes to water confirmed:* comparison with line profiles of other ice species such as CH_3OH and NH_3 shows that ice sputtering is only significant at low velocities (out to ± 10 km s^{-1}). High temperature gas-phase formation dominates water production at high velocities.
– *Water abundance profiles in cold cores retrieved:* velocity resolved HIFI line profiles have allowed the water abundance to be derived as a function of position across pre-stellar cores and protostellar envelopes, even if the sources are not spatially resolved or mapped. A relatively high gaseous water abundance of $\sim 10^{-7}$ is found in the outer layers, decreasing roughly inversely with density deeper into the core.
– *Simplified water chemistry networks explain data:* small gas-grain chemical models including freeze-out of O, formation of H_2O ice, (photo-)desorption of ice, and photodissociation of gaseous H_2O, work well to explain water profiles in a wide range of low-mass sources. The best fits imply a range of the external radiation field $G_{\rm ISRF}$, cosmic-ray induced field $G_{\rm CR}$ and pre-stellar core lifetimes.
– *Water ice forms early:* water ice is primarily formed in the cold pre-stellar stage. Some small enhancement (but no destruction) is possible in the cold outer envelopes up to $\sim$15–20 K.
– *Bulk HDO/H_2O ice is lower than cold HDO/H_2O gas:* HDO ground-state line profiles obtained with *Herschel* are well fitted by a constant HDO/H_2O abundance ratio of $\sim$0.025 in cold protostellar envelopes. This value reflects the high HDO/H_2O abundance ratio in cold gas and in the outermost layers of the water ice which are enriched in deuterium, not that of the bulk of the ice. Indeed, observed HDO/H_2O values in hot cores, where the bulk ices sublimate, are up to an order of magnitude lower. A high D_2O/HDO ratio compared with HDO/H_2O is a signature of cold gas and ice chemistry in the dense pre-stellar phase.
– *NH_3 does not follow H_2O:* In stark contrast with H_2O and HDO, the gaseous NH_3 abundance profile inferred from *Herschel* data is flat with radius throughout pre-stellar cores and protostellar envelopes. This strengthens the conclusion that the bulk of the gaseous NH_3 does not result from photodesorption of ammonia ice, but from cold gas-phase processes.
– *Inner hot cores are dry:* inner hot core abundances derived with a step-function retrieval analysis show a large variation from 10^{-6} to a few $\times 10^{-4}$ for low- and high-mass sources, with only a few sources at the upper end of this range. This suggests that most hot cores are "dry", although not as dry as originally thought in analyses in which the small scale physical structure is ignored. *Herschel* data are not well suited to constrain hot core abundances due to high optical depths in THz continuum and lines. ALMA and NOEMA can make major advances on this topic.
– *Similarity of low- and high-mass sources:* all conclusions on abundances and chemistry hold across the luminosity range.
– *Puzzling oxygen budget strengthens evidence for UDO:* the combined analysis of water gas, water ice and O_2 limits in cold clouds indicates that a large fraction of the oxygen budget is unaccounted for. Within the simple water chemistry models, the only solution is to have a short pre-stellar stage of only 0.1 Myr to prevent all O being turned into H_2O. An alternative option is for dense cores to have a small fraction of large (>1 μm) grains which hide more than 50% of the water ice from being observed through infrared absorption. This solution does not apply to hot cores and shocks, where the large icy grains should have sublimated and where a large fraction of oxygen is also missing. Another option is therefore that oxygen is in some refractory form called UDO, whose abundance increases from diffuse to dense clouds, and which consists of material that does not vaporize or atomize even in strong shocks up to 1000 K.
– *The water ice reservoir in disks is spatially confined and encompasses less of the disk than expected:* the weak water vapor emission from protoplanetary disks suggests either radial confinement of large icy grains in the inner disk or in several radial rings, or vertical settling of icy grains to the midplane below heights where UV photons can penetrate for photodesorption. This finding suggests that low gas-phase oxygen abundances in outer disks are common.

12.3. Water from clouds to disks

In conclusion, what have we learned about water in star-forming regions?
– *Most water forms prior to star formation:* most water is formed as ice in dense molecular clouds before they collapse to form stars. However, not all oxygen may be turned into water ice, possibly implying a short pre-stellar phase (Sects. 6, 7).
– *Water formed through high-T chemistry is mainly lost to space:* significant amounts of water are also produced or reformed by high temperature chemistry in warm outflows or shocks (Sect. 5). However, most of this water is lost to space in outflows and does not contribute to the water reservoir in planet-forming disks.
– *Water is mostly transported as ice during protostellar collapse and infall:* water enters the (forming) disk at large radii, with no observational evidence yet that it is affected by accretion shocks (Sect. 9.1).
– *Water locked up early in large grains in outer disks:* the water vapor content in the outer regions of protoplanetary disks indicates that the reservoir of available water ice is smaller than expected, being either radially or vertically confined or both. The weakness of the HIFI lines implies that ice-coated grains grow quickly, settle to the midplane and drift inward when grown to mm/cm sizes. This process likely starts already in embedded phase. It also implies that disks with a low gas-phase oxygen abundance are common, in line with the findings of low volatile carbon abundances (Sect. 9.2).
– *Inner disk water reservoir still to be probed:* warm water in the disk surface layers has been observed by *Herschel* and

Spitzer but the inner disk midplane inside the water iceline is still invisible (Sect. 9.2.2).

– *New planetary systems are likely to be born with sufficient water to become habitable:* the *Herschel* data have shown that water gas and ice are commonly associated with star-forming regions and that this conclusion is independent of "environment" or location in our Galaxy. A key requirement is that the cloud out of which the star and disk are formed is cold enough ($\lesssim$25 K) to enable water ice formation and has a long enough lifetime prior to collapse ($\gtrsim$0.1 Myr) to convert a significant fraction of atomic oxygen to water ice (Sect. 7). Various loss and gain factors en route from cloud to disk and planet-forming sites then control the ultimate outcome of the water supply to a nascent planet (Sect. 11.6.4).

In conclusion, *Herschel* has shown that water has lived up to its reputation of being a particularly interesting molecule for studying the physics and chemistry of star-forming regions. The large abundance changes of gas-phase water between cold and warm regions – now fully quantified – as well as the sensitivity of its line profiles to small motions, make water a unique diagnostic probe among the suite of interstellar molecules. *Herschel* has left a legacy for the analysis and interpretation of future water observations in Galactic and extragalactic sources. Also, even if *Herschel* has found that not all available oxygen is locked up in water gas or ice, this does not diminish its importance as a key ingredient for habitability on other planetary systems: water is found to be abundantly present in star- and planet-forming regions.

Acknowledgements. The authors would like to thank all WISH team members over the years for their seminal contributions to this project, as well as the entire HIFI science consortium for two wonderful decades of working together to make this happen. They are particularly grateful to Malcolm Walmsley, who stimulated the WISH program from the very beginning and helped with numerous projects. He left a great legacy. Fruitful collaborations with the DIGIT and WILL teams, and with members of the HDO team, are also acknowledged. Detailed discussions with Kathrin Altwegg and Martin Rubin on the oxygen budget in comets and with Bruce Draine on interstellar clouds are appreciated. Constructive comments from the referee have helped to improve the paper. A big salute goes to the HIFI and PACS instrument teams and to ESA for designing, building and operating these two powerful instruments and the *Herschel* Space Observatory. *Herschel* was an ESA space observatory with science instruments provided by the European-led Principal Investigator consortia and with important participation from NASA. HIFI was designed and built by a consortium of institutes and university de-partments from across Europe, Canada and the US under the leadership of SRON Netherlands Institute for Space Research, Groningen, The Netherlands with major contributions from Germany, France and the US. Consortium members are: Canada: CSA, U. Waterloo; France: CESR, LAB, LERMA, IRAM; Germany: KOSMA, MPIfR, MPS; Ireland, NUI Maynooth; Italy: ASI, IFSI-INAF, Arcetri-INAF; Netherlands: SRON, TUD; Poland: CAMK, CBK; Spain: Observatorio Astronómico Nacional (IGN), Centro de Astrobiologıa (CSIC-INTA); Sweden: Chalmers University of Technology – MC2, RSS & GARD, Onsala Space Observatory, Swedish National Space Board, Stockholm University – Stockholm Observatory; Switzerland: ETH Zürich, FHNW; USA: Caltech, JPL, NHSC. PACS has been developed by a consortium of institutes led by MPE (Germany) and including UVIE (Austria); KUL, CSL, IMEC (Belgium); CEA, OAMP (France); MPIA (Germany); IFSI, OAP/OAT, OAA/CAISMI, LENS, SISSA (Italy); IAC (Spain). This development has been supported by the funding agencies BMVIT (Austria), ESA-PRODEX (Belgium), CEA/CNES (France), DLR (Germany), ASI (Italy), and CICYT/MCYT (Spain) Astrochemistry in Leiden is supported by the Netherlands Research School for Astronomy (NOVA). J.R.G. thanks the Spanish MICIU for funding support under grants AYA2017-85111-P and PID2019-106110GB-I00. Part of this research was carried out at the Jet Propulsion Laboratory, California Institute of Technology, under a contract with NASA. D.F. acknowledges financial support from the Italian Ministry of Education, Universities and Research, project SIR (RBSI14ZRHR) as well as project PRIN-INAF-MAIN-STREAM 2017. AK acknowledges support from the Polish National Science Center grant 2016/21/D/ST9/01098 and the First TEAM grant of the Foundation for Polish Science No. POIR.04.04.00-00-5D21/18-00.

References

Adams, F. C. 2010, ARA&A, 48, 47
A'Hearn, M. F. 2011, ARA&A, 49, 281
Aikawa, Y., & Herbst, E. 1999, A&A, 351, 233
Aikawa, Y., Wakelam, V., Hersant, F., Garrod, R. T., & Herbst, E. 2012, ApJ, 760, 40
Albertsson, T., Semenov, D., & Henning, T. 2014, ApJ, 784, 39
Alexander, C. M. O. D., Fogel, M., Yabuta, H., & Cody, G. D. 2007, Geochim. Cosmochim. Acta, 71, 4380
Ali-Dib, M., Mousis, O., Petit, J.-M., & Lunine, J. I. 2014, ApJ, 785, 125
ALMA Partnership (Brogan, C. L., et al.) 2015, ApJ, 808, L3
Alonso-Martínez, M., Riviere-Marichalar, P., Meeus, G., et al. 2017, A&A, 603, A138
Altwegg, K., Balsiger, H., Berthelier, J. J., et al. 2017, Phil. Trans. R. Soc. London, Ser. A, 375, 20160253
Altwegg, K., Balsiger, H., & Fuselier, S. A. 2019, ARA&A, 57, 113
Altwegg, K., Balsiger, H., Hänni, N., et al. 2020, Nat. Astron., 4, 533
Andersson, S., & van Dishoeck, E. F. 2008, A&A, 491, 907
Andrews, S. M., Wilner, D. J., Hughes, A. M., et al. 2012, ApJ, 744, 162
Andrews, S. M., Huang, J., Pérez, L. M., et al. 2018, ApJ, 869, L41
Arasa, C., van Hemert, M. C., van Dishoeck, E. F., & Kroes, G. J. 2013, J. Phys. Chem. A, 117, 7064
Arasa, C., Koning, J., Kroes, G.-J., Walsh, C., & van Dishoeck, E. F. 2015, A&A, 575, A121
Artur de la Villarmois, E., Jørgensen, J. K., Kristensen, L. E., et al. 2019, A&A, 626, A71
Asplund, M., Grevesse, N., Sauval, A. J., & Scott, P. 2009, ARA&A, 47, 481
Audard, M., Ábrahám, P., Dunham, M. M., et al. 2014, in Protostars and Planets VI, eds. H. Beuther, R. S. Klessen, C. P. Dullemond, & T. Henning (Tucson: University of Arizona Press), 387
Bachiller, R., Cernicharo, J., Martin-Pintado, J., Tafalla, M., & Lazareff, B. 1990, A&A, 231, 174
Bachiller, R., Martin-Pintado, J., & Planesas, P. 1991, A&A, 251, 639
Balsiger, H., Altwegg, K., Bochsler, P., et al. 2007, Space Sci. Rev., 128, 745
Banzatti, A., Pontoppidan, K. M., Salyk, C., et al. 2017, ApJ, 834, 152
Banzatti, A., Pascucci, I., Bosman, A. D., et al. 2020, ApJ, 903, 124
Bardyn, A., Baklouti, D., Cottin, H., et al. 2017, MNRAS, 469, S712
Baulch, D., Cobos, C., Cox, R., et al. 1992, J. Phys. Chem. Ref. Data, 21, 411
Benz, A. O., Bruderer, S., van Dishoeck, E. F., et al. 2010, A&A, 521, L35
Benz, A. O., Bruderer, S., van Dishoeck, E. F., et al. 2016, A&A, 590, A105
Bergin, E. A., & Tafalla, M. 2007, ARA&A, 45, 339
Bergin, E. A., Neufeld, D. A., & Melnick, G. J. 1998, ApJ, 499, 777
Bergin, E. A., Melnick, G. J., Stauffer, J. R., et al. 2000, ApJ, 539, L129
Bergin, E. A., Alves, J., Huard, T., & Lada, C. J. 2002, ApJ, 570, L101
Bergin, E. A., Hogerheijde, M. R., Brinch, C., et al. 2010a, A&A, 521, L33
Bergin, E. A., Phillips, T. G., Comito, C., et al. 2010b, A&A, 521, L20
Bergin, E. A., Du, F., Cleeves, L. I., et al. 2016, ApJ, 831, 101
Bergner, J. B., Öberg, K. I., Bergin, E. A., et al. 2019, ApJ, 876, 25
Beuther, H., Zhang, Q., Bergin, E. A., et al. 2007, A&A, 468, 1045
Bieler, A., Altwegg, K., Balsiger, H., et al. 2015, Nature, 526, 678
Bisschop, S. E., Jørgensen, J. K., van Dishoeck, E. F., & de Wachter, E. B. M. 2007, A&A, 465, 913
Bjerkeli, P., Liseau, R., Larsson, B., et al. 2012, A&A, 546, A29
Bjerkeli, P., van der Wiel, M. H. D., Harsono, D., Ramsey, J. P., & Jørgensen, J. K. 2016, Nature, 540, 406
Bjerkeli, P., Ramsey, J. P., Harsono, D., et al. 2019, A&A, 631, A64
Blandford, R., Meier, D., & Readhead, A. 2019, ARA&A, 57, 467
Boehler, Y., Ricci, L., Weaver, E., et al. 2018, ApJ, 853, 162
Boogert, A. C. A., Pontoppidan, K. M., Knez, C., et al. 2008, ApJ, 678, 985
Boogert, A. C. A., Chiar, J. E., Knez, C., et al. 2013, ApJ, 777, 73
Boogert, A. C. A., Gerakines, P. A., & Whittet, D. C. B. 2015, ARA&A, 53, 541
Boonman, A. M. S., & van Dishoeck, E. F. 2003, A&A, 403, 1003
Boonman, A. M. S., Doty, S. D., van Dishoeck, E. F., et al. 2003a, A&A, 406, 937
Boonman, A. M. S., van Dishoeck, E. F., Lahuis, F., & Doty, S. D. 2003b, A&A, 399, 1063
Booth, A. S., Walsh, C., Ilee, J. D., et al. 2019, ApJ, 882, L31
Bosman, A. D., & Banzatti, A. 2019, A&A, 632, L10
Bosman, A. D., Tielens, A. G. G. M., & van Dishoeck, E. F. 2018a, A&A, 611, A80
Bosman, A. D., Walsh, C., & van Dishoeck, E. F. 2018b, A&A, 618, A182
Bottinelli, S., Boogert, A. C., Bouwman, J., et al. 2010, ApJ, 718, 1100
Brinch, C., & Hogerheijde, M. R. 2010, A&A, 523, A25
Brinch, C., Crapsi, A., Hogerheijde, M. R., & Jørgensen, J. K. 2007, A&A, 461, 1037

Bruderer, S., Benz, A. O., Doty, S. D., van Dishoeck, E. F., & Bourke, T. L. 2009, ApJ, 700, 872
Bruderer, S., Benz, A. O., Stäuber, P., & Doty, S. D. 2010, ApJ, 720, 1432
Bruderer, S., van Dishoeck, E. F., Doty, S. D., & Herczeg, G. J. 2012, A&A, 541, A91
Brünken, S., Sipilä, O., Chambers, E. T., et al. 2014, Nature, 516, 219
Busquet, G., Lefloch, B., Benedettini, M., et al. 2014, A&A, 561, A120
Carney, M. T., Yıldız, U. A., Mottram, J. C., et al. 2016, A&A, 586, A44
Carr, J. S., & Najita, J. R. 2008, Science, 319, 1504
Carr, J. S., & Najita, J. R. 2011, ApJ, 733, 102
Carr, J. S., Tokunaga, A. T., & Najita, J. 2004, ApJ, 603, 213
Cartledge, S. I. B., Lauroesch, J. T., Meyer, D. M., & Sofia, U. J. 2004, ApJ, 613, 1037
Caselli, P., Hartquist, T. W., & Havnes, O. 1997, A&A, 322, 296
Caselli, P., Keto, E., Pagani, L., et al. 2010, A&A, 521, L29
Caselli, P., Keto, E., Bergin, E. A., et al. 2012, ApJ, 759, L37
Caselli, P., Bizzocchi, L., Keto, E., et al. 2017, A&A, 603, L1
Cazaux, S., Caselli, P., & Spaans, M. 2011, ApJ, 741, L34
Ceccarelli, C., Bacmann, A., Boogert, A., et al. 2010, A&A, 521, L22
Ceccarelli, C., Caselli, P., Bockelée-Morvan, D., et al. 2014, in Protostars & Planets VI, eds. H. Beuther, R., Klessen, K. Dullemond, Th. Henning (Tucson: University of Arizona Press), 859
Cernicharo, J., Goicoechea, J. R., Daniel, F., et al. 2006, ApJ, 649, L33
Chavarría, L., Herpin, F., Jacq, T., et al. 2010, A&A, 521, L37
Chen, J.-H., Goldsmith, P. F., Viti, S., et al. 2014, ApJ, 793, 111
Cheung, A. C., Rank, D. M., & Townes, C. H. 1969, Nature, 221, 626
Chiang, E. I., Joung, M. K., Creech-Eakman, M. J., et al. 2001, ApJ, 547, 1077
Chiang, H.-F., Looney, L. W., & Tobin, J. J. 2012, ApJ, 756, 168
Chiappini, C., Romano, D., & Matteucci, F. 2003, MNRAS, 339, 63
Choi, Y. 2015, PhD thesis, University of Groningen, The Netherlands
Choi, Y., van der Tak, F. F. S., Bergin, E. A., & Plume, R. 2014, A&A, 572, L10
Choi, Y., van der Tak, F. F. S., van Dishoeck, E. F., Herpin, F., & Wyrowski, F. 2015, A&A, 576, A85
Chyba, C. F., & Hand, K. P. 2005, ARA&A, 43, 31
Ciesla, F. J., & Cuzzi, J. N. 2006, Icarus, 181, 178
Cleeves, L. I., Bergin, E. A., Alexander, C. M. O. D., et al. 2014, Science, 345, 1590
Cleeves, L. I., Öberg, K. I., Wilner, D. J., et al. 2016, ApJ, 832, 110
Codella, C., Lefloch, B., Ceccarelli, C., et al. 2010, A&A, 518, L112
Conrad, M. E., & Fich, M. 2020, ApJ, 890, 178
Coutens, A., Vastel, C., Caux, E., et al. 2012, A&A, 539, A132
Coutens, A., Vastel, C., Cabrit, S., et al. 2013a, A&A, 560, A39
Coutens, A., Vastel, C., Cazaux, S., et al. 2013b, A&A, 553, A75
Coutens, A., Vastel, C., Hincelin, U., et al. 2014, MNRAS, 445, 1299
Crapsi, A., Caselli, P., Walmsley, M. C., & Tafalla, M. 2007, A&A, 470, 221
Cruz-Diaz, G. A., Martín-Doménech, R., Moreno, E., Muñoz Caro, G. M., & Chen, Y.-J. 2018, MNRAS, 474, 3080
Cuppen, H. M., & Herbst, E. 2007, ApJ, 668, 294
Cuppen, H. M., Walsh, C., Lamberts, T., et al. 2017, Space Sci. Rev., 212, 1
Daniel, F., Dubernet, M.-L., & Grosjean, A. 2011, A&A, 536, A76
Dartois, E., Thi, W., Geballe, T. R., et al. 2003, A&A, 399, 1009
de Graauw, T., Helmich, F. P., Phillips, T. G., et al. 2010, A&A, 518, L6
Dent, W. R. F., Greaves, J. S., & Coulson, I. M. 2005, MNRAS, 359, 663
Dent, W. R. F., Thi, W. F., Kamp, I., et al. 2013, PASP, 125, 477
Dionatos, O., & Güdel, M. 2017, A&A, 597, A64
Dionatos, O., Jørgensen, J. K., Green, J. D., et al. 2013, A&A, 558, A88
Dionatos, O., Ray, T., & Güdel, M. 2018, A&A, 616, A84
Dominik, C., Ceccarelli, C., Hollenbach, D., & Kaufman, M. 2005, ApJ, 635, L85
Doty, S. D., van Dishoeck, E. F., & Tan, J. C. 2006, A&A, 454, L5
Draine, B. T. 1978, ApJS, 36, 595
Draine, B. T., & Hensley, B. S. 2020, ApJ, submitted
Draine, B. T., Roberge, W. G., & Dalgarno, A. 1983, ApJ, 264, 485
Drozdovskaya, M. N., van Dishoeck, E. F., Rubin, M., Jørgensen, J. K., & Altwegg, K. 2019, MNRAS, 490, 50
Drozdovskaya, M. N., Walsh, C., van Dishoeck, E. F., et al. 2016, MNRAS, 462, 977
Du, F., Bergin, E. A., & Hogerheijde, M. R. 2015, ApJ, 807, L32
Du, F., Bergin, E. A., Hogerheijde, M., et al. 2017, ApJ, 842, 98
Dubernet, M., Daniel, F., Grosjean, A., & Lin, C. Y. 2009, A&A, 497, 911
Dulieu, F., Congiu, E., Noble, J., et al. 2013, Nat. Sci. Rep., 3, 1338
Dunham, M. M., & Vorobyov, E. I. 2012, ApJ, 747, 52
Dutrey, A., Guilloteau, S., & Simon, M. 2003, A&A, 402, 1003
Dutrey, A., Di Folco, E., Beck, T., & Guilloteau, S. 2016, A&ARv, 24, 5
Eistrup, C., & Walsh, C. 2019, A&A, 621, A75
Emprechtinger, M., Lis, D. C., Bell, T., et al. 2010, A&A, 521, L28
Emprechtinger, M., Lis, D. C., Rolffs, R., et al. 2013, ApJ, 765, 61
Enoch, M. L., Evans, II, N. J., Sargent, A. I., et al. 2008, ApJ, 684, 1240
Evans, N. J., Dunham, M. M., Jørgensen, J. K., et al. 2009, ApJS, 181, 321
Favre, C., Cleeves, L. I., Bergin, E. A., Qi, C., & Blake, G. A. 2013, ApJ, 776, L38
Fedele, D., Pascucci, I., Brittain, S., et al. 2011, ApJ, 732, 106
Fedele, D., Bruderer, S., van Dishoeck, E. F., et al. 2012, A&A, 544, L9
Fedele, D., Bruderer, S., van Dishoeck, E. F., et al. 2013, A&A, 559, A77
Fedele, D., Carney, M., Hogerheijde, M. R., et al. 2017, A&A, 600, A72
Fich, M., Johnstone, D., van Kempen, T. A., et al. 2010, A&A, 518, L86
Flagey, N., Goldsmith, P. F., Lis, D. C., et al. 2013, ApJ, 762, 11
Flaherty, K. M., Hughes, A. M., Teague, R., et al. 2018, ApJ, 856, 117
Flaherty, K., Hughes, A. M., Simon, J. B., et al. 2020, ApJ, 895, 109
Flower, D. R., & Pineau des Forêts, G. 2010, MNRAS, 406, 1745
Flynn, G. J., Feser, M., Keller, L. P., et al. 2001, Lunar Planet. Sci. Conf., 32 1603
Franklin, J., Snell, R. L., Kaufman, M. J., et al. 2008, ApJ, 674, 1015
Fray, N., Bardyn, A., Cottin, H., et al. 2016, Nature, 538, 72
Frimann, S., Jørgensen, J. K., Dunham, M. M., et al. 2017, A&A, 602, A120
Furuya, K., Aikawa, Y., Nomura, H., Hersant, F., & Wakelam, V. 2013, ApJ, 779, 11
Furuya, K., Aikawa, Y., Hincelin, U., et al. 2015, A&A, 584, A124
Furuya, K., van Dishoeck, E. F., & Aikawa, Y. 2016, A&A, 586, A127
Furuya, K., Drozdovskaya, M. N., Visser, R., et al. 2017, A&A, 599, A40
Galli, D., & Shu, F. H. 1993, ApJ, 417, 220
Gensheimer, P. D., Mauersberger, R., & Wilson, T. L. 1996, A&A, 314, 281
Gerin, M., Neufeld, D. A., & Goicoechea, J. R. 2016, ARA&A, 54, 181
Gibb, E. L., Whittet, D. C. B., Boogert, A. C. A., & Tielens, A. G. G. M. 2004, ApJS, 151, 35
Ginsburg, A., Bally, J., Goddi, C., Plambeck, R., & Wright, M. 2018, ApJ, 860, 119
Glassgold, A. E., Mamon, G. A., & Huggins, P. J. 1991, ApJ, 373, 254
Godard, B., Pineau des Forêts, G., Lesaffre, P., et al. 2019, A&A, 622, A100
Goicoechea, J. R., Joblin, C., Contursi, A., et al. 2011, A&A, 530, L16
Goicoechea, J. R., Cernicharo, J., Karska, A., et al. 2012, A&A, 548, A77
Goicoechea, J. R., Chavarría, L., Cernicharo, J., et al. 2015, ApJ, 799, 102
Goldsmith, P. F., & Langer, W. D. 1978, ApJ, 222, 881
Goldsmith, P. F., Melnick, G. J., Bergin, E. A., et al. 2000, ApJ, 539, L123
Goldsmith, P. F., Liseau, R., Bell, T. A., et al. 2011, ApJ, 737, 96
Gómez-Ruiz, A. I., Codella, C., Viti, S., et al. 2016, MNRAS, 462, 2203
González-Alfonso, E., Fischer, J., Aalto, S., & Falstad, N. 2014, A&A, 567, A91
González-Alfonso, E., Fischer, J., Spoon, H. W. W., et al. 2017, ApJ, 836, 11
Gorti, U., & Hollenbach, D. 2008, ApJ, 683, 287
Green, J. D., Evans, II, N. J., Jørgensen, J. K., et al. 2013, ApJ, 770, 123
Green, J. D., Yang, Y.-L., Evans, II, N. J., et al. 2016, AJ, 151, 75
Greenberg, J. M., & Hage, J. I. 1990, ApJ, 361, 260
Grevesse, N., Asplund, M., Sauval, A. J., & Scott, P. 2010, Ap&SS, 328, 179
Griffin, M. J., Abergel, A., Abreu, A., et al. 2010, A&A, 518, L3
Güdel, M., Lahuis, F., Briggs, K. R., et al. 2010, A&A, 519, A113
Güdel, M., Eibensteiner, C., Dionatos, O., et al. 2018, A&A, 620, L1
Guilloteau, S., Bachiller, R., Fuente, A., & Lucas, R. 1992, A&A, 265, L49
Gusdorf, A., Giannini, T., Flower, D. R., et al. 2011, A&A, 532, A53
Gusdorf, A., Anderl, S., Lefloch, B., et al. 2017, A&A, 602, A8
Habing, H. J. 1968, Bull. Astron. Inst. Netherlands, 19, 421
Hajigholi, M., Persson, C. M., Wirström, E. S., et al. 2016, A&A, 585, A158
Hama, T., Kouchi, A., & Watanabe, N. 2018, ApJ, 857, L13
Harsono, D., Jørgensen, J. K., van Dishoeck, E. F., et al. 2014, A&A, 562, A77
Harsono, D., Bruderer, S., & van Dishoeck, E. F. 2015, A&A, 582, A41
Harsono, D., Bjerkeli, P., van der Wiel, M. H. D., et al. 2018, Nat. Astron., 2, 646
Harsono, D., Persson, M. V., Ramos, A., et al. 2020, A&A, 636, A26
Hartmann, L., Ciesla, F., Gressel, O., & Alexander, R. 2017, Space Sci. Rev., 212, 813
Hartogh, P., Lellouch, E., Crovisier, J., et al. 2009, Planet. Space Sci., 57, 1596
Harwit, M., Neufeld, D. A., Melnick, G. J., & Kaufman, M. J. 1998, ApJ, 497, L105
He, J., Shi, J., Hopkins, T., Vidali, G., & Kaufman, M. J. 2015, ApJ, 801, 120
Heays, A. N., Bosman, A. D., & van Dishoeck, E. F. 2017, A&A, 602, A105
Helmich, F. P., van Dishoeck, E. F., Black, J. H., et al. 1996, A&A, 315, L173
Henning, T., & Salama, F. 1998, Science, 282, 2204
Herczeg, G. J., Karska, A., Bruderer, S., et al. 2012, A&A, 540, A84
Herpin, F., Chavarría, L., van der Tak, F., et al. 2012, A&A, 542, A76
Herpin, F., Chavarría, L., Jacq, T., et al. 2016, A&A, 587, A139
Hily-Blant, P., Magalhaes, V., Kastner, J., et al. 2017, A&A, 603, L6
Hincelin, U., Wakelam, V., Commerçon, B., Hersant, F., & Guilloteau, S. 2013, ApJ, 775, 44
Hjalmarson, Å., Frisk, U., Olberg, M., et al. 2003, A&A, 402, L39
Hogerheijde, M. R., & van der Tak, F. F. S. 2000, A&A, 362, 697
Hogerheijde, M. R., Bergin, E. A., Brinch, C., et al. 2011, Science, 334, 338
Hollenbach, D., Kaufman, M. J., Bergin, E. A., & Melnick, G. J. 2009, ApJ, 690, 1497

Honda, M., Kudo, T., Takatsuki, S., et al. 2016, ApJ, 821, 2
Hosokawa, T., Yorke, H. W., & Omukai, K. 2010, ApJ, 721, 478
Huang, J., Öberg, K. I., & Andrews, S. M. 2016, ApJ, 823, L18
Huélamo, N., de Gregorio-Monsalvo, I., Macias, E., et al. 2015, A&A, 575, L5
Hueso, R., & Guillot, T. 2005, A&A, 442, 703
Hughes, A. M., Andrews, S. M., Espaillat, C., et al. 2009, ApJ, 698, 131
Indriolo, N., Neufeld, D. A., DeWitt, C. N., et al. 2015a, ApJ, 802, L14
Indriolo, N., Neufeld, D. A., Gerin, M., et al. 2015b, ApJ, 800, 40
Ioppolo, S., Cuppen, H. M., Romanzin, C., van Dishoeck, E. F., & Linnartz, H. 2008, ApJ, 686, 1474
Ioppolo, S., Palumbo, M. E., Baratta, G. A., & Mennella, V. 2009, A&A, 493, 1017
Ioppolo, S., van Boheemen, Y., Cuppen, H. M., van Dishoeck, E. F., & Linnartz, H. 2011, MNRAS, 413, 2281
Isella, A., Guidi, G., Testi, L., et al. 2016, Phys. Rev. Lett., 117, 251101
Ivlev, A. V., Röcker, T. B., Vasyunin, A., & Caselli, P. 2015, ApJ, 805, 59
Izquierdo, A. F., Galván-Madrid, R., Maud, L. T., et al. 2018, MNRAS, 478, 2505
Jacq, T., Henkel, C., Walmsley, C. M., Jewell, P. R., & Baudry, A. 1988, A&A, 199, L5
Jacq, T., Walmsley, C. M., Henkel, C., et al. 1990, A&A, 228, 447
Jacq, T., Braine, J., Herpin, F., van der Tak, F., & Wyrowski, F. 2016, A&A, 595, A66
Jarugula, S., Vieira, J. D., Spilker, J. S., et al. 2019, ApJ, 880, 92
Jenkins, E. B. 2009, ApJ, 700, 1299
Jensen, S. S., Jørgensen, J. K., Kristensen, L. E., et al. 2019, A&A, 631, A25
Jensen, S. S., Jørgensen, J. K., Kristensen, L. E., et al. 2021, A&A, submitted
Jiménez-Serra, I., Caselli, P., Martín-Pintado, J., & Hartquist, T. W. 2008, A&A, 482, 549
Jiménez-Serra, I., Martín-Pintado, J., Caselli, P., Viti, S., & Rodríguez-Franco, A. 2009, ApJ, 695, 149
Jin, S., Isella, A., Huang, P., et al. 2019, ApJ, 881, 108
Johnston, K. G., Robitaille, T. P., Beuther, H., et al. 2015, ApJ, 813, L19
Johnstone, D., Fich, M., McCoey, C., et al. 2010, A&A, 521, L41
Jørgensen, J. K., & van Dishoeck, E. F. 2010a, ApJ, 725, L172
Jørgensen, J. K., & van Dishoeck, E. F. 2010b, ApJ, 710, L72
Jørgensen, J. K., Schöier, F. L., & van Dishoeck, E. F. 2002, A&A, 389, 908
Jørgensen, J. K., Visser, R., Sakai, N., et al. 2013, ApJ, 779, L22
Kaltenegger, L. 2017, ARA&A, 55, 433
Kama, M., Bruderer, S., van Dishoeck, E. F., et al. 2016, A&A, 592, A83
Karska, A., Herczeg, G. J., van Dishoeck, E. F., et al. 2013, A&A, 552, A141
Karska, A., Herpin, F., Bruderer, S., et al. 2014a, A&A, 562, A45
Karska, A., Kristensen, L. E., van Dishoeck, E. F., et al. 2014b, A&A, 572, A9
Karska, A., Kaufman, M. J., Kristensen, L. E., et al. 2018, ApJS, 235, 30
Kaufman, M. J., & Neufeld, D. A. 1996, ApJ, 456, 611
Kessler, M. F., Steinz, J. A., Anderegg, M. E., et al. 1996, A&A, 315, L27
Keto, E., Rybicki, G. B., Bergin, E. A., & Plume, R. 2004, ApJ, 613, 355
Keto, E., Rawlings, J., & Caselli, P. 2014, MNRAS, 440, 2616
Kissel, J., Altwegg, K., Clark, B. C., et al. 2007, Space Sci. Rev., 128, 823
Klotz, A., Harju, J., Ristorcelli, I., et al. 2008, A&A, 492, 767
Krijt, S., Ciesla, F. J., & Bergin, E. A. 2016, ApJ, 833, 285
Krijt, S., Bosman, A. D., Zhang, K., et al. 2020, ApJ, 899, 134
Kristensen, L. E., & Bergin, E. A., 2021, A&A, submitted
Kristensen, L. E., & Dunham, M. M. 2018, A&A, 618, A158
Kristensen, L. E., Visser, R., van Dishoeck, E. F., et al. 2010, A&A, 521, L30
Kristensen, L. E., van Dishoeck, E. F., Tafalla, M., et al. 2011, A&A, 531, L1
Kristensen, L. E., van Dishoeck, E. F., Bergin, E. A., et al. 2012, A&A, 542, A8
Kristensen, L. E., van Dishoeck, E. F., Benz, A. O., et al. 2013, A&A, 557, A23
Kristensen, L. E., Gusdorf, A., Mottram, J. C., et al. 2017a, A&A, 601, L4
Kristensen, L. E., van Dishoeck, E. F., Mottram, J. C., et al. 2017b, A&A, 605, A93
Kudo, T., Hashimoto, J., Muto, T., et al. 2018, ApJ, 868, L5
Kwon, W., Looney, L. W., Mundy, L. G., Chiang, H.-F., & Kemball, A. J. 2009, ApJ, 696, 841
Kwon, W., van der Tak, F. F. S., Karska, A., et al. 2017, A&A, submitted
Lacy, J. H., Knacke, R., Geballe, T. R., & Tokunaga, A. T. 1994, ApJ, 428, L69
Lacy, J. H., Sneden, C., Kim, H., & Jaffe, D. T. 2017, ApJ, 838, 66
Lamberts, T., & Kästner, J. 2017, ApJ, 846, 43
Lamberts, T., Cuppen, H. M., Ioppolo, S., & Linnartz, H. 2013, Phys. Chem. Chem. Phys., 15, 8287
Lamberts, T., Cuppen, H. M., Fedoseev, G., et al. 2014, A&A, 570, A57
Lamberts, T., Ioppolo, S., Cuppen, H. M., Fedoseev, G., & Linnartz, H. 2015, MNRAS, 448, 3820
Lamberts, T., Fedoseev, G., Puletti, F., et al. 2016, MNRAS, 455, 634
Larsson, B., & Liseau, R. 2017, A&A, 608, A133
Larsson, B., Liseau, R., Pagani, L., et al. 2007, A&A, 466, 999
Läuter, M., Kramer, T., Rubin, M., & Altwegg, K. 2019, MNRAS, 483, 852
Le Gal, R., Hily-Blant, P., Faure, A., et al. 2014, A&A, 562, A83
Lee, H.-H., Bettens, R. P. A., & Herbst, E. 1996, A&AS, 119, 111
Lee, J., Lee, J.-E., Lee, S., et al. 2013, ApJS, 209, 4
Lefloch, B., Cabrit, S., Codella, C., et al. 2010, A&A, 518, L113
Leurini, S., Gusdorf, A., Wyrowski, F., et al. 2014, A&A, 564, L11
Leurini, S., Wyrowski, F., Wiesemeyer, H., et al. 2015, A&A, 584, A70
Leurini, S., Herpin, F., van der Tak, F., et al. 2017, A&A, 602, A70
Li, X., Heays, A. N., Visser, R., et al. 2013, A&A, 555, A14
Li, Z.-Y., Krasnopolsky, R., Shang, H., & Zhao, B. 2014, ApJ, 793, 130
Liang, L., Johnstone, D., Cabrit, S., & Kristensen, L. E. 2020, ApJ, 900, 15
Linke, R. A., Goldsmith, P. F., Wannier, P. G., Wilson, R. W., & Penzias, A. A. 1977, ApJ, 214, 50
Linnartz, H., Ioppolo, S., & Fedoseev, G. 2015, Int. Rev. Phys. Chem., 34, 205
Liseau, R., Goldsmith, P. F., Larsson, B., et al. 2012, A&A, 541, A73
Liu, L., Weiß, A., Perez-Beaupuits, J. P., et al. 2017, ApJ, 846, 5
Liu, Y., Dipierro, G., Ragusa, E., et al. 2019, A&A, 622, A75
Lodders, K. 2010, Astrophys. Space Sci. Proc., 16, 379
Lodders, K. 2019, ArXiv e-prints [arXiv:1912.00844]
Lommen, D., Jørgensen, J. K., van Dishoeck, E. F., & Crapsi, A. 2008, A&A, 481, 141
Long, F., Herczeg, G. J., Pascucci, I., et al. 2017, ApJ, 844, 99
Long, F., Herczeg, G. J., Harsono, D., et al. 2019, ApJ, 882, 49
Loomis, R. A., Öberg, K. I., Andrews, S. M., & MacGregor, M. A. 2017, ApJ, 840, 23
Macías, E., Espaillat, C. C., Ribas, Á., et al. 2018, ApJ, 865, 37
Maercker, M., Schöier, F. L., Olofsson, H., Bergman, P., & Ramstedt, S. 2008, A&A, 479, 779
Mandell, A. M., Bast, J., van Dishoeck, E. F., et al. 2012, ApJ, 747, 92
Manoj, P., Watson, D. M., Neufeld, D. A., et al. 2013, ApJ, 763, 83
Manoj, P., Green, J. D., Megeath, S. T., et al. 2016, ApJ, 831, 69
Maret, S., Bergin, E. A., Neufeld, D. A., et al. 2009, ApJ, 698, 1244
Marseille, M. G., van der Tak, F. F. S., Herpin, F., et al. 2010, A&A, 521, L32
Martín-Pintado, J., Bachiller, R., & Fuente, A. 1992, A&A, 254, 315
Matuszak, M., Karska, A., Kristensen, L. E., et al. 2015, A&A, 578, A20
Maud, L. T., Cesaroni, R., Kumar, M. S. N., et al. 2019, A&A, 627, L6
McClure, M. K., Espaillat, C., Calvet, N., et al. 2015, ApJ, 799, 162
McClure, M. K., Dominik, C., & Kama, M. 2020, A&A, 642, L15
McElroy, D., Walsh, C., Markwick, A. J., et al. 2013, A&A, 550, A36
McGuire, B. A. 2018, ApJS, 239, 17
McKee, C. F., & Hollenbach, D. J. 1980, ARA&A, 18, 219
Meisner, J., Lamberts, T., & Kästner, J. 2017, ACS Earth Space Chem., 1, 399
Meixner, M., Cooray, A., Leisawitz, D., et al. 2019, ArXiv e-prints, [arXiv:1912.06213]
Melnick, G. J. 2009, ASP Conf. Ser. 417, 59
Melnick, G. J., & Kaufman, M. J. 2015, ApJ, 806, 227
Melnick, G. J., Stauffer, J. R., Ashby, M. L. N., et al. 2000, ApJ, 539, L77
Melnick, G. J., Tolls, V., Neufeld, D. A., et al. 2008, ApJ, 683, 876
Melnick, G. J., Tolls, V., Snell, R. L., et al. 2011, ApJ, 727, 13
Melnick, G. J., Tolls, V., Goldsmith, P. F., et al. 2012, ApJ, 752, 26
Melnick, G. J., Tolls, V., Snell, R. L., et al. 2020, ApJ, 892, 22
Mennella, V., Baratta, G. A., Palumbo, M. E., & Bergin, E. A. 2006, ApJ, 643, 923
Meyer, D. M., Jura, M., & Cardelli, J. A. 1998, ApJ, 493, 222
Millar, T. J., Farquhar, P. R. A., & Willacy, K. 1997, A&AS, 121, 139
Min, M., Bouwman, J., Dominik, C., et al. 2016, A&A, 593, A11
Minissale, M., Dulieu, F., Cazaux, S., & Hocuk, S. 2016, A&A, 585, A24
Miotello, A., Testi, L., Lodato, G., et al. 2014, A&A, 567, A32
Miotello, A., van Dishoeck, E. F., Williams, J. P., et al. 2017, A&A, 599, A113
Mitchell, G. F., Maillard, J.-P., Allen, M., Beer, R., & Belcourt, K. 1990, ApJ, 363, 554
Miura, H., Yamamoto, T., Nomura, H., et al. 2017, ApJ, 839, 47
Miyauchi, N., Hidaka, H., Chigai, T., et al. 2008, Chem. Phys. Lett., 456, 27
Morbidelli, A., Lunine, J. I., O'Brien, D. P., Raymond, S. N., & Walsh, K. J. 2012, Ann. Rev. Earth Planet. Sci., 40, 251
Morbidelli, A., Karato, S.-I., Ikoma, M., et al. 2018, Space Sci. Rev., 214, 110
Moscadelli, L., Sanna, A., Cesaroni, R., et al. 2019, A&A, 622, A206
Motte, F., Bontemps, S., & Louvet, F. 2018, ARA&A, 56, 41
Mottram, J. C., van Dishoeck, E. F., Schmalzl, M., et al. 2013, A&A, 558, A126
Mottram, J. C., Kristensen, L. E., van Dishoeck, E. F., et al. 2014, A&A, 572, A21
Mottram, J. C., van Dishoeck, E. F., Kristensen, L. E., et al. 2017, A&A, 600, A99
Mousis, O., Ronnet, T., Brugger, B., et al. 2016, ApJ, 823, L41
Mumma, M. J., & Charnley, S. B. 2011, ARA&A, 49, 471
Murillo, N. M., Lai, S.-P., Bruderer, S., Harsono, D., & van Dishoeck, E. F. 2013, A&A, 560, A103
Neill, J. L., Wang, S., Bergin, E. A., et al. 2013, ApJ, 770, 142
Neufeld, D. A. 2012, ApJ, 749, 125
Neufeld, D. A., & Dalgarno, A. 1989, ApJ, 340, 869
Neufeld, D. A., & Hollenbach, D. J. 1994, ApJ, 428, 170

Neufeld, D. A., Melnick, G. J., Sonnentrucker, P., et al. 2006, ApJ, 649, 816
Neufeld, D. A., González-Alfonso, E., Melnick, G., et al. 2010, A&A, 521, L5
Neufeld, D. A., Gusdorf, A., Güsten, R., et al. 2014, ApJ, 781, 102
Nisini, B., Giannini, T., & Lorenzetti, D. 2002, ApJ, 574, 246
Nisini, B., Benedettini, M., Codella, C., et al. 2010, A&A, 518, L120
Nisini, B., Santangelo, G., Antoniucci, S., et al. 2013, A&A, 549, A16
Nisini, B., Santangelo, G., Giannini, T., et al. 2015, ApJ, 801, 121
Noble, J. A., Congiu, E., Dulieu, F., & Fraser, H. J. 2012, MNRAS, 421, 768
Nordh, H. L., von Schéele, F., Frisk, U., et al. 2003, A&A, 402, L21
Notsu, S., van Dishoeck, E. F., Walsh, C., Bosman, A. D., & Nomura, H. 2021, A&A, submitted
Oba, Y., Miyauchi, N., Hidaka, H., et al. 2009, ApJ, 701, 464
Öberg, K. I., Linnartz, H., Visser, R., & van Dishoeck, E. F. 2009, ApJ, 693, 1209
Öberg, K. I., Boogert, A. C. A., Pontoppidan, K. M., et al. 2011a, ApJ, 740, 109
Öberg, K. I., Murray-Clay, R., & Bergin, E. A. 2011b, ApJ, 743, L16
Ott, S. 2010, ASP Conf. Ser., 434, 139
Pagani, L., Salez, M., & Wannier, P. G. 1992, A&A, 258, 479
Pagani, L., Vastel, C., Hugo, E., et al. 2009, A&A, 494, 623
Pagani, L., Steinacker, J., Bacmann, A., Stutz, A., & Henning, T. 2010, Science, 329, 1622
Pagani, L., Lesaffre, P., Jorfi, M., et al. 2013, A&A, 551, A38
Parise, B., Simon, T., Caux, E., et al. 2003, A&A, 410, 897
Persson, M. V., Jørgensen, J. K., & van Dishoeck, E. F. 2012, A&A, 541, A39
Persson, M. V., Jørgensen, J. K., van Dishoeck, E. F., & Harsono, D. 2014, A&A, 563, A74
Persson, M. V., Harsono, D., Tobin, J. J., et al. 2016, A&A, 590, A33
Phillips, T. G., van Dishoeck, E. F., & Keene, J. 1992, ApJ, 399, 533
Pilbratt, G. L., Riedinger, J. R., Passvogel, T., et al. 2010, A&A, 518, L1
Pineda, J. E., Szulágyi, J., Quanz, S. P., et al. 2019, ApJ, 871, 48
Poch, O., Istiqomah, I., Quirico, E., et al. 2020, Science, 367, aaw7462
Podio, L., Kamp, I., Flower, D., et al. 2012, A&A, 545, A44
Podio, L., Kamp, I., Codella, C., et al. 2013, ApJ, 766, L5
Poglitsch, A., Waelkens, C., Geis, N., et al. 2010, A&A, 518, L2
Pontoppidan, K. M., van Dishoeck, E. F., & Dartois, E. 2004, A&A, 426, 925
Pontoppidan, K. M., Salyk, C., Blake, G. A., & Käufl, H. U. 2010a, ApJ, 722, L173
Pontoppidan, K. M., Salyk, C., Blake, G. A., et al. 2010b, ApJ, 720, 887
Pontoppidan, K. M., Salyk, C., Bergin, E. A., et al. 2014, Protostars & Planets VI, eds. H. Beuther, R. Klessen, K. Dullemond, Th. Henning, (Tucson: University of Arizona Press), 36
Poteet, C. A., Pontoppidan, K. M., Megeath, S. T., et al. 2013, ApJ, 766, 117
Poteet, C. A., Whittet, D. C. B., & Draine, B. T. 2015, ApJ, 801, 110
Prasad, S. S., & Tarafdar, S. P. 1983, ApJ, 267, 603
Prodanović, T., Steigman, G., & Fields, B. D. 2010, MNRAS, 406, 1108
Przybilla, N., Nieva, M.-F., & Butler, K. 2008, ApJ, 688, L103
Putaud, T., Michaut, X., Le Petit, F., Roueff, E., & Lis, D. C. 2019, A&A, 632, A8
Qi, C., Kessler, J. E., Koerner, D. W., Sargent, A. I., & Blake, G. A. 2003, ApJ, 597, 986
Rawlings, J. M. C., Wilson, T. G., & Williams, D. A. 2019, MNRAS, 486, 10
Raymond, S. N., & Izidoro, A. 2017, Icarus, 297, 134
Risacher, C., Güsten, R., Stutzki, J., et al. 2018, J. Astron. Instrum., 7, 1840014
Rivière-Marichalar, P., Ménard, F., Thi, W. F., et al. 2012, A&A, 538, L3
Rivière-Marichalar, P., Bayo, A., Kamp, I., et al. 2015, A&A, 575, A19
Roberts, H., Herbst, E., & Millar, T. J. 2003, ApJ, 591, L41
Roelfsema, P. R., Helmich, F. P., Teyssier, D., et al. 2012, A&A, 537, A17
Roelfsema, P. R., Shibai, H., Armus, L., et al. 2018, PASA, 35, e030
Rotundi, A., Sierks, H., Della Corte, V., et al. 2015, Science, 347, aaa3905
Rubin, M., Altwegg, K., Balsiger, H., et al. 2019, MNRAS, 489, 594
Sakai, N., Sakai, T., Hirota, T., et al. 2014, Nature, 507, 78
Salinas, V. N., Hogerheijde, M. R., Bergin, E. A., et al. 2016, A&A, 591, A122
Salyk, C., Pontoppidan, K. M., Blake, G. A., et al. 2008, ApJ, 676, L49
Salyk, C., Pontoppidan, K. M., Blake, G. A., Najita, J. R., & Carr, J. S. 2011, ApJ, 731, 130
Salyk, C., Lacy, J. H., Richter, M. J., et al. 2015, ApJ, 810, L24
Salyk, C., Lacy, J., Richter, M., et al. 2019, ApJ, 874, 24
San José-García, I. 2015, PhD thesis, Leiden University, The Netherlands
San José-García, I., Mottram, J. C., Kristensen, L. E., et al. 2013, A&A, 553, A125
San José-García, I., Mottram, J. C., van Dishoeck, E. F., et al. 2016, A&A, 585, A103
Santangelo, G., Nisini, B., Giannini, T., et al. 2012, A&A, 538, A45
Santangelo, G., Nisini, B., Antoniucci, S., et al. 2013, A&A, 557, A22
Santangelo, G., Antoniucci, S., Nisini, B., et al. 2014a, A&A, 569, L8
Santangelo, G., Nisini, B., Codella, C., et al. 2014b, A&A, 568, A125
Schilke, P., Walmsley, C. M., Pineau des Forets, G., & Flower, D. R. 1997, A&A, 321, 293
Schmalzl, M., Visser, R., Walsh, C., et al. 2014, A&A, 572, A81
Schöier, F. L., van der Tak, F. F. S., van Dishoeck, E. F., & Black, J. H. 2005, A&A, 432, 369
Schoonenberg, D., & Ormel, C. W. 2017, A&A, 602, A21
Schwarz, K. R., Bergin, E. A., Cleeves, L. I., et al. 2016, ApJ, 823, 91
Sheffer, Y., Rogers, M., Federman, S. R., et al. 2008, ApJ, 687, 1075
Shen, C. J., Greenberg, J. M., Schutte, W. A., & van Dishoeck, E. F. 2004, A&A, 415, 203
Shipman, R. F., van der Tak, F. F. S., Wyrowski, F., Herpin, F., & Frieswijk, W. 2014, A&A, 570, A51
Shipman, R. F., Beaulieu, S. F., Teyssier, D., et al. 2017, A&A, 608, A49
Shu, F., Najita, J., Galli, D., Ostriker, E., & Lizano, S. 1993, in Protostars and Planets III, eds. E. H. Levy, & J. I. Lunine (Tucson: University of Arizona Press), 3
Sipilä, O., Hugo, E., Harju, J., et al. 2010, A&A, 509, A98
Sipilä, O., Caselli, P., & Harju, J. 2015, A&A, 578, A55
Sipilä, O., Caselli, P., Redaelli, E., Juvela, M., & Bizzocchi, L. 2019, MNRAS, 487, 1269
Smith, I. W. M., Herbst, E., & Chang, Q. 2004, MNRAS, 350, 323
Smith, R. L., Pontoppidan, K. M., Young, E. D., & Morris, M. R. 2015, ApJ, 813, 120
Snell, R. L., Howe, J. E., Ashby, M. L. N., et al. 2000, ApJ, 539, L101
Spaans, M., Hogerheijde, M. R., Mundy, L. G., & van Dishoeck, E. F. 1995, ApJ, 455, L167
Spaans, M., Neufeld, D., Lepp, S., Melnick, G. J., & Stauffer, J. 1998, ApJ, 503, 780
Stark, R., van der Tak, F. F. S., & van Dishoeck, E. F. 1999, ApJ, 521, L67
Stäuber, P., Doty, S. D., van Dishoeck, E. F., Jørgensen, J. K., & Benz, A. O. 2004, A&A, 425, 577
Stäuber, P., Doty, S. D., van Dishoeck, E. F., & Benz, A. O. 2005, A&A, 440, 949
Stäuber, P., Jørgensen, J. K., van Dishoeck, E. F., Doty, S. D., & Benz, A. O. 2006, A&A, 453, 555
Steinacker, J., Andersen, M., Thi, W.-F., et al. 2015, A&A, 582, A70
Sturm, E., González-Alfonso, E., Veilleux, S., et al. 2011, ApJ, 733, L16
Suutarinen, A. N., Kristensen, L. E., Mottram, J. C., Fraser, H. J., & van Dishoeck E. F. 2014, MNRAS, 440, 1844
Tabone, B., Godard, B., Pineau des Forêts, G., Cabrit, S., & van Dishoeck, E. F. 2020, A&A, 636, A60
Tafalla, M., Liseau, R., Nisini, B., et al. 2013, A&A, 551, A116
Takakuwa, S., Tsukamoto, Y., Saigo, K., & Saito, M. 2018, ApJ, 865, 51
Taquet, V., López-Sepulcre, A., Ceccarelli, C., et al. 2013, ApJ, 768, L29
Taquet, V., Charnley, S. B., & Sipilä, O. 2014, ApJ, 791, 1
Taquet, V., Furuya, K., Walsh, C., & van Dishoeck, E. F. 2016, MNRAS, 462, S99
Taquet, V., van Dishoeck, E. F., Swayne, M., et al. 2018, A&A, 618, A11
Teague, R., Henning, T., Guilloteau, S., et al. 2018, ApJ, 864, 133
Testi, L., Birnstiel, T., Ricci, L., et al. 2014, in Protostars and Planets VI, eds. H. Beuther, R. S. Klessen, C. P. Dullemond, & T. Henning (Tucson: University of Arizona Press), 339
Thi, W. F., van Dishoeck, E. F., Blake, G. A., et al. 2001, ApJ, 561, 1074
Thi, W.-F., Woitke, P., & Kamp, I. 2010, MNRAS, 407, 232
Tielens, A. G. G. M. 1983, A&A, 119, 177
Tielens, A. G. G. M. 2013, Rev. Mod. Phys., 85, 1021
Tielens, A. G. G. M., & Hagen, W. 1982, A&A, 114, 245
Tobin, J. J., Hartmann, L., Chiang, H.-F., et al. 2012, Nature, 492, 83
Tobin, J. J., Looney, L. W., Li, Z.-Y., et al. 2016, ApJ, 818, 73
Tychoniec, Ł., Hull, C. L. H., Kristensen, L. E., et al. 2019, A&A, 632, A101
van Dishoeck, E. F. 1998, Faraday Discuss., 109, 31
van Dishoeck, E. F. 2004, ARA&A, 42, 119
van Dishoeck, E. F., & Helmich, F. P. 1996, A&A, 315, L177
van Dishoeck, E. F., Kristensen, L. E., Benz, A. O., et al. 2011, PASP, 123, 138
van Dishoeck, E. F., Herbst, E., & Neufeld, D. A. 2013, Chem. Rev., 113, 9043
van Dishoeck, E. F., Bergin, E. A., Lis, D. C., & Lunine, J. I. 2014, in Protostars and Planets VI, eds. H. Beuther, R. S. Klessen, C. P. Dullemond, & T. Henning (Tucson: University of Arizona Press), 835
van der Marel, N., van Dishoeck, E. F., Bruderer, S., Pérez, L., & Isella, A. 2015, A&A, 579, A106
van der Tak, F., Neufeld, D., Yates, J., et al. 2005, ESA SP, 577, 431
van der Tak, F. F. S., Walmsley, C. M., Herpin, F., & Ceccarelli, C. 2006, A&A, 447, 1011
van der Tak, F. F. S., Black, J. H., Schöier, F. L., Jansen, D. J., & van Dishoeck, E. F. 2007, A&A, 468, 627
van der Tak, F. F. S., Marseille, M. G., Herpin, F., et al. 2010, A&A, 518, L107
van der Tak, F. F. S., Chavarría, L., Herpin, F., et al. 2013, A&A, 554, A83
van der Tak, F. F. S., Shipman, R. F., Jacq, T., et al. 2019, A&A, 625, A103
van der Werf, P. P., Berciano Alba, A., Spaans, M., et al. 2011, ApJ, 741, L38
van der Wiel, M. H. D., van der Tak, F. F. S., Lis, D. C., et al. 2010, A&A, 521, L43

van Kempen, T. A., Doty, S. D., van Dishoeck, E. F., Hogerheijde, M. R., & Jørgensen, J. K. 2008, A&A, 487, 975
van Kempen, T. A., Kristensen, L. E., Herczeg, G. J., et al. 2010, A&A, 518, L121
van Kempen, T. A., McCoey, C., Tisi, S., Johnstone, D., & Fich, M. 2014, A&A, 569, A53
van Kempen, T. A., Hogerheijde, M. R., van Dishoeck, E. F., et al. 2016, A&A, 587, A17
van 't Hoff, M. L. R., Persson, M. V., Harsono, D., et al. 2018a, A&A, 613, A29
van 't Hoff, M. L. R., Tobin, J. J., Harsono, D., & van Dishoeck, E. F. 2018b, A&A, 615, A83
Vasta, M., Codella, C., Lorenzani, A., et al. 2012, A&A, 537, A98
Visser, R., & Bergin, E. A. 2012, ApJ, 754, L18
Visser, R., van Dishoeck, E. F., Doty, S. D., & Dullemond, C. P. 2009, A&A, 495, 881
Visser, R., Doty, S. D., & van Dishoeck, E. F. 2011, A&A, 534, A132
Visser, R., Kristensen, L. E., Bruderer, S., et al. 2012, A&A, 537, A55
Visser, R., Jørgensen, J. K., Kristensen, L. E., van Dishoeck, E. F., & Bergin, E. A. 2013, ApJ, 769, 19
Viti, S., Jimenez-Serra, I., Yates, J. A., et al. 2011, ApJ, 740, L3
Vuong, M. H., Montmerle, T., Grosso, N., et al. 2003, A&A, 408, 581
Wakelam, V., Vastel, C., Aikawa, Y., et al. 2014, MNRAS, 445, 2854
Walker, K. M., Song, L., Yang, B. H., et al. 2015, ApJ, 811, 27
Walsh, C., Nomura, H., Millar, T. J., & Aikawa, Y. 2012, ApJ, 747, 114
Walsh, C., Millar, T. J., Nomura, H., et al. 2014, A&A, 563, A33
Walsh, C., Nomura, H., & van Dishoeck, E. 2015, A&A, 582, A88
Wampfler, S. F., Herczeg, G. J., Bruderer, S., et al. 2010, A&A, 521, L36
Wampfler, S. F., Bruderer, S., Kristensen, L. E., et al. 2011, A&A, 531, L16
Wampfler, S. F., Bruderer, S., Karska, A., et al. 2013, A&A, 552, A56
Wang, K. S., van der Tak, F. F. S., & Hogerheijde, M. R. 2012, A&A, 543, A22
Watson, W. D. 1976, Rev. Mod. Phys., 48, 513
Watson, D. M., Bohac, C. J., Hull, C., et al. 2007, Nature, 448, 1026
Watson, D. M., Calvet, N. P., Fischer, W. J., et al. 2016, ApJ, 828, 52
Weingartner, J. C., & Draine, B. T. 1999, ApJ, 517, 292
Werner, M. W., Roellig, T. L., Low, F. J., et al. 2004, ApJS, 154, 1
Whittet, D. C. B. 2010, ApJ, 710, 1009
Whittet, D. C. B., Poteet, C. A., Chiar, J. E., et al. 2013, ApJ, 774, 102
Willacy, K., & Woods, P. M. 2009, ApJ, 703, 479
Woitke, P., Kamp, I., & Thi, W.-F. 2009, A&A, 501, 383
Wright, G. S., Wright, D., Goodson, G. B., et al. 2015, PASP, 127, 595
Wyrowski, F., van der Tak, F., Herpin, F., et al. 2010, A&A, 521, L34
Wyrowski, F., Güsten, R., Menten, K. M., et al. 2016, A&A, 585, A149
Yang, B., Stancil, P. C., Balakrishnan, N., & Forrey, R. C. 2010, ApJ, 718, 1062
Yang, C., Gao, Y., Omont, A., et al. 2013, ApJ, 771, L24
Yang, C., Omont, A., Beelen, A., et al. 2016, A&A, 595, A80
Yang, Y.-L., Green, J. D., Evans, II, N. J., et al. 2018, ApJ, 860, 174
Yen, H.-W., Takakuwa, S., Ohashi, N., et al. 2014, ApJ, 793, 1
Yen, H.-W., Koch, P. M., Takakuwa, S., et al. 2017, ApJ, 834, 178
Yıldız, U. A., Kristensen, L. E., van Dishoeck, E. F., et al. 2012, A&A, 542, A86
Yıldız, U. A., Acharyya, K., Goldsmith, P. F., et al. 2013a, A&A, 558, A58
Yıldız, U. A., Kristensen, L. E., van Dishoeck, E. F., et al. 2013b, A&A, 556, A89
Yıldız, U. A., Kristensen, L. E., van Dishoeck, E. F., et al. 2015, A&A, 576, A109
Yvart, W., Cabrit, S., Pineau des Forêts, G., & Ferreira, J. 2016, A&A, 585, A74
Zhang, K., Pontoppidan, K. M., Salyk, C., & Blake, G. A. 2013, ApJ, 766, 82

[1] Leiden Observatory, Leiden University, PO Box 9513, 2300 RA Leiden, The Netherlands
e-mail: ewine@strw.leidenuniv.nl
[2] Max-Planck Institut für Extraterrestrische Physik (MPE), Giessenbachstr. 1, 85748 Garching, Germany
[3] Niels Bohr Institute & Centre for Star and Planet Formation, Copenhagen University, Øster Voldgade 5–7, 1350 Copenhagen K, Denmark
[4] Max Planck Institute for Astronomy, Königstuhl 17, 69117 Heidelberg, Germany
[5] Institute for Particle Physics and Astrophysics, ETH Zurich, 8093 Zurich, Switzerland
[6] Department of Astronomy, The University of Michigan, 1085 S. University Ave., Ann Arbor, MI 48109-1107, USA
[7] Lab. d'astrophysique de Bordeaux, Univ. Bordeaux, CNRS, B18N, allée Geoffroy Saint-Hilaire, 33615 Pessac, France
[8] National Research Council Canada, Herzberg Astronomy and Astrophysics, 5071 West Saanich Rd, Victoria, BC, V9E 2E7, Canada
[9] Department of Physics & Astronomy, University of Victoria, Victoria, BC, V8P 1A1, Canada
[10] Department of Space, Earth and Environment, Chalmers University of Technology, Onsala Space Observatory, 439 92 Onsala, Sweden
[11] INAF – Osservatorio Astronomico di Roma, Via di Frascati 33, 00074, Monte Porzio Catone, Italy
[12] Observatorio Astronómico Nacional (OAN), Calle Alfonso XII, 3, 28014 Madrid, Spain
[13] SRON Netherlands Institute for Space Research, PO Box 800, 9700 AV Groningen, The Netherlands
[14] Kapteyn Astronomical Institute, University of Groningen, PO Box 800, 9700 AV Groningen, The Netherlands
[15] Max-Planck-Institut für Radioastronomie, Auf dem Hügel 69, 53121 Bonn, Germany
[16] INAF – Istituto di Astrofisica e Planetologia Spaziali, via Fosso del Cavaliere 100, 00133 Roma, Italy
[17] Division of Geological and Planetary Sciences, California Institute of Technology, Pasadena, CA 91125, USA
[18] LERMA & UMR8112 du CNRS, Observatoire de Paris, PSL University, Sorbonne Universités, 75014 Paris, France
[19] Instituto de Fisica Fundamental (IFF-CSIC), Calle Serrano 123, 28006 Madrid, Spain
[20] Korean Astronomy and Space Science Institute, Daejeon 34055, Korea
[21] Anton Pannekoek Institute for Astronomy, University of Amsterdam, Science Park 904, 1098XH Amsterdam, The Netherlands
[22] INAF, Osservatorio Astrofisico di Arcetri, Largo Enrico Fermi 5, 50125 Firenze, Italy
[23] Department of Physics & Astronomy, University of Waterloo, 200 University Avenue, Waterloo, ON, N2L 3G1, Canada
[24] National Astronomical Observatory of Japan, 2-21-1 Osawa, Mitaka, Tokyo 181-8588, Japan
[25] Kavli Institute for Astronomy and Astrophysics, Peking University, Yiheyuan Lu 5, Haidian Qu, 100871 Beijing, PR China
[26] Institute of Astronomy, Faculty of Physics, Astronomy and Informatics, Nicolaus Copernicus University, Grudziadzka 5, 87-100 Torun, Poland
[27] Department of Physics and Astronomy, San Jose State University, One Washington Square, San Jose, CA 95192-0106, USA
[28] Center for Astrophysics, Harvard & Smithsonian, 60 Garden Street, Cambridge, MA, 02138, USA
[29] Leiden Institute of Chemistry, Gorleaus Laboratories, Leiden University, PO Box 9502, 2300 RA Leiden, The Netherlands
[30] Department of Astronomy, Stockholm University, 106 91 Stockholm, Sweden
[31] INAF – Osservatorio Astronomico di Cagliari, via della Scienza 5, 09047 Selargius, Italy
[32] Jet Propulsion Laboratory, California Institute of Technology, 4800 Oak Grove Drive, Pasadena, CA 91109, USA
[33] Department of Physics & Astronomy, Johns Hopkins University, Baltimore, MD 21218, USA
[34] SRON Netherlands Institute for Space Research, Sorbonnelaan 2, 3584 CA Utrecht, The Netherlands
[35] School of Physics and Astronomy, University of Leeds, Leeds LS2 9JT, UK
[36] Center for Space and Habitability (CSH), University of Bern, Gesellschaftsstrasse 6, 3012 Bern, Switzerland

Appendix A: Overview of Herschel programs

Table A.1. WISH key program and related OT programs.

Program	Subprogram	(co-)PIs	h	# Sources	Main char.
WISH		E.F. van Dishoeck	499		Mostly HIFI lines PACS lines + selected maps
	Pre-stellar cores	P. Caselli		2	
	LM protostars	L. Kristensen/J. Mottram		29	
	Outflows	R. Lisau/B. Nisini/M. Tafalla		26	
	IM protostars	M. Fich/D. Johnstone		6	
	HM protostars	F. van der Tak/F. Herpin/F. Wyrowski		24	
	Disks	M. Hogerheijde/E. Bergin		12	
	Radiation diag.	A. Benz		12	
WILL		E.F. van Dishoeck/J. Mottram	134	49	LM selected HIFI+PACS lines
DIGIT		N.J. Evans	250	30	LM full PACS scans
COPS-HIFI		L. Kristensen	14	24	LM HIFI CO 16-15 / OH
LM-deep		R. Visser	20	5	Deep HIFI excited $H_2^{18}O$
Outflows		B. Nisini	54	5	LM PACS [O I], CO, H_2O maps
Water maps		R. Liseau	19	6	HIFI H_2O maps + PACS [O I]
IM Cygnus		S. Bontemps			HIFI selected lines
HM ATLASGAL		F. Wyrowski			HIFI selected lines
Disks		M. Hogerheijde	135	4	Very deep HIFI
WatCH		S. Wampfler	19	8	HIFI HCO^+, OH, H_3O^+

Table A.1 summarizes the various subprograms of the WISH key program as well as related *Herschel* open time programs whose data have been used in the analysis.

Appendix B: Observational details and data reduction

B.1. HIFI

HIFI consisted of a set of seven single-pixel dual-sideband heterodyne receivers (de Graauw et al. 2010). All observations were taken in both horizontal and vertical polarizations with simultaneously the Wide Band Spectrometer (WBS) and High Resolution Spectrometer (HRS) backends providing both wideband (WBS, 4 GHz bandwidth at 1.1 MHz resolution) and high-resolution (HRS, typically 230 MHz bandwidth at 250 kHz resolution) frequency coverage. The sideband ratio is approximately unity (Roelfsema et al. 2012).

Observations were taken as single pointings in dual-beam-switch (DBS) mode with a chop throw of 3′ using fast chopping. The only exception are some of the H_2O $1_{10}-1_{01}$ observations of LM sources, which were taken in position-switch mode to an emission-free position (see Kristensen et al. 2012, for details). The *Herschel*-HIFI beam ranges from 12.7″ to 38.7″ over the frequency range of the various water lines, set by the diffraction limit of the primary mirror.

The data were reduced within the *Herschel* Interactive Processing Environment (HIPE; Ott 2010; Shipman et al. 2017). After initial spectra production, first the instrumental standing waves were removed where required. This is especially important at the highest frequencies, see Kristensen et al. (2017b) for details. This was followed by baseline subtraction with a low-order (≤2 in general) polynomial in each sub-band. The fit to the baseline was then used to calculate the continuum level, taking into account the dual-sideband nature of the HIFI detectors. The initial continuum level is the combination of emission in both the upper and lower sidebands, which are assumed to be equal, so the final continuum level is half this value. Subsequently the WBS sub-bands were stitched together into a continuous spectrum and all data were converted to the $T_{\rm MB}$ scale using efficiencies from Roelfsema et al. (2012). Finally, all data were resampled to typically ∼0.3 km s^{-1} on the same velocity grid and either imported into CLASS or as FITS files into custom-made python routines for further analysis.

Comparison of the two polarizations for each source revealed insignificant differences in line shape or gain in most cases (although occasional differences up to 30% were seen, especially at highest frequencies), so these were co-added to reduce the noise. Comparison of peak and integrated intensities between the original WISH observations and those obtained as part of open time programs for the same source indicate that the calibration uncertainty is <10%. The velocity calibration is better than 100 kHz, while the pointing uncertainty is better than 2″ (Roelfsema et al. 2012). The beam positions of the H and V polarizations were, however, offset by up to 6″ at the lowest frequencies, so although the overall pointing accuracy was good, it did not mean that HIFI was always perfectly pointed on-source. For specific peculiarities of individual sources see discussion in Kristensen et al. (2012); Mottram et al. (2014); van der Tak et al. (2013, 2019). The HIFI OTF data reduction is described in Jacq et al. (2016).

B.2. PACS

The PACS integral field unit (IFU) spectroscopy mode was used consisting of two photoconductor arrays with 16 × 25 pixels, allowing simultaneous observations in the red 1st order grating (102–210 μm) and one of the 2nd or 3rd order blue gratings (51–73 or 71–105 μm) (Poglitsch et al. 2010). The IFU had 5 × 5 spatial pixels (called "spaxels") of 9.4″ × 9.4″ each, which covered a 47″ × 47″ field of view. It is important to note that the *Herschel* beam changes with wavelength whereas the spaxel size

stays constant, so that corrections for the wavelength-dependent loss of radiation need to be applied in case of a well-centered point source.

The spectral resolving power R increases with wavelength from about 1000 to 2000 (corresponding to velocity resolutions of 140 to 320 km s^{-1}) in 1st order and from about 1500 to 3000 (100 to 210 km s^{-1}) in 2nd order. At the shortest wavelengths, the velocity resolution is as good as 75 km s^{-1}, so the [O I] 63 μm line sometimes shows velocity-resolved line profiles (van Kempen et al. 2010; Nisini et al. 2015; Karska et al. 2018).

Most WISH observations obtained single footprint spectral maps in IFU line-scan mode in which deep observations are obtained for a narrow wavelength region around selected transitions (bandwidth $\Delta\lambda = 0.5 - 2$ μm). All observations used a chopping/nodding observing mode with off-positions within 6′ of the target coordinates to subtract the background emission.

Data reduction was performed with HIPE including spectral flat-fielding (see Herczeg et al. 2012; Green et al. 2013, 2016; Karska et al. 2018, for full details). The flux density was normalized to the telescopic background and calibrated using observations of Neptune. The overall calibration uncertainty in flux densities is estimated to be ~20% from cross comparisons of sources observed in multiple programs or modes (e.g., Karska et al. 2018). 1D spectra were obtained by summing over a number of spaxels chosen after inspection of the 2D spectral maps (Karska et al. 2013). For sources with extended line emission, the co-addition of spaxels with detected emission increases the S/N, smooths the continuum, and enables correction for significant differences in diffraction-limited beam sizes over the wide spectral range covered by PACS. For sources with point-like emission, only the central spaxel was used, multiplied by wavelength-dependent instrumental correction factors to account for the different point source functions (PSF) (see PACS Observers Manual).

The PACS full range spectroscopy mode, in which the entire far-infrared spectrum from 50 to 210 μm is obtained, was used for a few WISH sources (Herczeg et al. 2012; Goicoechea et al. 2012) and for all DIGIT sources (which partially overlap with the WISH sample, 8 sources in common) (Green et al. 2013). However, the spectral sampling within a resolution element is about 3–4 times coarser in the full spectral scan than in line spectroscopy mode, and integrations are generally less deep. Figure 7 shows part of the NGC 1333 IRAS 4A spectral scan compared with that of the neighboring 4B source (Herczeg et al. 2012), with the latter clearly richer in lines. Figure 3 illustrates the importance of spectral sampling for a few PACS lines observed in both line and range spectroscopy modes.

Appendix C: Additional water spectra

Figure C.1 presents the p-H_2O $1_{11}-0_{00}$ spectra of all high-mass sources, illustrating the multitude of foreground clouds along the lines of sight.

Figure C.2 presents the averaged and normalized water spectra and high-J CO spectra for each class of sources, from low- to high mass. The water spectra arise from medium-J levels that do not connect with the ground state so that no absorption features are present. The similarity in profiles within each class of sources and between classes of sources is clearly seen, with only the low-mass Class I profiles narrower than the others.

Figure C.3 presents deep integrations of the excited $3_{12}-3_{03}$ $H_2^{18}O$ transition ($E_{up} = 250$ K) toward low-, intermediate-, and high-mass sources. The line is barely detected toward the low- and intermediate-mass sources, as opposed to the high-mass

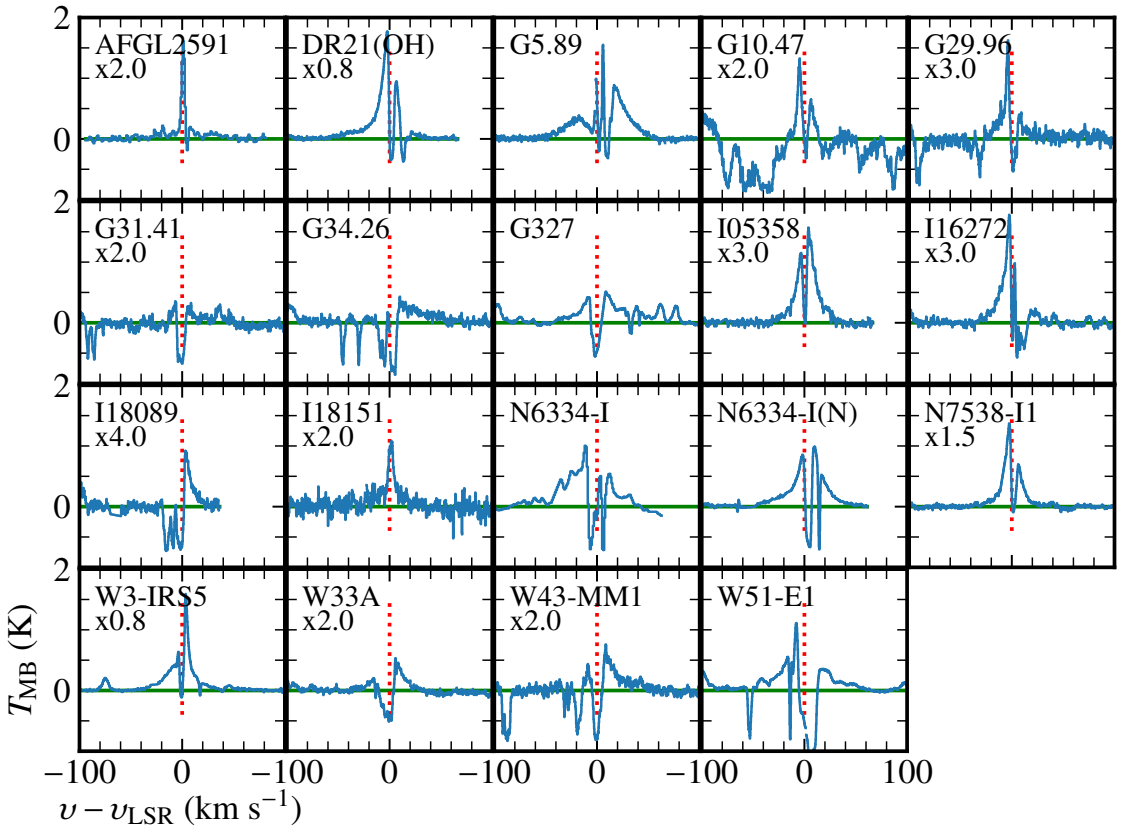

Fig. C.1. H_2O $1_{11}-0_{00}$ spectra toward all high-mass sources in the WISH program.

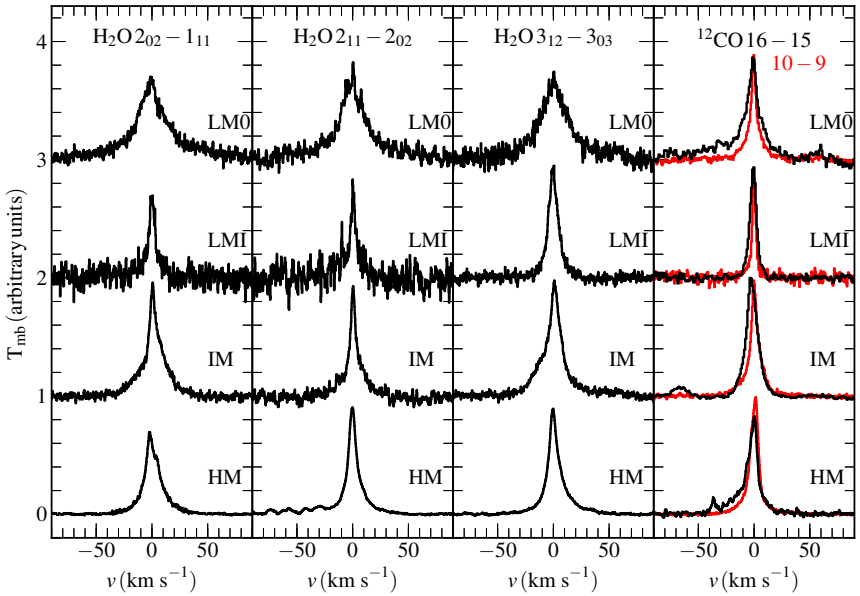

Fig. C.2. Averaged and normalized mid-J water and CO spectra for low-mass Class 0 (LM0), low-mass Class I (LMI), intermediate mass (IM) and high mass (HM) sources. From left to right the H_2O $2_{02}-1_{11}$ line at 988 GHz, $2_{11}-2_{02}$ line at 752 GHz, the $3_{12}-3_{03}$ line at 1097 GHz, and the CO $J = 16–15$ together with the 10–9 profiles are presented. All spectra have been shifted to zero velocity. The low intensity features on the blue wing of the 752 GHz HM spectrum are due to methanol emission. Data from San José-García et al. (2013, 2016); Kristensen et al. (2017b)

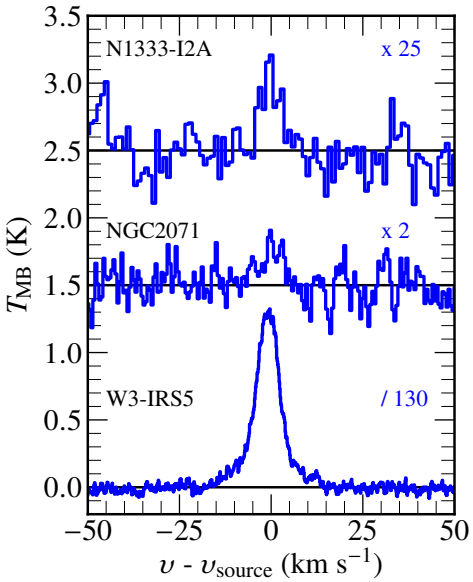

Fig. C.3. Deep $H_2^{18}O$ $3_{12}-3_{03}$ spectra obtained toward a low-mass, intermediate-mass and high-mass protostar (from top to bottom) (based on Visser et al. 2013).

source where it is prominent. However, in spite of the difference in S/N, there is no indication that the line emission traces different components toward the different sources: it probes warm water in the inner envelope on small scales.

Appendix D: Water chemistry: three routes

D.1. Water and related species

The chemical reactions that form water in interstellar space have been well described in various papers, details of which will not be repeated here (see recent overviews in Hollenbach et al. 2009; van Dishoeck et al. 2013; Lamberts et al. 2013). References to papers are mostly those that have appeared since the 2013 reviews. Three main routes can be distinguished, which are summarized in Fig. 4: (i) gas-phase ion-molecule chemistry, driven by cosmic ray ionization of H and H_2; (ii) high temperature gas-phase neutral-neutral chemistry initiated by the O + H_2 reaction; and (iii) ice chemistry.

Route (i) dominates the formation of water in cold low-density diffuse and translucent clouds with visual extinctions of a few magnitudes. *Herschel*-HIFI has probed this chemistry in detail through far-infrared absorption line observations of H_2O as well as intermediates OH^+ and H_2O^+ as part of the PRISMAS key program (Flagey et al. 2013; Gerin et al. 2016). Typical observed H_2O abundances are low, only $(0.5–1.5)\times10^{-8}$ with respect to total hydrogen, which are well reproduced by models such as those by Hollenbach et al. (2009) within factors of 2. In the WISH sample, the intermediate species OH^+, H_2O^+ and H_3O^+ have been detected together with water in foreground clouds toward many protostars (e.g., Benz et al. 2010, 2016; Wyrowski et al. 2010). Analysis of these WISH + PRISMAS data have resulted in a mean value of the cosmic ray ionization rate of $\zeta_H = 1.8\times10^{-16}$ s^{-1} in diffuse clouds (Indriolo et al. 2015b).

Route (ii) is much more relevant for star-forming regions, where temperatures close to protostars and in winds can be up to a few hundred K and in shocks as high as a few thousand K. The reaction O + H_2 → OH + H is endothermic, whereas the subsequent reaction OH + H_2 → H_2O + H is exothermic but has a significant energy barrier of ~2100 K (Baulch et al. 1992). The rates for these reactions have been critically discussed by van Dishoeck et al. (2013) and start to dominate water formation at temperatures above ~250 K. Water destruction can occur by the reverse reaction with atomic H, but this reaction has a very high barrier of ~10^4 K and is unlikely anyhow in dense molecular gas because of the low abundance of atomic H. This leaves UV photons as the main route for water destruction, with X-rays only effective in regions of high extinction. Photodissociation of H_2O starts to be effective shortward of 1800 Å and continues down to the ionization threshold at 983 Å (12.61 eV), including

Ly α at 1216 Å. Its lifetime in the general interstellar radiation field, as given by Draine (1978), is only 40 yr (Heays et al. 2017). Close to (proto)stars, the UV radiation field is enhanced by many orders of magnitude, making the water vapor lifetime even shorter.

Route (iii) dominates the formation of water in cold dense clouds, and is in fact the route that produces the bulk of water in space (Bergin et al. 2000; van Dishoeck et al. 2013, for review) since freeze-out of gaseous water is insufficient (Lee et al. 1996). The timescale for an atom or molecule to collide with a grain and stick to it is $t_{\rm freeze} = 3 \times 10^9/n({\rm H_2})$ yr for normal 0.1 μm size grains and sticking probabilities close to unity. Since the freeze-out time scales as $1/n$ whereas the free-fall time of a cloud (which is a lower limit to its lifetime) scales as $1/\sqrt{n}$, the former becomes shorter than the latter for densities $>10^4$ cm^{-3} so most species will end up on the grains (e.g., Bergin & Tafalla 2007). The grain temperature plays a key role in the ability to retain species on grains and for surface reactions to occur. Light species such as H and H_2 are weakly bound so they have a high mobility and short residence time on the grains. In fact, for grain temperatures above ~20 K, this residence time is so short that hydrogenation ceases to be effective, except through the direct Eley-Rideal mechanism. Heavier species such as O and OH are more strongly bound and less mobile. These rates are usually parametrized through binding energies $E_{\rm b}$ and diffusion energies $E_{\rm d}$, with the latter often taken to be a fraction of 0.3–0.7 of $E_{\rm b}$. At the lowest temperatures, tunneling reactions of H and H_2 can be important as well (Meisner et al. 2017; Lamberts & Kästner 2017; Cuppen et al. 2017).

Tielens & Hagen (1982) postulated that the formation of water from O atoms on grain surfaces proceeds through three routes involving hydrogenation of s−O, s−O_2 and s−O_3, respectively, where s−X indicates a species on the surface. All three routes have subsequently been studied and quantified in various laboratories (see Linnartz et al. 2015, for summary) (Fig. 4).

Water ice can be returned to the gas by various desorption processes. The most effective one is thermal desorption, which occurs on timescales of years when the dust temperature rises above ~100 K (precise value depends on pressure). This leads to gas-phase abundances of H_2O as high as the original ice abundances, if there is no subsequent destruction of gaseous H_2O. This process dominates the production of gaseous water in the warm inner parts of high- and low-mass protostellar envelopes ("hot cores" or "hot corinos") and inside the snow line in disks. Water ice can also be sputtered by energetic particles in shocks, but not all water ice may be returned to the gas and some of it may be dissociated (see Sect. 5 for details).

At dust temperatures below the sublimation limit, photodesorption is an effective mechanism to get water back into the gas phase, even though only a small fraction of the UV absorptions results in desorption of intact H_2O molecules (Andersson & van Dishoeck 2008). The efficiency is about 10^{-3} per incident photon within factors of a few, as determined through laboratory experiments and theory (e.g., Arasa et al. 2015; Cruz-Diaz et al. 2018). Only the top few monolayers of the ice contribute. Thus, icy clouds exposed to radiation from a nearby star or the general interstellar radiation field will have a layer of enhanced water vapor at the edge, the so-called "photodesorption layer" (Hollenbach et al. 2009).

Deep inside clouds, cosmic rays produce a low level of UV flux, ~10^4 photons cm^{-2} s^{-1}, through interaction with H_2 (Prasad & Tarafdar 1983; Shen et al. 2004; Ivlev et al. 2015). This process turns out to be crucial for explaining the water observations of cold dense clouds. Other nonthermal ice desorption processes include cosmic ray induced spot heating (which may work for CO, but is generally not efficient for strongly bound molecules such as H_2O) and desorption due to the energy liberated by the formation reaction (called "reactive" or "chemical" desorption). The latter process is less well understood and constrained than photodesorption and may not be as effective on water ices as on other surfaces (Dulieu et al. 2013; Minissale et al. 2016).

Stimulated by the discovery of abundant O_2 ice in comet 67P but lack of H_2O_2 and O_3 ice (Bieler et al. 2015), a new critical look has been taken at the ice formation network (Taquet et al. 2016; Eistrup & Walsh 2019). Important parameters whose values are still uncertain and that are found to have an impact are (i) the diffusion to binding energy ratios $E_{\rm d}/E_{\rm b}$; (ii) the binding energy of atomic oxygen on ice, $E_{\rm b}$(O), now found to be ~1600 K, a factor of 2 higher than adopted in earlier work (He et al. 2015); (iii) the activation barriers $E_{\rm a}$ of the reactions O + O_2 and H + O_2. Lamberts et al. (2014) conclude that the O + H_2 reaction is not important for water ice formation at low temperatures.

Taken together, it is gratifying to conclude that the advent of *Herschel* has stimulated a number of laboratory and theoretical chemical physics studies of fundamental gas-phase and solid-state processes involved in the water network.

D.2. CO_2 chemistry

Another molecule which could potentially be a significant oxygen carrier is CO_2. Its chemistry is loosely connected with that of H_2O, primarily through the OH radical.

Gas-phase formation of CO_2 takes place mostly through the reaction CO + OH → CO_2 + H, which has a slight activation barrier of 176 K (Smith et al. 2004). The CO_2 production rate is controlled by the availability and fate of OH, since OH can also be consumed by the H_2O formation route, OH + H_2 → H_2O + H. This route has a higher activation energy, 1740 K, than that leading to CO_2, so CO_2 production is favored at lower temperatures. However, since H_2 is orders of magnitude more abundant than CO, the formation of H_2O dominates at higher temperatures, typically above 150 K (Bosman et al. 2018b). Thus, gaseous CO_2 formation is only effective in a quite narrow temperature range, 50–150 K, and then only when OH is present as well. In dense regions, this requires UV photons or X-rays to liberate O and OH from H_2O or CO.

The grain-surface formation of CO_2 is thought to proceed primarily through the s-CO + s-OH → s-HOCO route, with most of the s-HOCO subsequently converted into s-CO_2 as found in laboratory experiments (e.g., Ioppolo et al. 2011) and theoretical calculations (Arasa et al. 2013). Again the reaction rate depends on the s-OH abundance, usually created by cosmic-ray induced photodissociation of s-H_2O. Alternative proposed CO_2 formation routes include the energetic processing of ice mixtures (e.g., Ioppolo et al. 2009) and UV irradiation of water-ice covered hydrogenated carbon grains (Mennella et al. 2006).

The s-CO_2 binding energy is about 2300 K (Noble et al. 2012). This implies that the s-CO_2 desorption temperature (its snow line) is in between that of H_2O and CO.

Appendix E: Excitation and radiative transfer of water vapor

The populations of the H_2O and CO energy levels are determined by the balance between the collisional and radiative excitation and de-excitation rates. A major effort was undertaken by the

chemical physics community in preparation for *Herschel* to calculate the collisional rate coefficients of H_2O and CO with H_2 over a wide range of temperatures. In WISH, the latest values from Daniel et al. (2011) for H_2O and Yang et al. (2010) and Neufeld et al. (2010) for CO have been used, as tabulated in LAMDA (Schöier et al. 2005). More recently, rate coefficients for CO + H up to high temperatures have become available which play a role in regions with high H/H_2 fractions (Walker et al. 2015).

The water radiative transfer is particularly complex, because the large Einstein A values, subthermal excitation, (very) high optical depths and large numbers of lines that need to be included. However, many lower J water lines are effectively thin, a regime in which the line brightness still scales with column density (e.g., Snell et al. 2000). This assumption holds as long as the collision rate is so slow that every excitation immediately leads to a radiative de-excitation and the production of one photon which escapes the cloud, possibly after many absorptions and re-emissions, before another excitation occurs. In formulae, this implies $C < A/\tau$, where C is the collision rate and τ the optical depth (Linke et al. 1977; Keto et al. 2014). To properly treat water vapor excitation, many energy levels need to be taken into account; while this slows down the computing speed, the advantage is that some of the higher-lying lines, especially those in the PACS domain, become optically thin so that they better the excitation models. Another complication is that at high frequencies, the continuum can become optically thick as well, thus limiting the depths for looking into the innermost part of the source (Cernicharo et al. 2006; van Kempen et al. 2008; Visser et al. 2013). This far-infrared dust continuum can also effectively couple with the water excitation (González-Alfonso et al. 2014).

WISH team members developed and used a number of radiative transfer codes to analyze the *Herschel* data, ranging from the simple constant density and temperature non-LTE excitation program RADEX using a local escape probability (van der Tak et al. 2007) to more sophisticated 1D nonlocal Monte-Carlo codes RATRAN (Hogerheijde & van der Tak 2000) and MOLLIE (Keto et al. 2004) that can handle radial temperature and density variations as expected in cold cores and protostellar envelopes and that also follow the transport of continuum photons. For nonspherical geometries, a 2D version of RATRAN and the 3D code LIME (Brinch & Hogerheijde 2010) have been used, as well as a fast 3D code using a local source approximation by Bruderer et al. (2010). Also, team members had access to the Onsala Accelerated Lambda Iteration (ALI) code for arbitrary source structures that can treat line overlap (Maercker et al. 2008). These codes have been tested against each other in a 2004 workshop (van der Tak et al. 2005) and subsequent WISH team meetings.

Appendix F: Modeling approaches

F.1. Retrieval models

The simplest analysis method is to use a non-LTE excitation and radiative transfer code such as RADEX to derive best-fitting densities and temperatures from observed line ratios. Also column densities and emitting areas can be derived from the observed line intensities, although there is often some degeneracy between parameters (see van der Tak et al. 2010; Herczeg et al. 2012; Mottram et al. 2014; Santangelo et al. 2014b, for examples). This method is most appropriate for shock components seen in on-source line profiles and at shock positions offset from the source.

To constrain the envelope abundance, a retrieval method is commonly used in which a trial water abundance is chosen. Usually a step function with a low outer and high inner abundance (when $T > 100$ K) is adopted (see also Sect. 7.1.2). The molecular excitation and radiative transfer in the line is then computed at each position in the envelope, using a temperature and density profile constrained by other data. The resulting sky brightness distribution is convolved with the *Herschel* beam profile. These inner and outer abundances are then adjusted until best agreement with observational data is reached. The velocity structure can be a constant (turbulent) broadening as function of position in the envelope, and/or some other function such as infall or expansion (see Johnstone et al. 2010; Herpin et al. 2012, for examples).

For simplicity, spherically symmetric models are typically adopted but *Herschel* data show that often UV-heated cavity walls need to be added in a 2D geometry (see Bruderer et al. 2009; Visser et al. 2012; Lee et al. 2013, for examples)

F.2. Forward models

The forward modeling approach uses a chemical model as illustrated in Fig. 4 coupled with a physical model of the source to compute abundances as function of position and time. These are then fed into excitation and radiative transfer calculations to obtain the line intensity maps, which are finally convolved with the beam. These chemistry models can be run either in steady-state or in a time-dependent mode at each position in the cloud. Best fit parameters in this case can be any parameter fed into the chemical network such as overall (initial) abundances or rates of reactions. Often, the chemical evolution time ("age") or cosmic ray ionization rate are adjusted to obtain the best fit (see Doty et al. 2006; Caselli et al. 2012, for examples). As noted above, often simplified chemistry networks are used for computational speed and to allow key processes to be identified.

Some of the above models keep the physical structure of the source fixed even when the chemistry evolves in time, while others let the physical structure evolve. Also, a parcel of gas often stays fixed at a given location in the source. An alternative approach is to follow the chemistry of a parcel of gas as it falls in from large radii to smaller distances and eventually enters the (forming) protostellar disk. In the context of WISH, such 2D models have been developed and applied to water by Visser et al. (2009, 2011) and for deuterated water by Furuya et al. (2017).

Appendix G: Oxygen budget

This section summarizes our current understanding of the oxygen budget in various regions of the interstellar medium that are part of the star- and planet formation cycle. The different oxygen reservoirs are summarized in Table 3 and visualized in percentages in Fig. 32 in the main text. The following subsections provide more background information on the numbers in this table and figure. The numbers in the text plus their uncertainties are generally as stated in the original papers, with added text to motivate the uncertainties. The number of significant digits therefore varies and should not be taken to reflect the actual uncertainties. Very small numbers have been rounded off to (<)1 ppm.

G.1. Overall and refractory oxygen budget

The overall [O]/[H] abundance of oxygen in all forms in the ISM is taken to be 5.75×10^{-4} or 575 ppm, as measured for early

B-type stars (Przybilla et al. 2008). This number, denoted in short as [O], is somewhat higher than the solar oxygen abundance of 4.9×10^{-4} or 490 ppm (Asplund et al. 2009; Grevesse et al. 2010). A recent compilation by Lodders (2019) of solar and meteoritic abundances gives a recommended value for the present solar system of 537 ppm (their Table 8), with values ranging from 512–660 ppm. The solar and solar system abundances presumably reflect the ISM composition as it was 4.6 Gyr ago, whereas the higher Przybilla et al. (2008) value is representative of hotter and therefore younger stars. Indeed, the difference in abundances is consistent with galactic chemical evolution models (Chiappini et al. 2003). In the following analysis, [O] = 575 ppm is used, but other studies (e.g., Pontoppidan et al. 2014) use the lower [O] abundance in their analysis of the oxygen budget in protoplanetary disks, decreasing the need for unidentified forms of oxygen by nearly 100 ppm.

Oxygen can be partitioned into gas, ice and dust. The gas and ice are considered as "volatiles", the dust as "refractories", with the difference related to the sublimation temperature of the material. The boundary between the two categories is traditionally taken to be around 600 K, so that refractories include at least all the silicates, metals (as chemically defined), and metal oxides. The fraction of oxygen locked up in refractory dust, [O_{refr}], then comes from counting the amount of [Mg], [Si] and [Fe] in the ISM, together denoted as [M]. Here the analysis of Whittet (2010) is followed. Depending on the type of mineral (e.g., olivines or pyroxenes or metal oxides), the oxydation ratios differ slightly. The maximum is [O_{refr}]/[M] = 1.5, whereas the minimum is [O_{refr}]/[M] = 1.2. This number could be lower only if a large fraction of Fe would be in carbonaceous grains (Weingartner & Draine 1999). Using the Mg, Si and Fe abundances of Przybilla et al. (2008), this gives [O_{refr}] = 90–140 ppm. The value of [O_r] = 140 ppm is assumed here. This number does not include any oxygen locked up in refractory organics or any other types of refractory material.

G.2. Diffuse clouds

Diffuse interstellar clouds with extinctions A_V <1 mag have the advantage that all hydrogen atoms (in H and H_2) as well as the dominant form of oxygen, neutral atomic oxygen O, can be measured directly with high accuracy through ultraviolet spectroscopy toward background early-type stars. In this paper, the atomic oxygen abundance of O/[H] = 3.2×10^{-4} or 320 ppm is used, as measured by Meyer et al. (1998) with HST-GHRS for 13 lines of sight in the local ISM. The uncertainty of ~10% is due to the spread in measurements as well as a small uncertainty in the oscillator strength of the optically thin O I 1356 Å line. A subsequent survey of the 1356 Å line in the Galactic disk with HST-STIS by Cartledge et al. (2004) finds atomic O abundances ranging from 390 ppm for the lowest density clouds to 284 ppm in higher density regions, consistent with the slight decrease with density seen by Jenkins (2009) in diffuse clouds.

Oxygen-containing molecules such as H_2O and O_2 have abundances in diffuse clouds that are at least 3–4 orders of magnitude lower than that of atomic oxygen (e.g., Spaans et al. 1998; Flagey et al. 2013). Gaseous CO (Sheffer et al. 2008) and ices (Poteet et al. 2015) are also negligible in diffuse molecular clouds. Thus 320 ppm is taken as the amount of volatile oxygen, [O_{vol}] that can cycle between gas and ice in dense clouds.

For our adopted [O] abundance of 575 ppm, the sum of the identified refractory and volatile oxygen is 140 + 320 = 460 ppm, leaving 115 ppm for Unidentified Depleted Oxygen, UDO. The estimated uncertainty in the amount of UDO is significant, of order 50% based on the above discussion, but some UDO still seems required.

These average numbers for diffuse clouds are consistent with the detailed analysis of a single well-studied line of sight, the diffuse molecular cloud toward ζ Oph with $A_V \approx 1$ mag (Poteet et al. 2015). They derive [O_{refr}] in silicates to be 126 ± 45 ppm, with an additional ≤19 ppm in iron oxides such as Fe_3O_4. Taking the measured atomic O toward ζ Oph at 307 ± 30 ppm (Jenkins 2009), together with their upper limits on H_2O ice (≤9−23 ppm depending on grain size) and organic refractory material (<7 ppm in the form of polyoxymethylene), they find that as much as 98–156 ppm of oxygen could be in UDO.

G.3. Dense clouds

Many oxygen-bearing species in gas, ice and dust can be measured directly toward bright infrared sources in or behind dense clouds. Because of their rising spectrum with wavelength, protostars embedded in their natal envelope are particularly suitable for high S/N spectra. As for diffuse clouds, the advantage of absorption line studies is that all species are measured for the same pencil beam line of sight. Summaries of abundances and oxygen budget toward protostars based on data from ISO, *Spitzer* and ground-based instruments are presented in Gibb et al. (2004); Öberg et al. (2011a) and Boogert et al. (2015).

G.3.1. Low mass protostars

For low-mass protostars, the bulk of the envelope is cold so most of the oxygen budget is in ice and dust. The numbers listed in Table 3 are taken from the Boogert et al. (2015) compilation. The median ice abundances in their Table 2 are listed both with respect to water ice and with respect to hydrogen. The latter values require a determination of the total hydrogen column N_H along the line of sight. This column is obtained either from the measured optical depth of the silicate feature $\tau_{9.7\mu m}$ or from the near-IR extinction A_K, or both, with relations between these observables and the total hydrogen column density benchmarked for clouds in which both can be measured (Vuong et al. 2003; Boogert et al. 2013). The amount of oxygen in silicates is taken to be the same as for diffuse clouds, 140 ppm (Whittet 2010).

The bulk of the oxygen in ices is in H_2O, CO_2 and CO ices. Of these three species, CO is the most volatile one and can show significant variation from cloud to cloud. It is the only major ice species that is not formed on the grains but frozen out from the gas, with an ice abundance that depends on temperature and density. However, when the CO ice abundance is low, its gas-phase abundance is high, so this does not affect the total volatile oxygen budget. Taken together, the amount of oxygen measured in ices sums up to only 76 ppm, or 13% of [O].

The gas-phase CO column toward several low-mass protostars has been measured through high spectral resolution infrared observations of CO and its isotopologs by Smith et al. (2015). Their inferred CO ice/(gas+ice) abundances are generally much less than 20% (see their Fig. 11). With CO ice at 10 ppm, this implies a gas-phase CO abundance of at least 40 ppm. Another independent measurement of gaseous CO in cold clouds has been obtained by observing the infrared absorption lines of both CO and H_2 (Lacy et al. 2017). Their inferred CO/H_2 is 1.7×10^{-4} with a variation of ~30% between lines of sight, which would correspond to CO locking up 83 ppm with some spread. Based

on these two studies, we take gaseous CO to account for 100 ppm with a 50% uncertainty.

No direct observational limits exist for gaseous atomic oxygen or other oxygen-bearing molecules, but they should be negligible according to dark cloud models (McElroy et al. 2013). Also, both millimeter interferometry and *Herschel*-WISH+ studies of $H_2^{18}O$ emission lines show that the warm water abundance in the inner regions of low-mass protostars is generally low, much less than 40 ppm (Visser et al. 2013; Persson et al. 2016, their Fig. 11), and that O_2 is negligible (Yıldız et al. 2013b) (see Sect. 7.4).

Taken together, the silicate dust, ices and gas account for only 140 + 76 + 100 + 40 = 356 ppm of oxygen at most. This leaves at least 219 ppm or 38% of the oxygen budget unaccounted for. If all in UDO, this would imply a doubling of its abundance compared with diffuse clouds.

G.3.2. High-mass protostars

The abundances measured toward high-mass protostars listed in Table 3 are also taken from Boogert et al. (2015). Overall, the pattern is similar as for low-mass protostars, except that the ice abundances are even lower. In particular, the CO_2 ice abundance, which counts double for oxygen, is a factor of 2–3 lower in high-mass regions. Taken together, the total amount of oxygen in ices is only 47 ppm.

The envelopes around high-mass protostars are more massive and warmer due to their higher luminosities, so gas-phase column densities are larger than for low-mass sources. The CO abundance in dense warm gas has been measured directly by Lacy et al. (1994) for once source through infrared absorption lines of both CO and H_2 to be $CO/H_2 = 2.5 \times 10^{-4}$, corresponding to 130 ppm. We take CO to contain 100 ppm more generally. For high-mass protostars, CO_2 and H_2O gas have been measured directly through infrared absorption studies with ISO for the same lines of sight as for the ices. CO_2 gas has been detected with typical gas/ice ratios of 0.01–0.08 so it contributes negligibly (Boonman et al. 2003b; van Dishoeck 1998). In contrast, the H_2O gas/ice ratio derived from infrared absorption is more variable, with gas/ice ratios ranging from 0.01-2.2 (van Dishoeck & Helmich 1996; van Dishoeck 1998). With H_2O ice accounting for 31 ppm, this gives H_2O gas at most 62 ppm, about 60% of that of CO. This number is consistent with the measured gaseous H_2O column densities relative to those of hot H_2 in the inner region (Boonman & van Dishoeck 2003), with H_2 derived from CO infrared absorption lines obtained with the CFHT-FTS by Mitchell et al. (1990) assuming $CO/H_2 = 2 \times 10^{-4}$. Interestingly, the corresponding ratio $H_2O/CO \approx 0.6$ is similar to that found by Indriolo et al. (2015a) for some of the same lines of sight using much higher spectral resolution H_2O data obtained with SOFIA-EXES and VLT-CRIRES. Assuming that atomic O and O_2 are negligible, this gives a total of 162 ppm accounted for in the gas.

Taken together, the dust, ice and gas account for 140 + 47 + 162 = 349 ppm, leaving 226 ppm for UDO (40% of oxygen). This is very similar to the case for low-mass protostars, even though very different techniques and instruments are involved for measuring the gas abundances.

G.4. Shocks

Shocks have the advantage that temperatures are so high that all volatile oxygen should be returned to the gas phase. The refractory silicate part is again taken to be 140 ppm, and should be viewed as an upper limit since some silicate dust could be sputtered by the shocks, as evidenced by high gas-phase abundances of SiO (Guilloteau et al. 1992).

The most direct measurements of the gaseous H_2O and CO abundances come from *Herschel*-PACS emission line observations of dense shocks at positions offset from the protostars for which *Spitzer* data on H_2 are available (Neufeld et al. 2014). There is some degeneracy in the fit, however, so not all column densities can be determined independently. For the shock associated with the NGC 2071 outflow, $H_2O/CO = 0.8$ is derived assuming $CO/H_2 = 3.2 \times 10^{-4}$ (that is, assuming most available carbon in CO). This would imply that CO accounts for 160 ppm and H_2O for 128 ppm.

As discussed in Sect. 5 and Table 2, *Herschel* WISH observations of H_2O in shocks associated with low-mass protostars generally give low abundances, down to 1 ppm. The best determined case is that of HH 54 for which H_2 is obtained from spectrally-resolved VLT-VISIR data, finding $H_2O/H_2 < 1.4 \times 10^{-5}$, less than 7 ppm (Santangelo et al. 2014a). Similarly, Kristensen et al. (2017b) find $H_2O/CO \sim 0.02$ for a range of protostars based on *Herschel*-HIFI H_2O and CO 16-15 data. Finally, fitting both CO *Herschel*-PACS and H_2 *Spitzer* data simultaneously in a number of shocks associated with low-mass protostars gives $CO/H_2 \sim 2 \times 10^{-5}$ with values up to 10^{-4}, corresponding to 10–50 ppm (Dionatos et al. 2013, 2018).

OH has been measured in some outflows associated with low- and high-mass sources with *Herschel* but remains a small contributor to the oxygen budget (Wampfler et al. 2011) (see Sect. 5.2). The same holds for O_2 (Melnick et al. 2011) (see Sect. 7.4).

This leaves atomic oxygen as the only other plausible gaseous oxygen reservoir. The few existing SOFIA-GREAT data of spectrally resolved [O I] 63 μm lines imply low abundances, however, with atomic O accounting for at most 15% of the volatile oxygen (Kristensen et al. 2017a). For the NGC 1333 IRAS 4A shock, atomic O is at most 30 ppm.

In summary, for shocks studied with *Herschel* and taking the maximum CO abundance at 160 ppm, as assumed by Neufeld et al. (2014) for NGC 2071, gives a total oxygen budget in silicate dust and gas of 140 + 160 + 128 + 30 = 458 ppm, leaving 117 in unidentified form. Taking instead CO at 100 ppm would give 140 + 100 + 80 + 30 = 350 ppm, leaving 225 ppm for UDO. For shocks associated with low-mass protostars, the CO and H_2O abundances may be up to an order of magnitude lower. Both numbers for UDO for NGC 2071 are remarkably similar to the range found for diffuse clouds and protostars, even though gas and dust in shocks experience much higher temperatures. Apparently, the UDO material is refractory enough that it is not sublimated or sputtered under typical shock conditions with 300–700 K gas probed with *Herschel* data.

There is some evidence that for the hottest gas, >1000 K, more oxygen is returned to the gas and driven into H_2O. Although the best fit to the *Herschel* data of NGC 2071 gives $H_2O/CO < 1$, an acceptable fit can be found with a somewhat higher temperature T_w above which H_2O becomes abundant (1000 K rather than 300 K), which results in $H_2O/CO = 1.2$ (Neufeld et al. 2014). For the same NGC 2071 shock, Melnick et al. (2008) find $H_2O/H_2 = (0.2-6) \times 10^{-4}$ using even higher excitation H_2O lines coming from hotter gas observed with *Spitzer*. The upper range of this study would account for most of the volatile oxygen and leave no room for UDO. Similarly, Goicoechea et al. (2015) identify a hotter, ~2500 K component of the Orion shock in the very high J CO and H_2O *Herschel* lines with $H_2O/CO \sim 1.3$ and $H_2O/H_2 \gtrsim 2 \times 10^{-4}$ and

$CO/H_2 \gtrsim 1.5 \times 10^{-4}$. More such studies using mid-infrared lines probed with JWST are warranted.

G.5. Comets

The Rosetta mission to comet 67P/Churyumov-Gerasimenko has provided a unique opportunity to determine the composition of one icy planetesimal in exquisite detail. Depending on its formation location and history in the solar system, a significant fraction of its composition could be inherited from the dense cloud phase (Drozdovskaya et al. 2019). The bulk abundances of the many molecules measured by the Rosetta instruments in ice and dust are summarized by Rubin et al. (2019) (see also Altwegg et al. 2019). The ice (volatile) abundances are derived primarily from data from the ROSINA instrument (Balsiger et al. 2007) whereas the dust abundances come mostly from the COSIMA instrument (Kissel et al. 2007). There is some ongoing discussion of the overall bulk dust : ice ratio of the comet as a whole, with values ranging from 1:1 (Läuter et al. 2019) to ∼3:1 (by weight) (Rotundi et al. 2015).

The numbers listed in Table 3 are based on those in Table 5 of Rubin et al. (2019) for the 1:1 dust:ice ratio, which is most consistent with estimates for other comets (A'Hearn 2011). For this case, 66% of [O] is in ice, 34% is in dust. Overall, the abundances of [O] and [C] in this comet are close to solar, as measured with respect to [Si]. However, not all of the oxygen in dust is in silicates: in fact, COSIMA finds that nearly 50% of the dust by weight consists of carbonaceous material (Bardyn et al. 2017; Fray et al. 2016). Bardyn et al. (2017) derive [O]/[C] ≈ 0.3 for the organic phase, which they note is close to the average [O]/[C] ratio of ∼0.2 measured in Insoluble Organic Mattter (IOM) in carbonaceous chondrites (Alexander et al. 2007), but lower than [O]/[C] = 0.5 found for carbon-rich phases in Interplanetary Dust Particles (IDPs) (Flynn et al. 2001). Given that [O]/[C]≈1 in the dust phase (Bardyn et al. 2017), this leads to a make up of [O_{refr}] of about 25% in silicate dust and 9% in refractory organics, for a total of 34%.

The comet entries in Table 3 assume that silicate dust is unchanged at 140 ppm. The refractory organics then account for 50 ppm. For the ice phase, the abundances of CO, CO_2 and other O-containing ices (mostly O_2) with respect to H_2O are taken from Table 2 of Rubin et al. (2019), normalized to 66% of total [O].

By definition, there is no room for UDO in the oxygen budget in comets as summarized in Rubin et al. (2019). The question is whether ROSINA and COSIMA measured all possible oxygen reservoirs: some intermediate molecular mass or dust sizes or volatility ranges may have been missed by the instruments. In particular the separation between volatiles and refractories at 600 K may be too strict: there is likely a continuum of semi-volatile or less refractory species which sublimate in the 300–600 K range and which could have escaped detection. Such an oxygen reservoir could be in the form of large organic molecules of intermediate size. It is important to note that large refractory organics by themselves are not the full solution to the UDO problem, since at 50 ppm they account for at most 25–50% of the missing oxygen in diffuse and dense clouds. Another option could be semi-volatile ammonium salts such as $NH_4^+OCN^-$ or $NH_4^+HCOO^-$ which have recently been detected in comet 67P and which appear to be responsible for the bulk of the NH_3 observed in comets (Altwegg et al. 2020; Poch et al. 2020). If the maximum NH_3 abundance with respect to H_2O of 4% measured close to the Sun is used, and if the maximum of two oxygen atoms per nitrogen atom is taken for salts, at most 5% of total volatile [O] can be accounted for in salts, about 19 ppm (Altwegg & Rubin, priv. comm.). The entry "O-other ice" for comets takes this maximum value into account.